The impact of atmospheric motions on source-specific black carbon and the induced direct radiative effects over a river-valley region

Huikun Liu[1], Qiyuan Wang[1,2,4*], Suixin Liu[1,5], Bianhong Zhou[3], Yao Qu[1], Jie Tian[1], Ting Zhang[1], Yongming Han[1,2,4], Junji Cao[6,5*]

[1]Key Laboratory of Aerosol Chemistry and Physics, State Key Laboratory of Loess and Quaternary Geology, Institute of Earth Environment, Chinese Academy of Sciences, Xi'an, 710061, China
[2] CAS Center for Excellence in Quaternary Science and Global Change, Xi'an, 710061, China
[3] Shaanxi Key Laboratory of Disaster Monitoring and Mechanism Simulation, College of Geography & Environment, Baoji University of Arts & Sciences, Baoji 721013, China
[4]Guanzhong Plain Ecological Environment Change and Comprehensive Treatment National Observation and Research Station, Xi'an 710061, China
[5]Shaanxi Key Laboratory of Atmospheric and Haze-fog Pollution Prevention, Xi'an 710061, China
[6]Institute of Atmospheric Physics, Chinese Academy of Sciences, Beijing 100029, China

[*]*Correspondence to*: Qiyuan Wang (wangqy@ieecas.cn) and Junji Cao (jjcao@mail.iap.ac.cn)

Abstract. Black carbon (BC) is one of the most important short lived climate forcers, and atmospheric motions play an important role in determining its mass concentrations of pollutants. Here an intensive observation was launched in a typical river-valley city to investigate relationships between atmospheric motions and BC aerosols. Equivalent BC (eBC) source apportionment was based on an aethalometer model with the site-dependent absorption Ångström exponents (AAEs) and the mass absorption cross-sections (MACs) retrieved using a positive matrix factorization (PMF) model based on observed chemical components (i.e. EC, POC, K^+, Mg, Al, Si, S, Cl, Ca, V, Mn, Fe, Ni, Cu, As, Se, Br, Sr, Pb, Ga, and Zn) and primary absorption coefficients at selected wavelengths from λ = 370 to 880nm. The derived AAEs from 370 to 880nm were 1.07 for diesel vehicular emissions, 2.13 for biomass burning, 1.74 for coal combustion, and 1.78 for mineral dust. The mean values for eBC_{fossil} and $eBC_{biomass}$ were 2.46 μg m^{-3} and 1.17 μg m^{-3} respectively. Wind run distances and the vector displacements of the wind in 24 h were used to construct a self-organizing map, from which four atmospheric motions categories were identified (local-scale dominant, local-scale strong and regional-scale weak, local-scale weak and regional-scale strong and regional-scale dominant). BC pollution was found to be more likely when the influence of local-scale motions outweighed those of regional-scale motions. Cluster analysis for the back trajectories of air mass calculated by Hybrid Single-Particle Lagrangian Integrated Trajectory model at the study site indicated that the directions of air flow can have different impacts for different scales of motion. The direct radiative effects (DRE) of source-specific eBCs were lower when the influence of regional-scale motions outweighed that of the local ones. However, due to chemical aging of the particles during transport, the DRE efficiencies under regional scale motions were ~1.5 times higher than those under more local influences. The finding that the DRE efficiency of BC increased during the regional transport suggested significant consequences in regions downwind of pollution sources and emphasizes the importance of regionally transported BC for potential climatic effects.

删除了: has a strong light absorption ability. It …s one of the most important short livedfe…climate forcers, and which can warm the climateand is known as the second strongest light-absorbing substance in the atmosphere after CO_2.…aA…mospheric motions plays…an important role in determining itsthe ambient…mass concentrations of pollutants. Here The relationship between atmospheric motion and BC aerosols is complex, and detailed investigation of the impact of different scales of motion on BC is still insufficient. Thus, ...

删除了: conducted using the…aethalometer model with the site-dependent absorption Ångström exponents (AAEs) and the mass absorption cross-sections (MACs) which were ...

删除了: data

删除了: the

设置了格式: 上标

删除了: different …avelengths from(i.e.…λ = 370 to, 470, 520, 590, 660, or…880nm) ...

删除了: optical data

删除了: of

删除了: Based on the data of actual …w…nd run distances and the vector displacements of the wind in 24 h,…were used to construct aa ...

删除了: A

删除了: showed that …our featured …tmospheric motions categories were identified (i.e. …ocal-scale dominantce… local-scale strong and regional-scale weak, local-scale weak and regional-scale strong and regional-scale dominantce… were identified at the sampling site… A further analysis of under the four motion categories showed that the …C pollution was found to be more likely to happen …hen the influence of local-scale motions outweighed thoseat…of regional-scale motions. The trajectory …c ...

删除了: HYSPLIT

删除了: s

删除了: air mass…directions of air flow can have different could post divergent …mpacts for under…different scales of atmospheric…motion. The direct radiative effects (DRE) of source-specific eBCs were lower when the influence of regional-scale motions outweighed that of the local ones. However, due to chemical aging of the particles during ...

删除了: is study revealed

删除了: the disproportional change between BC mass concentration and its DRE. T

删除了: was enhanced…during the regional transport suggested significant which could lead to ...

删除了: . It

删除了: that

删除了: highlights

删除了: and its potentially enhanced…potential climatic effects are worthy of attention ...

1 Introduction

Black carbon (BC) is produced by the incomplete combustion of biomass and fossil fuels. The BC aerosol has a strong light absorption capacity and can cause heating of the atmosphere. In fact, BC is widely recognized as one of the most important short-lived climate forcers (IPCC, 2021). Due to this high light-absorbing ability, BC has the potential to perturb the radiative balance between the earth and atmosphere and in so doing cause in the in climate to change and drive ecosystems away from their natural states (Schroter et all., 2005). Those changes ultimately will affect biodiversity and could threaten humans' food security (Ochoa-Hueso et al., 2017; Shindell et al., 2012). Besides heating the atmosphere directly, BC also is important for nucleating clouds, and that is another way in which the particles can cause indirect climatic effects (Jacobson, 2002). As BC is heterogeneously distributed in the atmosphere, its climatic effects are highly variable and dependent on its distribution in the atmosphere, both horizontally and vertically; its radiative properties and how they are affected by of chemical processing; and its lifetime (IPCC, 2021).

The radiative efficiency of BC can vary due to differences in emission sources and atmospheric aging processes (Bond et al., 2013; He et al., 2015; Cappa et al., 2012). Indeed, BC from different sources can vary in light absorbing abilities (Cheng et al., 2011) which can affect the radiative forcing of climate. In addition to the effects of the sources, regional transport can impact the light-absorbing ability through chemical processing or aging (Zhang et al., 2019). After BC particles are emitted, they can stay in the atmosphere for days or a few weeks (IPCC, 2021). During transport, fresh BC can experience a series of physical and chemical changes, for instance, mixing with other substances that can alter its microphysical and optical properties (Kahnert and Kanngießer, 2020). The aging processes can be even faster in polluted regions (Peng et al., 2016), and as a result, the light-absorbing ability of BC can be strongly affected. Indeed, the light absorption ability of BC after aging can be as much as 2.4 times that of fresh particles (Peng et al., 2016).

The concentrations of BC are controlled by local emissions, and regional transport, but meteorological conditions also are important because they affect both transport and removal. Normally, local emissions in urban areas are predictable to some degree because those emission sources are mainly anthropogenic and the concentrations of pollutants follow the diurnal patterns driven by anthropogenic activities. By contrast, meteorological conditions and regional transport are governed by multiple scales of motion which result in distinct meteorological impacts on ambient pollutant levels (Levy et al., 2010, Dutton, 1976). A commonly accepted classification of the scale of motion is based on horizontal distance and time scales. Typically, the time scale of local-scale motions varies from hours to days and the spatial scale ranges from 10^2 to 10^5 m (Oke et al., 2002; Seinfeld and Pandis, 2006). The local scales of motion are mainly controlled by local factors such as the roughness of the earth's surface, orography, land breeze/sea breeze circulation, etc. (Hewitson and Crane, 2006; IPCC, 2021). Larger scale of motions are associated with a mesoscale or synoptic scale weather systems, which on the one hand can transport pollutants but on the other can disperse them (Kalthoff et al., 2000; Zhang et al., 2012).

The relationships between atmospheric motions and pollutant concentrations are complex. Atmospheric motions determine where and how extensive the pollution impacts are, but of course the rates of pollutant emissions, especially local ones, are important, too (Dutton, 1976). Liao et al., (2020) found that synoptic-scale flow led to an enhanced $PM_{2.5}$ in a coastal area of the Pearl River Delta, while meso/local scale motions led to $PM_{2.5}$ pollution in an inland area. Levy et al. (2010) showed that the concentrations of NO_x and SO_2 were higher under the dominance of smaller-scale motions than under larger scale motions.

删除了: commonly…produced by the incomplete combustion of biomass and fossil fuels. The BC aerosolIt…has a strong light absorption capacity and can cause ability likely toto …eating of the atmosphere.,…In fact, BC is which has been …idely recognized as one of the most important short-lived life …limate forcers which can warm the climate

删除了: the second strongest light-absorbing substance in the atmosphere after CO_2 (Bond et al., 2013)

删除了: its …igh light-absorbing ability, BC has the considerable…potential to perturb the cause radiative perturbation in the …adiative balance between the earth and atmosphere.…and in so doing cause in the The balance is so important that breaking it will result…in climate to change drive , leading to further negative changes in the …cosystems away from their natural states (Schroter et all., 2005). Those changes ultimately will affect biodiversity and could threaten threaten …umans' food security and biodiversity

删除了: also an …mportant for cloud…nucleating clouds, and that is another way in which the particles can causenucleus leading to…indirect climatic effects after being activated …Jacobson, 2002). Aslthough

删除了: Thus, BC is also known as

删除了: a short-lived climate pollutant,

删除了: but

删除了: is…highly variable and dependent depending …n its distribution in the atmosphere, both horizontally and vertically; its radiative properties and how they are affected by of chemical processing; and its lifetime radiative efficiency and lifetime

删除了: may be variable because of …ifferences

删除了: A

删除了: Llocal

删除了: is

删除了: the…local emissions sources…and regional

删除了: at

删除了: in urban areas …ecause those emission sources

删除了: y

删除了: s…in a…distinct meteorological impacts on amb

删除了: (it is atmosphere phenomena)

删除了: is …ainly controlled by local factors such as the

删除了: aerosol concentration

删除了: A …l

删除了: is…associated with a mesoscale or synoptic scal

删除了: diffuse

删除了: ion is…complex. Atmospheric motions determi

删除了: decides

删除了: …impacts arecould be… but of course the rates

However, few studies have touched on the impacts of different scales of motion on BC and their effects on radiative efficiency even though the effects could cause rapid climatic effects due to the patchy and constantly changing distributions (IPCC, 2021).

Topography also plays an important role in air pollution (Zhao et al., 2015). River-valley topography is complicated, and it can have a considerable influence on air pollution and synoptic patterns of flow (Green et al., 2016; Carvalho et al., 2006). The pollution levels at cities in river-valleys are not only influenced by general atmospheric dynamics but also strongly impacted by the local-scale of dynamics (Brulfert et al., 2006). Surface albedo and surface roughness are affected by the the complex topography of river-valley regions, and those physical factors can affect circulation and cause changes in pollutant mass concentrations (Wei et al., 2020). Mountains also significantly affect pollution, and once pollutants are generated or transported into the river-valley regions, their dispersal can be impeded by the blocking effect of the mountains. Instead of being dispersed, they can be carried by the airflows over the mountains to converge at the bottom of the valley and increase the pollutants along the river (Zhao et al., 2015). In this way, pollutants can accumulate in valleys and spread throughout the area, thereby aggravating pollution. In addition, temperature inversions commonly form in river-valleys during the winter, and that, too, can aggravate pollution problems (Glojek et al., 2022 and Bei et al., 2016).

Thus, we focused our study on the impacts of different scales of motion on source-specific equivalent BCs (eBCs) and we evaluated radiative effects of eBCs over a river-valley city. The primary objectives of this study were: (1) to quantify the contributions of fossil fuel combustion and biomass burning to eBC concentrations, (2) to investigate the impacts of different scales of motion on the source-specific eBC, and (3) to estimate the radiative effects and the radiative efficiency of the source-specific eBC under different atmospheric motion scenarios. The study provides insights into the influence of the specified atmospheric motions on BC and highlights the effects of those motions on the radiative efficiency and potential climatic effects of the regionally transported BC.

2 Methodology

2.1 Research site

Baoji is a typical river-valley city, located at the furthest west of the Guanzhong Plain, at an altitude from 450 to 800 m a.s.l. (Figure S1). Baoji has a complex topography and often suffering from severe pollution in winter. It is surrounded by mountains to the south, west and north, with the Weihe River as the central axis extending eastward. The shape can be viewed as a funnel with large opening to east. The Qinling peaks and the flat Weihe Plain are the main landforms of Baoji. The main peak of the Qinling Mountains is 3,767 m a.s.l. and it is the highest mountain in the eastern part of mainland China. This terrain causes divergent flow at local scales, which can impact pollution levels (Wei et al., 2020). Baoji also is an important railway intersection in China, connecting six railways to the north-west and southwest China. Pollutant levels can be high and pollutants are not easy to be dispersed in the city due to its special topographic conditions, dense population (total population of 0.341 million, with 63.5% population living in the downtown aera and population density of 6003 people per km^2 in 2019 (http://tjj.shaanxi.gov.cn/upload/2021/zk/indexch.htm and https://data.chinabaogao.com/hgshj/2021/042053X932021.html), and impacts from major highway and railway networks.

删除了: its…radiative efficiency even though the effects it …ould cause lead to …apid climatic effects due to the patchy its uneven

删除了: The …r

删除了: of the river-valley city

删除了: which has

删除了: of the…river-valleys city …re not onlyis…influenced by general atmospheric dynamics and …but also strongly impacted by the local-

删除了: T…e complex topography of river-valley regions, and those physical factors can affect has uneven surface With the uneven solar radiation due to different albedo and surface roughness, it is easy to form…resulting in varieda different local scale of

删除了: but it

删除了: whichcan plays an important role in

删除了: O…ce pollutants are generated produced

删除了: they are it is hard to be dispersed them due to…the blocking effect of the mountains.,

删除了: and

删除了: i

删除了: then the pollutants

删除了: could

删除了: over…ver the mountains to the river-valley terra

删除了: accelerate…pollutants along the river (Zhao et al., 2015). In this way, pollutants can accumulate in valleys and spread throughout The valley not only performs as a drain for pollutants but also acts as a way for pollutants to enter …

删除了: in winter

删除了: ed…in winter …n the areas with …iver-valley

删除了: Mountains significantly affect pollution, since th

删除了: are …ocused ourkeen on studying

删除了: fascinated to …tudy on the impacts of different

删除了: their

删除了: the eBC contributions from fossil fuel combustic

删除了: featured …cales of motion on the source-specifi

删除了: with…an altitude varying…from 450 m a.s.l.…

删除了: Guanzhong Plain is surrounded by mountains to

删除了: of air movement …hich can produce

删除了: Mountains significantly affect pollution, since th

删除了: also…an important railway intersection in Chin

删除了: /

设置了格式: 上标

删除了: , it is not easy to disperse pollutants

The sampling site was on the rooftop of a building at Baoji University of Arts and Sciences (34°21′ 16.8″ N, 107°12′ 59.6″ E, 569 m a.s.l.) surrounded by commercial and residential buildings, highways, and a river, there were no major industrial emission sources nearby. The main sources of BC in Baoji were the domestic fuel (coal and biomass) burning as well as the motor vehicle emissions (Zhou et al., 2018; Xiao et al., 2014). Open fire also can be sources for BC, but there were limited fire found scattered around the site (Figure S2). The meteorological conditions at Baoji for the four seasons are listed in Table S1, and the wind roses for the different seasons are shown in Figure S3(data are from the Meteorological Institute of Shaanxi Province).

2.2 Sampling and laboratory measurements

eBC and the absorption coefficients (b_{abs}) at 370, 470, 520, 590, 660, 880, and 950 nm wavelength were measured using an AE33 aethalometer (Magee Scientific, Berkeley, CA, USA) equipped with a $PM_{2.5}$ cut-off inlet (SCC 1.829, BGI Inc. USA) that had a time resolution of 1 min. A Nafion® dryer (MD-700-24S-3; Perma Pure, Inc., Lakewood, NJ, USA) with a flow rate of 5 L min^{-1} was used to dry the $PM_{2.5}$ before the measurement. Briefly, the particles were dried by the Nafion® dryer before being measured with the AE33 aethalometer, and the deposited particles were irradiated by light-emitting diodes at seven wavelengths of light-emitting diodes (λ = 370, 470, 520, 590,660, 880, and 950 nm), and the light attenuation was detected. The non-linear loading issue for filter-based absorption measurement was accounted for in the AE33 by a technique called dual-spot compensation. The quartz filter (PN8060) matrix scattering effect was corrected by using a factor of 1.39. More details of AE33 measurement techniques can be found in Drinovec et al. (2015).

The scattering coefficient (b_{scat}) at a single (525) nm wavelength was measured with the use of a nephelometer (Aurora-1000, Ecotech, USA) that had a time resolution of 5 min. The nephelometer and aethalometer operated simultaneously and used the same $PM_{2.5}$ cyclone and Nafion® dryer. The calibration was conducted based on the user guide with a calibration gas R-134. Zero calibrations were conducted every other day by using clean air without particles. The ambient air was drawn in through a heated inlet with a flow rate of 5 L min^{-1}. The relative humidity remained lower than 60%.

$PM_{2.5}$ samples were collected for every 24 hours (h) from 10 a.m. local time to the 10 a.m. the next day from 16th November 2018 to 21st December 2018 with two sets of mini-volume samplers (Airmetrics, USA) , one using quartz fiber filters (QM/A; Whatman, Middlesex, UK) and the other with Teflon® filters (Pall Corporation, USA), both with a flow rate of 5 L min^{-1}. Those samples were kept in a refrigerator at 4°C before analysis. The mass concentration of K^+ in the $PM_{2.5}$ quartz sample was extracted in a separate 15 mL vials containing 10 mL distilled deionized water (18.2 MΩ resistivity). The vials were placed in an ultrasonic water bath and shaken with a mechanical shaker for 1 h to extract the ions and determined by a Metrohm 940 Professional IC Vario (Metrohm AG., Herisau, Switzerland) with Metrosep C6-150/4.0 column (1.7 mmol/L nitric acid+1.7 mmol/L dipicolinic acid as the eluent) for cation analysis. A group of elements (i.e. Mg, Al, Si, S, Cl, Ca, V, Mn, Fe, Ni, Cu, As, Se, Br, Sr, Pb, Ga, and Zn) on the Teflon® filters was were determined by energy-dispersive x-ray fluorescence (ED-XRF) spectrometry (Epsilon 4 ED-XRF, PANalytical B.V., Netherlands). The X-rays were generated from a gadolinium anode on a side-window X-ray tube. A spectrum of the ratio of X-ray and photon energy was obtained after 24 minutes of analysis for each sample with each energy peak characteristic of a specific element, and the peak areas were proportional to the concentrations of the elements. Quality control was conducted on a daily basis with test standard sample.

删除了: is

删除了: the…uilding at Baoji University of Arts and Sciences building at Baoji University …34°21′ 18.4…6.8″ N, 107°8…2′ 34.7

删除了: and … river, there weres

删除了: and

删除了: spots could

删除了: an…emission

删除了: of

设置了格式: 非突出显示

设置了格式: 非突出显示

设置了格式: 非突出显示

设置了格式

删除了: spots …ound scattered around the site (Figure S2). The meteorological conditions at Baoji for the fourof different…seasons are listed in Table S1, and the wind roses for theof…different seasons are showned

删除了: is

设置了格式: 非突出显示

删除了: .

删除了:

删除了: Equivalent BC (

删除了:)

删除了: via…a $PM_{2.5}$ cut-off inlet (SCC 1.829, BGI Inc. USA) that hadwith

删除了: 5

删除了: with …even wavelengths of light-emitting diodes (λ = 370, 470, 520, 590,660, 880, and 950 nm), and the light attenuation was detected. The non-linear loading issue for filter-based absorption measurement was accounted for in the AE33 is solved …y a technique in AE33

删除了: 2.14…

删除了: by … nephelometer (Aurora-1000, Ecotech, USA) that had with … time resolution of 5 min during the study period… The nephelometer and aethalometerIt…operated simultaneously and used with AE33 using…the same $PM_{2.5}$ cyclone and Nafion® dryer. A single wavelength (525nm) was used to measure the scattering coefficient.

删除了: of …as conducted based on the user guide witha

删除了: with

删除了: (xxx)

删除了: The…Zz…ro calibrations were was…conducte

删除了: by…two sets of mini-volume samplers (Airmetr

删除了: with an IonPac CS12A column (20m methane

删除了: E…ements (i.e. Mg, Al, Si, S, Cl, Ca, V, Mn, Fe

删除了: ing sample PAT-3195

Organic carbon (OC) and elemental carbon (EC) in each sample were determined with the use of a DRI Model 2001 Thermal/Optical Carbon Analyzer (Atmoslytic Inc., Calabasas, CA, USA). The thermal/optical reflectance (TOR) method and IMPROVE_A protocol were used for analysis. A punch of a quartz filter sample was heated at specific temperatures to obtain data for four OC fractions and three EC fractions. Total OC was calculated by summing all OC fractions and the pyrolyzed carbon (OP) produced. Total EC was calculated by summing all EC fractions minus the OP. Detailed methods and quality assurance/quality control processes were described in Cao et al., (2003). Primary organic carbon (POC) was estimated by using the minimum R-squared (MRS) method, which is based on using eBC as a tracer (Text S1). The method uses the minimum R^2 between OC and eBC to indicate where the ratio for which secondary OC and eBC are independent. A detailed description of the MRS method can be found in Wu et al., (2016).

Data for NO_x, wind speed, and direction at 12 ground monitoring sites were downloaded from http://sthjt.shaanxi.gov.cn/hx_html/zdjkqy/index.html. The wind data at 100 meters (m) above the ground and the planetary boundary layer height were downloaded from https://rda.ucar.edu/datasets/ds633.0. The data used for the HYSPLIT air mass trajectory analyses was downloaded from Global Data Assimilation System and it had a resolution of 1°×1°(GDAS, https://www.ready.noaa.gov/gdas1.php). The data and main parameters used in trajectory model are listed in Table S2.

2.3 Optical source apportionment

The positive matrix factorization (PMF) model that was used for the optical source apportionment in this study. PMF solves chemical mass balance by decomposing the observational data into different source profiles and contribution matrices as follows:

$$X_{ij} = \sum_{k=1}^{p} g_{ik} f_{kj} + e_{ij} \qquad (1)$$

where X_{ij} denotes the input data matrix; p is the number of sources selected in the model; g_{ik} denotes the contribution of the k^{th} factor to the i^{th} input data; f_{kj} represents the k^{th} factor's profile of the j^{th} species; and e_{ij} represents the residual. Both g_{ik} and f_{kj} are non-negative. The uncertainties of each species and $b_{abs}(\lambda)$ were calculated by the equation recommended in EPA PMF5.0 user guideline(Norris et al, 2014) as follows:

$$Unc = \sqrt{(error\ fraction \times concentration(or\ ligth\ absorption\ coefficient))^2 + (0.5 \times MDL)^2} \qquad (2)$$

$$Unc = \frac{5}{6} \times MDL \qquad (3)$$

where MDL is the minimum detection limit of the method. When the concentration of a species was higher than the MDL then equation (2) was used otherwise equation (3) was used. In equation (2), for calculating the uncertainty of a chemical species, the error fraction was multiplied the concentration of the species. For calculating the uncertainty of optical data, the error fractions were multiplied by the light absorption coefficients.

Chemical species data (EC, POC, K^+, Mg, Al, Si, S, Cl, Ca, V, Mn, Fe, Ni, Cu, As, Se, Br, Sr, Pb, Ga and Zn) and the primary absorption (Pabs) data at λ=370nm,470nm,520nm,660nm, and 880nm were used for PMF analysis. The error fraction of offline measured data was the difference between multiple measurements of the same sample. The error fraction used for optical data

删除了: by
删除了: different
删除了: produced
删除了: pyrolyzed carbon (OP)
删除了: method
删除了: It
设置了格式: 非突出显示
删除了: of
删除了: is
删除了: referred to
删除了: The
删除了: i
删除了: with
删除了: ,
删除了: t
删除了: HYSPLIT
删除了: were
删除了:
域代码已更改
删除了:
删除了: (Norris et al, 2014)
删除了:
删除了:
带格式的: 两端对齐
删除了: F
设置了格式: 上标
删除了: put
删除了: in PMF
删除了: is
删除了: the measured values

was 10% based on Rajesh and Ramachandran (2018). PMF solves the equation (1) by minimizing the Q value, which is the sum of the normalized residuals' squares, as follows,

$$Q = \sum_{i=1}^{n}\sum_{j=0}^{n}\left[\frac{e_{ij}}{u_{ij}}\right]^{2} \qquad (4)$$

where u_{ij} represents the uncertainties of each X_{ij} and Q_{true}/Q_{exp} was used as the indicators for the factor number determination.

2.4 eBC source apportionment

The quantities of eBC generated from biomass burning versus fossil fuel combustion were deconvolved by an aethalometer model which uses Beer-Lambert's Law to write the absorption coefficients equations, wavelengths and absorption Ångström exponents (AAEs) for the two different BC emission sources (Sandradewi et. al., 2008). This approach is widely used for separating BC from two different sources based on optical data (Rajesh et al., 2018; Kant et al., 2019; Panicker et al., 2010). However, the traditional aethalometer model could be affected by the light absorbing substances at lower wavelengths such as dust and secondary formation particles. An improvement to the traditional aethalometer model was made, by explicitly considering the interference of the b_{abs} at a lower wavelength (370nm) caused by dust and secondary OC. Thus, the calculation of the absorption and source apportionment was based on the following equations (Wang et al., 2020):

$$\frac{b_{abs}(370)_{fossil}}{b_{abs}(880)_{fossil}} = \left(\frac{370}{880}\right)^{-AAE_{fossil}} \qquad (5)$$

$$\frac{b_{abs}(370)_{biomass}}{b_{abs}(880)_{biomass}} = \left(\frac{370}{880}\right)^{-AAE_{biomass}} \qquad (6)$$

$$b_{abs}(880) = b_{abs}(880)_{fossil} + b_{abs}(880)_{biomass} \qquad (7)$$

$$b_{abs}(370) = b_{abs}(370)_{fossil} + b_{abs}(370)_{biomass} + b_{abs}(370)_{secondary} + b_{abs}(370)_{dust} \qquad (8)$$

$$eBC_{fossil} = \frac{b_{abs}(880)_{fossil}}{MAC_{BC}(880)_{fossil}} \qquad (9)$$

$$eBC_{biomass} = \frac{b_{abs}(880)_{biomass}}{MAC_{BC}(880)_{biomass}} \qquad (10)$$

where AAE_{fossil} and $AAE_{biomass}$ are the AAEs for fossil fuel combustion and biomass burning. These were derived from the optical source apportionment by using PMF as discussed in section 3.1. Further, $b_{abs}(370)$ and $b_{abs}(880)$ are the total b_{abs} measured by the AE33 at the wavelengths of 370 nm and 880 nm respectively; $b_{abs}(370)_{fossil}$ and $b_{abs}(880)_{fossil}$ are the b_{abs} caused by emissions from fossil fuel combustion at those two wavelengths; $b_{abs}(370)_{biomass}$ and $b_{abs}(880)_{biomass}$ are the b_{abs} caused by emissions from biomass burning at those two wavelengths; $b_{abs}(370)_{dust}$ refers to the b_{abs} contributed by mineral dust at the wavelength of 370 nm, which was derived from the result of optical source apportionment; $b_{abs}(370)_{secondary}$ refers to the b_{abs} caused by the secondary aerosols at the wavelength of 370 nm, which was calculated by the minimum R-squared approach with eBC as a tracer (Text S1, Wang et al., 2019); eBC_{fossil} and $eBC_{biomass}$ are the eBCs from fossil fuel combustion and biomass burning; and $MAC_{BC}(880)_{fossil}$ and $MAC_{BC}(880)_{biomass}$ are the mass absorption cross-sections of eBC_{fossil} and the mass absorption cross-section of $eBC_{biomass}$ at the wavelength of 880 nm respectively, which were based on the PMF results for the optical source apportionments.

删除了: is
删除了: (
删除了: ,
删除了: ”
删除了: where MDL is the minimum detection limit of data. The error fraction of offline measured data is the difference between the measured values of the same sample. The error fraction of offline measured data is the difference between the measured values of the same sample.
删除了: An error fraction of 0.1 was used for online data (Rai et al., 2020).
删除了: as follows
删除了: :
删除了: ere
带格式的: 两端对齐
删除了:
删除了: and
删除了: separated
删除了: (Sandradewi et. al., 2008)
删除了: . Aethalometer model
删除了: about
删除了: of
删除了: interfered
删除了: Different from
删除了: an improvement has been made
删除了: giving consideration to
删除了: conducted by
删除了: y
删除了: .
删除了: were
删除了: .
删除了: .
删除了: .
删除了: .
删除了: were
删除了: of
设置了格式: 非突出显示
删除了: .
删除了: calculated
删除了: of
删除了: using PMF

2.5 Indicators for the different scales of motion

The mathematical definitions of airflow condition proposed by Allwine and Whiteman (1994) were used in this study. The definitions quantify the flow features integrally at individual stations. Three variables were quantified, namely the actual wind run distance (S) which is the scalar displacement of the wind in 24 h (i.e. the accumulated distance of the wind), the resultant transport distance (L) which is the vector displacement of the wind in 24 h (i.e. the straight line from the starting point to the end point), and the recirculation factor (R) is based on the ratio of L and S which indicates the frequency of the wind veering in 24 h. The influences of different scales of atmospheric motions were assessed based on the method proposed by Levy et al., (2010), and for this, we used wind data at 100 m above the sampling site and the wind data from 12 monitoring stations at ground level (~15m) to indicate the different scales of motions. The winds at the surface monitoring stations were expected to be more sensitive to local-scale turbulence and convection than the winds at 100 m. With less influence from the surface forces, the indicators at 100 m would be more sensitive to larger scales of motion. The equations used as follows:

$$L_{n\tau/bj} = T\left[\left(\sum_{j=i}^{i-\tau+1} u_i\right)^2 + \left(\sum_{j=i}^{i-\tau+1} v_i\right)^2\right]^{1/2} \tag{11}$$

$$S_{n\tau/bj} = \sum_{j=i}^{i-\tau+1}\left(u_j^{\,2} + v_j^{\,2}\right)^{1/2} \tag{12}$$

$$R_{n\tau/bj} = 1 - \frac{L_{i\tau}}{S_{i\tau}} \tag{13}$$

where T is the interval of the data (i.e., 60 min), i is the i^{th} the ending time step data, τ is the integration time period of the wind run (24 h), i-τ+1 represents the data at the start time, and n is the number of monitoring stations (a total of 12 in this study). The quantities u and v are the wind vectors. Using the wind data from the 12 monitoring stations covering Baoji, the L and S values at the 12 different sites at ground level were calculated. $L_{n\tau}$ and $S_{n\tau}$ represent the resultant transport distance and the actual wind run distance at the n^{th} (n = 1 to 12) monitoring station at ground level; $R_{n\tau}$ is the recirculation factor at the n^{th} monitoring station which is calculated based on $L_{n\tau}$ and $S_{n\tau}$. L_{bj}, and S_{bj} are the resultant transport distance and the actual wind run distance at 100 m height above the ground. These represent the flow characteristics in higher atmosphere at the study site, and they were calculated by using the wind data at 100 m height. The recirculation factor (R_{bj}) was calculated for a height of 100 m.

As explained in Levy et al., (2010), if local-scale motions are strong and regional-scale motions are weak, the variations in winds at each station would not be likely to be uniform due to differences in local factors, and that would result in a relatively large standard deviations (R_{std}) for $R_{n\tau}$. By contrast, if the local-scale motions are weak and the regional-scale motion is strong, the wind direction would be likely to be more uniform over a large area, and the R_{bj} and the R_{std} should be relatively smaller.

2.6 Self-organizing map

A self-organizing map (SOM) developed by Kohonen (1990) is a type of artificial neural network that is widely used for categorizing high-dimensional data into a few major features (Stauffer et al., 2016 and Pearce et al., 2014). In particular, this approach is widely used for categorizing different meteorological patterns (Liao et al., 2020; Han et al., 2020; Jiang et al., 2017). Unlike traditional dimension reduction methods (e.g., principal component analysis), SOM projects high-dimensional input data by non-linear projection into user-designed lower-dimensions, which are typically two-dimensional arrays of nodes

删除了: strength

删除了: ratio …R) is based on the ratio ofof…L and S which indicates the difference between the wind run distance and the actual resultant distance, representing ...

删除了: To distinguish …t…e influences of different scales of atmospheric motions were assessed, ...

删除了: featured

删除了: height… With less influence from the of…surface forces, the indicators at 100 m would be more sensitive to larger scales of motion. The Equations …quations used a ...

删除了: is

删除了: number of

删除了: With

删除了: ed

删除了: the ratio …alculated based onby ...

删除了: .

设置了格式: 字体：非倾斜，非上标/ 下标

删除了: to

删除了: higher …n the ...

删除了: which was…calculated by using the wind data at 100 m height. The recirculation factor (R_{bj} ...

删除了: i

删除了: s the recirculation factor ratio at…100 m height ...

删除了: calculated using L_{bj} and S_{bj}

删除了: is…strong and regional-scale motions are is ...

删除了: then winds at each monitoring site would be mainly controlled by local-scale motion. …T ...

删除了: of …inds at each station would not be likely to be uniform due to differences int…local factors, and that would so that will ...

删除了: ing

删除了: of the

删除了: calculated by using the wind speed and direction data from the 12 monitoring stations in Baoji

删除了: Otherwise

删除了: is

删除了: influence caused by small-scale differences would be …eak and theened…, ...

删除了: one … type of artificial neural network that i developed by Kohonen (1990), which i… widely used for categorizing high-dimensional data into a few major features (Stauffer et al., 2016 and Pearce et al., 2014). In particular, this approachIt…is widely used for categorizing different meteorological patterns (Liao et al., 2020; Han et al., 2020; Jiang et al., 2017). UnlikeDifferent from the…traditional dimension reduction methods (e.g., principal component ...

带格式的: 行距：1.5 倍行距

(Hewitson and Crane, 2006). The performance of SOM in classifying climatological data has been shown to be robust (Reusch et al., 2005). Competitive learning algorithms are used to train SOM, and the architecture of SOM consists of two layers; one is called the input layer and it contains the high dimensional input data. The other layer is the output layer in which the node number is the output cluster number. The working principle of SOM is to convert high dimensional data with complex correlations into lower dimensions via geometrical relationships (Ramachandran et al., 2019). After the initial random weights are generated, the input data are compared with each weight, and the best match is defined as winning. The winning node and the neighboring nodes close to the winning node will learn from the same inputs and the associated weights are updated. After multiple iterations, the network to settles into stable zones of features and the weights. More detailed working principles of SOM can be found Kangas and Kohonen, (1996) and Kohonen et al., (1996).

Comparison between the input data and each weight is made by applying Euclidean distances, the best match is defined by the following equation:

$$\|x - m_c\| = min\{\|x - m_i\|\} \tag{14}$$

where x is the input data, m_c is the best matched weight, m_i is the weights connected with the i^{th} node.

The weights are updated by following equation:

$$m_i(t+1) = m_i(t) + h_{ci}(t)[x(t) - m_i(t)] \tag{15}$$

where the $m_i(t+1)$ is the i^{th} weight at t+1 time, $m_i(t)$ is the i^{th} weight at t time, the $h_{ci}(t)$ is the neighborhood kernel defined over the lattice points at t time, and c is the winning node location.

SOM was used to categorize the daily atmospheric motions during the study period and to explore the influences of different scales of motion on source-specific eBC. Hourly averages of three sets of data (R_{std}, L_{bj}, and S_{bj}) were input into SOM. Determining the size of the output map is crucial for SOM (Chang et al 2020 and Liu et al., 2021). To reduce the subjectivity, the K-means cluster method was used for the decision-making regarding size. The similarity of each item of the input data relative to the node was measured using Euclidean distance. The iteration number was set to 2000. For each input data item, the node closest to it would "win out". The reference vectors of the winning node and their neighborhood nodes were updated and adjusted towards the data. The "Kohonen" package in *R* language (Wehrens and Kruisselbrink, 2019) was used to develop the SOM model in this study.

2.7 Estimations of direct radiative effects and heating rate

The Santa Barbara DISORT Atmospheric Radiative Transfer (SBDART) model was used to estimate the direct radiative effects (DRE) induced by source-specific eBC. The model has been used in many studies to calculate the DRE caused by aerosols and BC (Pathak et al., 2010; Rajesh et al., 2018; Zhao et al., 2019). SBDART calculated DRE based on several well-tested physical models. Details regarding the model were presented in Ricchiazzi et al., (1998). The important input data included aerosol parameters, including aerosol optical depth (AOD), single scattering albedo (SSA), asymmetric factor (AF) and extinction efficiency, surface albedo, and atmospheric profile.

删除了: by non-linear projection …Hewitson and Crane, 2006). The performance of SOM Its performance…in classifying climatological data has been shown to beshow

删除了: result

删除了: is trained by competitive learning algorithm…and.…T…

删除了: ,

设置了格式: 字体: 10 磅, 字体颜色: 自动设置

设置了格式: 字体: 10 磅, 字体颜色: 自动设置

删除了: which

设置了格式: 字体: 10 磅, 字体颜色: 自动设置

设置了格式

删除了: se

删除了: non-linear and…complex correlations of high dimensional data

设置了格式: 字体: 10 磅, 字体颜色: 自动设置

设置了格式

删除了: every

删除了: will be

删除了: every

设置了格式: 字体: 10 磅, 字体颜色: 自动设置

设置了格式: 字体: 10 磅, 字体颜色: 自动设置

设置了格式: 字体: 10 磅, 字体颜色: 自动设置

设置了格式: 字体: 10 磅, 字体颜色: 自动设置

设置了格式

删除了: will be …pdated. After iterating over …ultiple

删除了: with their

设置了格式: 字体: 10 磅, 字体颜色: 自动设置

设置了格式

删除了: The …c

设置了格式: 字体: 10 磅, 字体颜色: 自动设置

设置了格式

设置了格式

设置了格式

设置了格式

设置了格式

设置了格式

设置了格式

删除了: Therefore, …OM was usedconducted…to categ

删除了: T

删除了: e determination,…the K-means cluster method v

删除了: T…e model were presentedwas elaborated

删除了: includes …ncluded aerosol parameters, includin

删除了: contain

The aerosol parameters used in this study were derived by the Optical Property of Aerosol and Cloud (OPAC) model (Hess et al., 1998) based on the number concentrations of aerosol components. As the study was conducted in an urban region, the urban aerosol profile was used in OPAC, and it included soot (eBC), water-soluble matter (WS), and water-insoluble matter (WIS). The number concentrations of soot were derived from the mass concentrations of eBC with the default ratio (5.99E-5 μg m^{-3}/ particle.cm^{-3}) in OPAC. The number concentrations of WS and WIS were adjusted until the modeled SSA and b_{abs} at 500nm in OPAC were close (±5%, see Figure S4) to those values calculated with data from the nephelometer and AE33 ($b_{ext}(520) = b_{scat}(525) + b_{abs}(520)$, SSA= $b_{scat}(525)/b_{ext}(520)$). The DRE of source-specific eBC at the top of atmosphere (TOA) and surface atmosphere (SUF) were calculated from the difference between the DREs with or without the number concentrations of the source-specific eBC under clear-sky conditions.

$$DRE_{eBC} = (F\downarrow - F\uparrow)_{with\ eBC} - (F\downarrow - F\uparrow)_{without\ eBC} \quad (16)$$

$$DRE_{eBC,ATM} = DRE_{eBC,TOA} - DRE_{eBC,SUF} \quad (17)$$

where DRE_{eBC} is the DRE of source-specific eBC, $F\downarrow$ and $F\uparrow$ are the downward and upward flux, $DRE_{eBC,ATM}$ is the DRE of the source-specific eBC for the atmospheric column, that is, the DRE at the top of the atmosphere ($DRE_{eBC,TOA}$) minus that at the surface ($DRE_{eBC,SUF}$).

3 Results and discussion

3.1 Calculation of eBC$_{fossil}$ and eBC$_{biomass}$

The PMF model was used for the optical source apportionment, and those results were used to obtain the site-specific AAEs and MACs, which in turn were used to calculate the source-specific eBC with the improved aethalometer model. For every solution, PMF was run 20 times. The Q_{true}/Q_{exp} ratios from the 2- to 7-factor solutions were examined, and the values of a 4-factor solution were found most stable compared with others because the Q_{true}/Q_{exp} values did not drop appreciably after the addition of one more factor (Figure S5). Based on these results, the 4-factors solution was determined to be the most interpretable. Two diagnostic methods, Bootstrap (BS) and Displacement (DISP) (Norris et al, 2014; Brown et al. 2015) were used to validate the robustness and stability of the results. The BS method was used to assess the random errors and partially assess the effects of rotational ambiguity while DISP was used to evaluate rotational ambiguity errors. The results of the BS and DISP analyses showed that there was no swap for the 4-factor solution (Table S3). The modelled primary $b_{abs}(\lambda)$ were well correlated (r = 0.95–0.96, slope = 0.90~0.95, p < 0.01, Figure S6) with their observed counterparts, which suggested that the modelling performance of PMF5.0 was good. The factor profiles obtained from the PMF are shown in Figure 1.

The first factor (PC1) had was featured with high loadings of EC (52%), POC (49%), and V (49%) and moderate loadings of Mn (33%), Ni (40%), Cu (37%), and Zn (44%). This factor source contributed 27% to 44% of the primary $b_{abs}(\lambda)$. Of the species with high loadings on PC1, EC has been found to be associated with vehicular emissions due to incomplete fuel combustion (Cao et al., 2013). V and Ni are commonly detected in the particles emitted by diesel-powered vehicles (Lin et al., 2015 and Zhao et al., 2021). Mn compounds are commonly used as an antiknock additive for unleaded gasoline to raise octane numbers and protect the engine (Lewis et al., 2003; Geivanidis et al., 2003); and Cu and Zn are emitted by the combustion of lubricating

删除了: A…rosol parameters used in this study were derived by the Optical Property of Aerosol and Cloud (OPAC) model (Hess et al., 1998) based on the number concentrations of aerosol components. AsSince…the study was conducted in the …n urban region, the urban aerosol profile was used in OPAC, and it includedwhich includes

删除了: was

删除了: μg m^{-3}

设置了格式: 字体: 10 磅

删除了: the model… The number concentrations of WS and WIS were adjusted until the modeled SSA and b_{abs} at 500nm in OPAC were close (±5%, see Figure S42

设置了格式: 上标

删除了: was

删除了: 4

删除了: 5

删除了: at

删除了: of…the whole …tmospheric columne… that is, which is equal to

删除了: minuses

删除了: To obtain the site-specific AAEs and MACs for calculating the source-specific eBC with the improved aethalometer model, the PMF model was used for the optical source apportionment.

删除了: ed

删除了: factors solution

删除了: s

删除了: was

删除了: s

删除了: was …ere found most stable compared with others because the Q_{true}/Q_{exp} values did not drop appreciably after the addition ofadding

删除了: S3

删除了: Thus, a…4-factors solution source number …as determined to be the most interpretable. Two diagnostic methods, Bootstrap (BS) and Displacement (DISP) (Norris et al, 2014; Brown et al. 2015) were used tT

删除了: understand

删除了: , two diagnostic methods, which are Bootstrap (

删除了: Bootstrap (BS) and Displacement (DISP) metho

设置了格式: 非突出显示

删除了: ~

删除了: S4

删除了: given by

删除了: High amounts of …C has been found to be were

删除了:). …u and Zn are emitted by were found in …he oils and from the wear of motor vehicle parts (i.e., brakes and tires) (Thorpe and Harrison, 2008; Song et al., 2006). In addition, the EC associated with this factor was found well correlated (r = 0.83, p < 0.01, Figure S7) with the daily averaged NO$_x$ which is a commonly used tracer of vehicular emissions in the urban areas (Zotter et al., 2017). Recent research on the source contributions of BC emissions has shown that most of BC associated with transportation was emitted by on-road diesel vehicles in China (Xu et al., 2021). From these results, PC1 was identified as diesel vehicular emissions. The MAC of this factor (MAC (880)$_{diesel}$) was 6.7 m^2 g^{-1}. The estimated AAE of this factor (AAE$_{diesel}$) was 1.07 (Figure S8), which is comparable with the AAE values of vehicle emissions (0.8~1.1) reported in previous studies (Zotter et al., 2017; Kirchstetter et al., 2004).

The second factor (PC2) was characterized by the high loadings of K$^+$ (51%), Cl (79%), and Br (52%) and moderate amounts of EC (26%), POC (28%), and Pb (30%). Of these, K$^+$ is a widely recognized tracers for the biomass burning emissions (Urban et al., 2012; Zhang et al., 2015), and high loadings of Cl also can be taken as a signal of biomass burning (Yao et al., 2002; Manousakas et al., 2017). Previous studies showed that a large quantity of Br was found in biomass burning aerosols was caused by emissions of CH$_3$Br emission during combustion (Manö and Andreae, 1994; Artaxo et al.,1998). Particulate matter emitted from biomass burning typically has substantial amounts of OC and EC (Song et al, 2006), and Pb also has been observed in biomass-burning aerosols (Amato et al., 2016). Thus, PC2 was identified as emissions from biomass burning. The contribution of this factor to primary b_{abs}(370) was as high as 50%, but only 33% to primary b_{abs}(880), and that was likely caused by the brown carbon which is a typically found in biomass-burning aerosols (Washenfelder et al., 2015; Yan et al., 2015). The MAC of this factor (MAC (880)$_{biomass}$) was 9.5 m^2 g^{-1}. The AAE of this factor (AAE$_{biomass}$) was 2.13 (Figure S8), which is consistent with the wide range of AAEs reported for biomass-burning (1.2~3.5) (Sandradewi et al., 2008; Helin et al., 2018; Zotter et al., 2017).

The third factor (PC3) had significant loadings of S (64%), Se (98%), As (51%), and Pb (53%) and moderate loadings of Ga (42%)—all of these elements are commonly associated with coal combustion (Hsu et al., 2016; Tan et al., 2017). For instance, coal combustion has gradually become the main source of Pb in PM$_{2.5}$ after China began to phase out Pb-containing gasoline (Xu et al. 2012). Thus, PC3 was assigned to coal combustion. The MAC of this factor (MAC (880)$_{coal}$) was 7.5 m^2 g^{-1}. This factor contributed 17%–19% primary b_{abs}(λ), and its derived AAE$_{coal}$ was 1.74 (Figure S8) which is close to the AAE found for coal-chunks (Sun et al., 2017).

The last factor (PC4) was most heavily loaded with Al (68%), Si (76%), Ca (65%), Fe (51%), and Sr (71%). These elements are typical crustal elements, and they are abundant in mineral dust (Tao et al., 2016; Tao et al., 2017). Minor amounts of EC in crustal dust could be from other EC that had deposited on the ground and later resuspended together with the dust by natural or artificial disturbances (e.g., wind and traffic flow). This factor only contributed ~4% of the primary b_{abs}(λ). The estimated AAE$_{dust}$ was 1.78 (Figure S8) which is close to the AAE of mineral dust reported in previous studies (AAE$_{370\sim950}$ = 1.82, Yang et al., 2009).

As elaborated above, the PM$_{2.5}$ EC over Baoji was mainly from diesel vehicular emissions, biomass burning, and coal combustion. The emissions can be further grouped into those from biomass burning and fossil fuel combustion (the sum of diesel vehicular emissions and coal combustion). Thus, the AAE$_{fossil}$ (1.26) and MAC (880)$_{fossil}$ (7.1 m^2 g^{-1}) were calculated was the mass-weighted averages (relative to the total EC) of AAE$_{coal}$ (MAC (880)$_{coal}$) and AAE$_{diesel}$ (MAC (880)$_{diesel}$) (Table S4). The hourly mass concentrations of eBC$_{fossil}$ and eBC$_{biomass}$ were then calculated using the 'aethalometer model' (Eqs. 5–

删除了: ing
删除了: S5
删除了: data…which is a commonly used tracer of vehicular emissions in the urban areas (Zotter et al., 2017). According to …r…cent research on the source contributions of BC emissions has shown that most, the majority…of BC associated with from…transportation was emitted by on-road diesel vehicles in China (Xu et al., 2021). From these results, PC1Owing to those results above, this factor…was identified diesel vehicular ...
删除了: e
设置了格式: 非突出显示
删除了: one of the… widely recognized tracers for the emissions of…biomass burning emissions (Urban et al., Zhang et al., 2015), and h. H…gh loadings of Cl also can be taken as a signal of biomass burning (Yao et al., 2002; Manousakas et al., 2017). Previous studies showed report ...
删除了: ies
删除了: amount…of Br was found in biomass burning aerosols was caused by emissions of because of the…CH$_3$Br emission during combustion (Manö and Andreae, 1994; Artaxo et al.,1998). Particulate matter emitted from biomass burning typically has substantial amounts of OC and EC are commonly found in particulate matter emitted from biomass burning as major substances…(Song et al, 2006), and.…Pb has been was also…observed in biomass-burning aerosols (Amato et al., 2016). Thus, PC2 was identified as emissions from biomass burning. The contribution of this factor to ...
删除了: that
删除了: the
删除了: Wang et al., 2019
删除了: ,… the contribution of this factor to primary ...
设置了格式: 非突出显示
删除了: fell in …he wide range of biomass-burning ...
删除了: presented …ignificant loadings of S (64%), Se ...
删除了: to be
删除了: As …hina began to phase out Pb-containing ...
删除了: of
设置了格式: 非突出显示
删除了: is dominated by the contributions of…Al (68%) ...
设置了格式: 非突出显示
删除了: in PM$_{2.5}$ …ver Baoji was mainly from diesel ...
删除了: were
删除了: was
删除了: was
删除了: ere…s the mass-weighted averages (relative to t ...
删除了: S2
设置了格式: 非突出显示

10). The results showed that eBC_{fossil} and $eBC_{biomass}$ were only weakly correlated (r = 0.3, Figure S9), indicating a reasonably good separation, and furthermore, their diel variations showed different patterns (Figure 2).

The mean values of eBC_{fossil} and $eBC_{biomass}$ were 2.46 μg m^{-3} and 1.17 μg m^{-3}, respectively. The averaged total eBC mass concentration (± standard deviation) was 3.63±2.73μg m^{-3} , and the eBC ranged from varying from 0.39 to 12.73 μg m^{-3} during the study period, The averaged mass concentration was comparable to that in Lanzhou, another river valley city in China, that was sampled in the same season (5.1 ± 2.1, Zhao et al.,2019). The lowest value is comparable to other river valley regions such as in Retje in India (Glojek et al., 2022) or in Urumqi River Valley in China (Zhang et al., 2020), however even the highest concentration was much lower than that in other urban regions (Table S5).

The diel variations of eBC_{fossil} (Figure 2a) showed a bimodal pattern with two peaks at 9 a.m. and 7 p.m local time. which are typical peak commuting hours, indicating that there were strong influences from traffic emissions. Due to the reduced traffic flow from 1 a.m. to 5 a.m., eBC_{fossil} decreased slowly. After 5 a.m. passenger vehicles were allowed on the highways in and near Baoji, and eBC_{fossil} started to rise, probably in response to the increased traffic emissions. As the morning commuter traffic increased, eBC_{fossil} reached its first peak at 9 a.m. From then until 11 a.m., eBC_{fossil} declined only slightly because the wind speeds decreased (Figure 2c), which offset the effects of the decreases in traffic. From 11 a.m. to 3 p.m., the increases in the height of the planetary boundary layer (PBLH) (Figure 2d) led to a rapid decrease in eBC_{fossil}. Later the PBLH decreased rapidly, resulting in conditions unfavorable for dispersion, and then eBC_{fossil} rose quickly to the second peak at 7 p.m. After passing the evening peak in traffic, the eBC_{fossil} decreased dramatically.

In contrast, the diel variation of $eBC_{biomass}$ (Figure 2b) showed greater influences from meteorological conditions during the daytime, and $eBC_{biomass}$ showed lower concentrations during the day compared with the night. After 6 p.m., increased biomass burning from cooking and residential heating let to the emission of more $eBC_{biomass}$ and the stable PBLH hindered the dispersion of $eBC_{biomass}$; these two factors caused the $eBC_{biomass}$ to reach its peak at 8 p.m. At night, the downslope winds from the mountains converged in the valley at night time (Oke et al., 2002) and turned easterly, where the land altitude is lower than at Baoji (Zhao et al., 2015). This led to t relatively strong winds (Figure 2c) favored dispersion and caused the measured $eBC_{biomass}$ pollutant levels to decrease.

3.2 The influence of regional and local atmospheric motion on eBC_{fossil} and $eBC_{biomass}$

The K-means results showed that the four-category solution was appropriate for interpretation as explained above (see also Figure S10). Thus a 2×2 map size was used for the self organizing map (SOM). The four featured atmospheric motion categories given by SOM (Figure S11) were identified as follows (feature values are in Table 1):

1. Local-scale dominance (LD): This category featured high R_{bj} and R_{std}. As described in section 2.5, high R_{std} indicates greater divergence of R at the 12 stations due to the strong influence of local-scale turbulence and convection. L_{bj} and S_{bj} were shorter than 130km implying stagnation (Allwine and Whiteman, 1994).

删除了: barely shared a …orrelation ...

删除了: p < 0.01,

删除了: S6…9), indicating a reasonably good separation, and furthermore, ...

删除了: T…eir dieldiurnal…variations showed …different patternsvaried, however ...

删除了: to…another river valley city in China, that was sampled in the same season (5.1 ± 2.1, Zhao et al.,2019). The lowest value is comparable to other river valley regions such as in Retje in India (Glojek et al., 2022) orand ...

删除了: H

删除了: is…much lower than that in other most ...

设置了格式: 非突出显示

删除了:

删除了: diurnal

删除了: were …re typical peak commuting peak …ours, indicating that there were in cities, indicating a ...

删除了:

删除了: of…traffic emissions. Due to the reduced traffic flow from 1 a.m. to 5 a.m., eBC_{fossil} decreased slowly. After 5 a.m. passenger vehicles were allowed on the highways in and near Baoji, and eBC_{fossil} started to rise, probably in response to the increased traffic emissions. perhaps owing to pollutant transport from nearby highways. …s the morning commuter traffic increased peak led to increased vehicles on the road in the city… eBC_{fossil} reached its first peak at 9 a.m. From then 9 a.m.…untilto…11 a.m., eBC_{fossil} only …eclined only slightly because the reduced …ind speeds decreased (Figure 2c), which offset the effects of the decreasesdecline…in traffic flow… From 11 a.m. to 3 p.m., the increases in the height of thed…planetary boundary layerr height…(PBLH) (Figure 2d) led to a rapid decrease inof ...

删除了: s…ecreased rapidlyhrank fast… resulting in conditions unfavorable for dispersion, and then eBC_{fossil} rose quickly to therising and the evening traffic peak, coupled with the undesirable dispersion conditions, helped eBC_{fossil} skyrocket to its…second peak at 7 p.m. After passing the ...

删除了: New para here

删除了: By

删除了: diurnal

删除了: more …nfluences from meteorological conditions during the daytime, and $eBC_{biomass}$ showed demonstrating ...

删除了: ies…solution was more ...

删除了: S7

删除了: in SOM

删除了: S8

删除了: average L_{bj} = 70.9 km, S_{bj} = 107.8 km, R_{bj} = 0.35, R_{std} = 0.25.

删除了: s…high R_{bj} and R_{std}. As described in section 2.5, high R_{std} indicates greater divergence of R at thein ...

2. Local-scale strong and regional-scale weak (LSRW): For this group, L_{bj} and S_{bj} were longer than those for LD, and R_{std} was slightly lower than that in LD.

3. Local-scale weak and regional-scale strong (LWRS): As the values suggest, both R_{bj} and R_{std} were lower than those in LD and LSRW, especially R_{bj}. This suggests the winds veered less frequently and the differences of R found in 12 stations were smaller than in the two situations above. This situation shows that the influence of the regional-scale motion was greater than that for the previous two categories.

4. Regional-scale dominance (RD): In this category, wind direction at the study site was nearly uniform (extremely low R_{bj}) suggesting good ventilation (Allwine and Whiteman, 1994). The differences among R found at the 12 stations were even smaller than for the LWRS group, implying a strong increased influence of regional-scale motions. Indeed, the influence of regional-scale motions far outweighed the local ones for this category, and therefore, this group was considered to be dominated by strong regional-scale motions.

As shown in Table 1, the SOM classified 40% of cases were classified as LD, 29% were classified into RD, 17% and 14% were assigned into LSRW and LWRS respectively. These results indicate that most winter days in Baoji were strongly influenced by local-scale motions. Under LD, the average mass concentration of eBC$_{fossil}$ (3.08 ± 2.07 μg m^{-3}) and eBC$_{biomass}$ (1.52 ± 1.19 μg m^{-3}) were the highest among all four atmospheric categories noted above and over half (60% for eBC$_{biomass}$ and 55% for eBC$_{fossil}$) of the high values (75th to 100th percentile) were found in this category (Figure 3). In addition, as shown in Figure 3, the vast majority of the high values are located in the zone indicating air stagnation ($S_{bj} \leq$ 130km, shaded yellow). One difference that the 75th to 100th percentile eBC$_{biomass}$ tended to cluster at $R_{bj} \leq 0.2$ indicates that under LD circumstances, pollutants were likely coming from the same directions as where the main pollution sources were agglomerated, but eBC$_{fossil}$ in contrast, evidently originated from more scattered locations ($R_{bj} \geq 0.4$). Under LSRW, the averaged mass concentrations of eBC$_{fossil}$ and eBC$_{biomass}$ were 2.79 ± 1.73 μg m^{-3}and 1.06 ± 0.83 μg m^{-3} respectively (Table 1), which were both lower than those for the LD situation. When the regional scale of motion became stronger (i.e., LWRS and RD), the average mass concentration of eBC$_{fossil}$ (2.15 ± 1.62 μg m^{-3} and 1.69 ± 1.36 μg m^{-3}) and eBC$_{biomass}$ (0.86 ± 1.58 μg m^{-3} and 0.93 ± 0.72 μg m^{-3}) were lower, presumably because strong winds cause the pollutants to mix with cleaner air. Interestingly, 19% of the total 75th to 100th percentile eBC$_{biomass}$ was found under RD, and 55% of that was when ventilation was good ($S_{bj} \geq$ 250km, $R_{bj} \leq 0.2$, Figure 3, shaded grey). These findings imply that the high mass concentrations of eBC$_{biomass}$ were carried by regional-scale airflow to the site.

Figure 4 portrays the mass concentrations of eBC$_{fossil}$ and eBC$_{biomass}$ during the daytime and night time respectively under the four atmospheric motion categories specified earlier. As shown in Figure 4 (a) and (c), the mean values of both types of source-specific eBCs during daytime were the highest (3.02 ± 2.12 μg m^{-3} and 1.15 ± 0.8 μg m^{-3}) under LD and the lowest (1.36 ± 1.00 μg m^{-3} and 0.58 ± 0.53 μg m^{-3}) under RD. Meanwhile, the average mass concentrations of both types of eBC decreased when the influences of the regional scale of atmospheric motion getting were stronger. This suggests that eBC pollution was apt to accumulated under the dominance of local-scale motions and dispersed under the dominance of regional-scale motions during the daytime. Similar to the variations in the daytime, the mean values of eBC$_{fossil}$ (3.00 ± 2.04 μg m^{-3}) and eBC$_{biomass}$ (1.76 ± 1.33 μg m^{-3}) under LD were also the highest during the night. However, unlike eBC$_{fossil}$, the mass concentrations of eBC$_{biomass}$ did not decrease when the influence of regional-scale atmospheric motions was stronger (Figure S12). The mean

删除了: average L_{bj} = 106.9 km, S_{bj} = 164.8 km, R_{bj}=0.33, R_{std} = 0.23.

删除了: In these circumstances… L_{bj} and S_{bj} were longer than those forunder…LD, and. ...

删除了: average L_{bj} =159 km, S_{bj} = 183.4 km, R_{bj}=0.13, R_{std} = 0.20.

删除了: particularly the

删除了: for

设置了格式: 非突出显示

删除了: compared with that in the

删除了: average L_{bj} =235.6km, S_{bj} = 246.4 km, R_{bj}= 0.05, R_{std} = 0.18.

删除了: of…*R* found at thein…12 stations were even smaller than for the LWRS group, implying a strongfurther…increased influence of regional-scale motions. Indeed, tT…e influence of regional-scale motions far outweighs …utweighed the local ones forin…this category, and t. T…erefore, this groupone ...

删除了: Presented…in Table 1, t…he SOM classifiedhe SOM result showed that…40% of cases were classified LD, 29% were classified into RD, 17% and 14% were assigned into LSRW and LWRS respectively, … These results indicate that suggesting …ost winter days in Baoji were strongly greatly…influenced by local-scale motions in Baoji… ...

删除了: under

删除了:

删除了: The

删除了: Oneis

删除了:

删除了: , which

删除了: pollution was

删除了: .

删除了: By contrast, …BC$_{fossil}$ … in contrast, evidently originated may come ...

删除了: under

删除了: encourages

删除了: r

删除了: it under…good ventilation ...

删除了: , which…implyies ...

删除了: was

删除了: featured…atmospheric motion categories specified earlier. As shown in Figure 4 (a) and (c), the mean values of both types of source-specific eBCs during daytime were t ...

删除了: higher

删除了: enhanced

设置了格式: 非突出显示

value of eBC$_{biomass}$ under RD was the second highest (1.17 ± 0.73 μg m^{-3}). The nocturnal PBHL which was higher than 100m (Figure S13) for the RD group, and therefore, the high nocturnal eBC$_{biomass}$ may have been caused by the eBC$_{biomass}$ transported to the site from upwind regions.

3.3 Impacts of air mass directions

Atmospheric motions can not only cause the dispersal of pollution but also bring polluted air to the site from distant sources. Indeed, air mass movements can mean the difference between no pollution and severe pollution at a receptor site. To examine the impacts caused by air masses from different directions, the hourly 24h-back trajectories were calculated at 100 m above the ground using the Hybrid Single-Particle Lagrangian Integrated Trajectory model (Draxler and Hess, 1998, Text S2). Then the trajectories were clustered by using an angle-based distance statistics method (Text S2) to show the general directional features. This method determines the direction from which the air masses reach the site and has been widely used for air mass trajectory clusters. A detailed method description can be found in Sirois and Bottenheim (1995). Three air-mass trajectory clusters were identified (Figure S14), 45% of total trajectories associated with Cluster No.1, which originated from the north. Cluster No.2 accounted for 36% of the trajectories, and those were from the east direction while Cluster No.3 composed 19% of the total trajectories and displayed origins from southwest.

Hourly trajectories were assigned into the four featured atmospheric motions. The varying concentrations of the source-specific eBCs associated with different clusters indicate the divergent impacts of air mass direction on the pollution level at the sampling site. As shown in Table 1, LD was mainly connected with the air masses from Cluster No.2 (52%) and Cluster No.1 (45%). The average mass concentrations of eBC$_{fossil}$ and eBC$_{biomass}$ associated with Cluster No.1 were 2.82 ± 1.59 μg m^{-3} and 1.34 ± 1.07 μg m^{-3}. In comparison, Cluster No.2 was associated with a higher mean eBC$_{fossil}$ (3.2 ± 1.73 μg m^{-3}) and the highest mean eBC$_{biomass}$ (1.72 ± 1.29 μg m^{-3}) of the three clusters. This could be attributed to more intensive emissions in the eastern parts of Baoji because 75% of the total population of Baoji is located in this area (http://tjj.baoji.gov.cn/art/2020/10/15/art_9233_1216737.html, accessed on 25 September 2021, in Chinese). Several highways and railways are located in the south and southwest of Baoji, but the population is sparse with only ~4% of the total population residing in those areas. Thus, Cluster No.3 was associated with the highest mean eBC$_{fossil}$ concentration (3.64 ± 0.67 μg m^{-3}) but the lowest mean eBC$_{biomass}$ (0.67 ± 0.87 μg m^{-3}). It is important to point out, however, that only 3% of the total trajectories came from this cluster.

Under LSRW, 56% of the trajectories were from Cluster No.1, 33% from Cluster No.2, and 11% from Cluster No.3. Although the total averaged mass concentrations (Table 1) of two types of eBC generally showed that the regional-scale motions favored dissipation of eBC compared with LD, the eBC$_{fossil}$ (3.43 ± 1.17 μg m^{-3}) associated with Cluster No.2 and eBC$_{biomass}$ associated with Cluster No.3. (1 ± 0.64 μg m^{-3}) were higher by 0.23 μg m^{-3} and 0.33μg m^{-3} respectively relative to the LD case. The rise of eBC$_{fossil}$ associated with Cluster No.2 was possibly caused by the enhanced regional influence of pollutants brought from adjacent regions. According to previous studies (Wang et al., 2016; Xu et al., 2016), severe BC pollution in winter is caused by fossil fuel combustion in Xi'an which is to the east of Baoji. Studies also have reported that high EC emitted from biomass burning was found to have originated from Sichuan Province (Wu et al., 2020; Cai et al., 2018; Huang et al., 2020) which is to the southwest of Baoji. Combined with the phenomenon that the mass concentration of eBC$_{biomass}$ associated with Cluster No.3

删除了: Given…Tt ...

删除了: S9

删除了: under…RD group, and therefore, the high nocturnal high of …BC$_{biomass}$ may have beencould be ...

删除了: transported

设置了格式: 非突出显示

删除了: to the site

删除了: influences …he dispersalion…of pollution at a site…but also bringcan transport…polluted air mass…to the site from distant sourcesfar away… Indeed, aA…r mass movements can from different directions could ...

删除了: the…ngle-based distance statistics method angle distance method ...

删除了: 1

删除了: and… …a ...

删除了: Wang et al. (2018)

删除了: Finally, …t ...

删除了: S10

删除了: with …5% of total trajectories associated with Cluster No.1, which originated from the north. Cluster No.2 accounted for 36% of the trajectories, and those were classified as Cluster No.2 …rom the east direction while Cluster No.3 composed consisted of …9% of the total trajectories and displayed an …rigins from southwestly direction… ...

删除了: presented …n Table 1, LD was mainly connected with the air masses from Cluster No.2 (52%) and Cluster No.1 (45%). The average mass concentrations of eBC$_{fossil}$ and eBC$_{biomass}$ associated with Cluster No.1 were 2.82 ± 1.59 μg m^{-3} and 1.34 ± 1.07 μg m^{-3}. In comparison, Cluster No.2 was associated with a higher mean eBC$_{fossil}$ (3.2 ± 1.73 μg m^{-3}) and the highest mean eBC$_{biomass}$ (1.72 ± 1.29 μg m^{-3}) of among … ...

删除了: at …n the eastern parts of Baoji because the majority of the population of Baoji (~…5%)…of the total population of Baoji)…is distributed ...

删除了: th/9/…2021, in Chinese). Several highways and railways are located in the south and southwest of Baoji, but the although …opulation is sparse with only ~4% of the total population of Baoji …esiding in thoseis…areas. Thus, No.3 was associated with the highest mean eBC$_{fossil}$ concentration (3.64 ± 0.67 μg m^{-3}) but the lowest mean eBC$_{biomass}$ (0.67 ± 0.87 μg m^{-3}). Nonetheless, …i… is important to point out, however,worth noticing ...

域代码已更改

删除了: generally…the regional-scale motions favoreds…dissipation of eBC compared with those under…LD, the eBC$_{fossil}$ (3.43 ± 1.17 μg m^{-3}) associated with Cluster No.2 and eBC$_{biomass}$ associated with Cluster No.3. (1 ± 0.64 μg m^{-3}) were higher rose …y 0.23 μg m^{-3} and 0.33μg m^{-3} respectively relative to the LD case. The rise of eBC$_{fossil}$ associated with Cluster No.2 was possibly plausibly …au ...

rose with regional scales of motion, it is reasonable to conclude that the increase of eBC$_{\mathrm{biomass}}$ associated with Cluster No.3 was likely influenced by pollution transport from the southwest.

Under LWRS, 42% of the trajectories were from Cluster No.1., 36% from Cluster No.3, and 22% from Cluster No.2. With stronger regional scales of motion, the mean values of eBC$_{\mathrm{fossil}}$ and eBC$_{\mathrm{biomass}}$ associated with all clusters were lower than those under LD, except for eBC$_{\mathrm{biomass}}$ associated with Cluster 3 which increased by 0.52 µg m^{-3}. As mentioned before, this increase could have been caused by regional transport.

In the last category (RD), 41% of the trajectories were from Cluster No.1., 39% from Cluster No.3, and 20% from Cluster No.2. Similar to the results for LWRS, the average mass concentration of eBC$_{\mathrm{fossil}}$ and eBC$_{\mathrm{biomass}}$ associated with Cluster No.1 were only 35% and 48% of the respective values for LD. The average mass concentrations of eBC$_{\mathrm{fossil}}$ and eBC$_{\mathrm{biomass}}$ associated with Cluster No.2 were 32% and 51% of the eBC$_{\mathrm{fossil}}$ and eBC$_{\mathrm{biomass}}$ under LD. As for Cluster No.3, the average mass concentration of eBC$_{\mathrm{fossil}}$ associated with this cluster was also the lowest of all clusters. However, interestingly, the mean value of eBC$_{\mathrm{biomass}}$ associated with Cluster No.3 was highest compared with other categories of Cluster No.3. Under strong influences of a regional scale of motions, the value of eBC$_{\mathrm{biomass}}$ was 1.9 times as high as that under LD.

3.4 Radiative effects

Figure 5a shows the DREs at top of the atmosphere (DRE$_{\mathrm{eBC,\ TOA}}$), surface (DRE$_{\mathrm{eBC,\ SUF}}$), and the whole atmosphere (DRE$_{\mathrm{eBC,\ ATM}}$) of eBC$_{\mathrm{fossil}}$ and eBC$_{\mathrm{biomass}}$. The DRE$_{\mathrm{eBC,\ TOA}}$ and DRE$_{\mathrm{eBC,\ SUF}}$ of eBC were 13 W m^{-2} and -22.9 W m^{-2}, which were lower than that reported in Lanzhou (21.8 W m^{-2} and -47.5 W m^{-2} for DRE$_{\mathrm{eBC,\ TOA}}$ and DRE$_{\mathrm{eBC,\ SUF}}$) – which is another a river valley city in China (Zhao et al., 2019). This could be due to fact that the eBC mass concentration in Baoji was lower than in Lanzhou (Table S5). As for the DRE$_{\mathrm{eBC,\ TOA}}$ and DRE$_{\mathrm{eBC,\ SUF}}$ per an unit mass of BC, the results of the two studies were comparable. The DRE$_{\mathrm{eBC,\ TOA}}$ of eBC$_{\mathrm{fossil}}$ (DRE$_{\mathrm{eBCfossil,\ TOA}}$) and eBC$_{\mathrm{biomass}}$ (DRE$_{\mathrm{eBCbiomass,\ TOA}}$) were 9.4 ± 7.5 W m^{-2} and 3.6 ± 3.4 W m^{-2} indicating a warming effect at the top of the atmosphere. The DRE$_{\mathrm{eBC,\ SUF}}$ of eBC$_{\mathrm{fossil}}$ (DRE$_{\mathrm{eBCfossil,\ SUF}}$) and eBC$_{\mathrm{biomass}}$ (DRE$_{\mathrm{eBCbiomass,\ SUF}}$) were -16.5 ± 13.5 W m^{-2} and -6.4 ± 6.2 W m^{-2} showing a cooling effect at the surface. The DRE$_{\mathrm{eBC,\ ATM}}$ of eBC$_{\mathrm{fossil}}$ (DRE$_{\mathrm{eBCfossil,\ ATM}}$) and eBC$_{\mathrm{biomass}}$ (DRE$_{\mathrm{eBCbiomass,\ ATM}}$) were 25.9 ± 20.8 W m^{-2} and 10 ± 9.5 W m^{-2} in the atmosphere, indicating a heating effect.

Figure 5 also shows the DRE$_{\mathrm{eBC,\ ATM}}$ of the source-specific eBC for different atmospheric motions. In general, the changes of DRE$_{\mathrm{eBC,\ ATM}}$ are in accordance with those of the eBC mass concentrations. The DRE$_{\mathrm{eBCfossil,\ ATM}}$ under LD was the largest with a mean value of 30.4 ± 23 W m^{-2}, followed by LSRW (28.7 ± 20.7 W m^{-2}). As the mass concentration of eBC$_{\mathrm{fossil}}$ was low when regional scales of motion were stronger, the DRE$_{\mathrm{eBC,\ ATM}}$ under LWRS and RD also were lower compared with those under LD or LSRW. By contrast, the DRE$_{\mathrm{eBC,\ ATM}}$ of eBC$_{\mathrm{biomass}}$ under LSRW was the highest (11.5 ± 11.8 W m^{-2}), but it is only 0.3 W m^{-2} higher than that under LD. When the regional scale of motions became stronger, the DRE$_{\mathrm{eBCbiomass,\ ATM}}$ declined as expected due to the lower eBC$_{\mathrm{biomass}}$ mass concentrations (Figure 4c). The DRE$_{\mathrm{eBC,\ ATM}}$ of eBC$_{\mathrm{biomass}}$ under LWRS and RD were 8.6 ± 8.5 W m^{-2} and 7.9 ± 7.4 W m^{-2} respectively.

Although DRE$_{\mathrm{eBC,\ ATM}}$ declined with increased influences from the regional scale of motion, the DRE$_{\mathrm{eBC,\ ATM}}$ efficiency (DRE$_{\mathrm{eBC,\ ATM}}$ per mass concentration) was found to increase with greater regional-scale motion. Furthermore, the DRE efficiencies of both types of eBC under LD and LSRW were comparable, around 10 W m^{-2} (Table 2). In contrast, the efficiencies

删除了: the enhancement of a …egional scales of motion, it is reasonable to conclude believe…that the increase rise …f eBC$_{\mathrm{biomass}}$ associated with Cluster No.3 was likely influenced by pollution transport from the region to the ...

删除了: a…stronger regional scales of motion, the mean values of eBC$_{\mathrm{fossil}}$ and eBC$_{\mathrm{biomass}}$ associated with all clusters were lower than those under LD, except for the …BC$_{\mathrm{biomass}}$ associated with Cluster 3 which was further …ncreased by 0.52 µg m^{-3}. As mentioned before, this increase rise …ould have been be ...

删除了: ame as…LWRS, the average mass concentration of eBC$_{\mathrm{fossil}}$ and eBC$_{\mathrm{biomass}}$ associated with Cluster No.1 werewas…only 35% and 48% of the respective values forunder…LD respectively… The average mass of eBC$_{\mathrm{fossil}}$ and eBC$_{\mathrm{biomass}}$ associated with Cluster No.2 were was …2% and 51% of the eBC$_{\mathrm{fossil}}$ and eBC$_{\mathrm{biomass}}$ under LD. As for Cluster No.3, the average mass concentration of eBC$_{\mathrm{fossil}}$ associated with this cluster Cluster No.3 …as also the lowest of among …ll …lusterscircumstances… However, interestingly, the mean value of eBC$_{\mathrm{biomass}}$ associated with Cluster No.3 was highest compared with other categories of the concentration associated with…Cluster No.3 under other categories… Under a …tronger ...

删除了: was

删除了: was

删除了: -

删除了: which is also

删除了: cloud

删除了: because

删除了: is…as lower than that ...

删除了: For a unit of BC …he DRE$_{\mathrm{eBC,\ TOA}}$ and DRE$_{\mathrm{eBC,\ SUF}}$ per an unit mass of BC, in ...

删除了: those…two studies were comparable. The DRE$_{\mathrm{eBC,\ TOA}}$ of eBC$_{\mathrm{fossil}}$ (DRE$_{\mathrm{eBCfossil,\ TOA}}$) and eBC$_{\mathrm{biomass}}$ (DRE$_{\mathrm{eBCbiomass,\ TOA}}$) were 9.4 ± 7.5 W m^{-2} and 3.6 ± 3.4 W m^{-2} indicating a warming effect at the top of the atmosphere. The DRE$_{\mathrm{eBCfossil,\ SUF}}$ (…RE$_{\mathrm{eBC,\ SUF}}$ of eBC$_{\mathrm{fossil}}$)…(DRE$_{\mathrm{eBCfossil,\ SUF}}$) and DRE$_{\mathrm{eBCbiomass,\ SUF}}$ (DRE$_{\mathrm{eBC,\ SUF}}$ of …BC$_{\mathrm{biomass}}$) ...

设置了格式: 非突出显示

删除了: under …ifferent featured …tmosphericre…motions. In general, the changes of DRE$_{\mathrm{eBC,\ ATM}}$ are in accordance with those of the eBC mass concentrations of eBC… The DRE$_{\mathrm{eBCfossil,\ ATM}}$ under LD was the largest with a mean value of 30.4 ± 23 W m^{-2}, followed by DRE$_{\mathrm{eBCfossil,\ ATM}}$ under…LSRW (28.7 ± 20.7 W m^{-2}). As the mass concentration of eBC$_{\mathrm{fossil}}$ was low when ered…by a stronger …egional scales of motion were stronger, the DRE$_{\mathrm{eBC,\ ATM}}$ under LWRS and RD were …lso were lower compared with those under in …D and …r LSRW. By contrast, the DRE$_{\mathrm{eBC,\ ATM}}$ of eBC$_{\mathrm{biomass}}$ under LSRW was the highest (11.5 ± 11.8 W m^{-2}), but though…it is only 0.3 W ...

设置了格式: 下标

删除了: the enhancement of …egional-scale motion. Furthermore, tT…e calculation showed that …RE ...

varied more when the regional-scale motions were stronger. Under LWRS, the efficiencies of eBC$_{\text{fossil}}$ and eBC$_{\text{biomass}}$ were 13.5 ± 6.7 and 14.7 ± 8.1 (W m^{-2})/(μg m^{-3}) respectively. Under RD, the efficiencies were even higher, 15.6 ± 8.9 (W m^{-2})/(μg m^{-3}) for eBC$_{\text{fossil}}$ and 15.5 ± 8.4 (W m^{-2})/(μg m^{-3}) for eBC$_{\text{biomass}}$, which are > 1.5 times those recorded under LD. The higher eBC efficiencies may have been caused by the increases in the BC MAC during the regional transport. Studies have confirmed that the aging processes in the atmosphere can enhance the light-absorbing ability of BC (Chen et al., 2017; Shen et al., 2014), and regional transport can provide sufficient time for BC aging (Shiraiwa, et al. 2007; Cho et al., 2021). Therefore, the nonlinear change between mass concentration and DRE efficiency was very likely caused by the strong regional-scale motions that dispersed fresh BC from local emissions but also brought aged BC to the area from the upwind regions. As a result, under these conditions, the transported BC reached a receptor site with a higher light-absorbing ability which led to a higher DRE efficiency of BC at the sampling site. This strongly implies regionally transported BC can greatly perturb climate, particularly at the river-valley city in our study where dispersion was weak (Zhao et al., 2015; Wang et al., 2013).

4 Conclusions

This study derived site-specific AAEs using a PMF model for which chemical and optical data collected from a river-valley city during winter were used as the inputs. Based on the calculated AAEs, source-specific eBCs (i.e., eBC$_{\text{fossil}}$ and eBC$_{\text{biomass}}$) were then apportioned using an aethalometer model. Finally, the impacts of different scales of atmospheric motions on the mass concentrations of the source-specific eBCs and the induced DREs were investigated. Four sources of eBC were identified: which are diesel vehicular emissions, biomass burning, coal combustion, and mineral dust. The derived AAEs were 1.07 for diesel vehicular emissions, 2.13 for biomass burning, 1.74 for coal combustion, and 1.78 for mineral dust. The mean values of eBC$_{\text{fossil}}$ and eBC$_{\text{biomass}}$ were 2.46 μg m^{-3} and 1.17 μg m^{-3}, respectively.

The self-organizing map indicated that there were four types of atmospheric motions during the sampling period that affected the mass concentrations of source-specific eBCs. Of these, the local-scale motions were the main influence on most winter days. The eBC$_{\text{fossil}}$ and eBC$_{\text{biomass}}$ under those identified atmospheric motions showed that over half of the 75th to 100th percentile values for the entire data set were found in LD group (60% for eBC$_{\text{biomass}}$ and 55% for eBC$_{\text{fossil}}$). This illustrates that the BC pollution was more severe under the influences of local-scale motion outweighed regional-scale motions. However, even though regional-scale motions were associated with lower eBCs, 19% of the high values of eBC$_{\text{biomass}}$ values occurred under RD, especially when there was good ventilation. Furthermore, the air masses from different directions also had impacts on the source-specific eBCs that varied relative to the different atmospheric motions. eBC$_{\text{fossil}}$ most likely accumulated under the influence of strong local-scale motions, but eBC$_{\text{biomass}}$ also was found to be increased with the enhanced regional scale of motions when the air masses from the southwest; this indicates that there were impacts from regional transport.

Similar to the mass concentrations, the DREs of the two types of eBC were both lower when the regional scale of motions were greater than the local ones. However, the changes in mass concentrations and DREs were not proportionate because the regional-scale of motions carried the fresh BC away from the local site but brought the aged BCs to the site from the upwind regions. As a result, the DRE efficiency of eBC was ~1.5 times higher when the regional scale of motion was stronger. This study showed that different scales of air motions affected the mass concentrations of source-specific eBCs and their DRE

删除了: so under a stronger influence of

删除了: (W m^{-2})/(μg m^{-3})…and 14.7 ± 8.1 (W m^{-2})/(μg m^{-3}) respectively. Under RD, the efficiencies were even higher, which were ...

删除了: 6.7

删除了: respectively… which are > over ….5 times those recorded under LD. The higher eBC efficienciesThis…may have been caused by could be attributed to…the increases in the BC the enhanced…MAC of BC…during the regional transport. Studies have confirmed that the aging processes in the atmosphere can would…enhance the light-absorbing ability of BC (Chen et al., 2017; Shen et al., 2014), and regional transport can provide sufficient time for BC aging (Shiraiwa, et al. 2007; Cho et al., 2021). Therefore, the nonlinear disproportional…change between mass and DRE efficiency was very likely caused by the strong regional-scale motions that dispersed blew away the …resh BC from local emissions but also in the meantime …roug ...

设置了格式: 下标

设置了格式: 下标

删除了: when regional scale motion is strong… This strongly implies regionally transported BC can a …reatlyer…perturbation…to regional …limate caused by regionally transported BC… particularly in …t the river-city in our study where due to weak…dispersion was weakconditions…(Zhao et al., 2015; Wang et al., 2013). indicating a potentially enhanced climatic effect. ...

删除了: the… PMF model for whichwith…chemical and optical data collected from in … river-valley city during winter were used as the inputs. Based on the calculatedWith those…AAEs, source-specific eBCs (i.e., eBC$_{\text{fossil}}$ and eBC$_{\text{biomass}}$) were then apportioned using anthe…aethalometer model. Finally, the impacts of different scales offeatured…atmospheric motions on the mass concentrations of the source-specific eBCs and the induced DREs were ...

删除了: that is

删除了: During the sampling period,…the mass concentrations of source-specific eBCs were influenced b ...

删除了: featured

删除了: (60% for eBC$_{\text{biomass}}$ and 55% for eBC$_{\text{fossil}}$) …f …the high values (…5th to 100th percentile values for the entire ...

删除了: in general …as more severe under the likely to happen when the…influences offrom…local-scale motio ...

删除了: from

删除了: the …egional-scale motions. However, even though although …egional-scale motions were associated with ...

删除了: a…stronger …nfluence of strong local-scale motions, but by contrast besides accumulating under a st ...

删除了: regional transport.i

删除了: ndicating an evident

删除了: outweighed …he local ones. However, the changes of …n mass concentrations and DREs were not ...

efficiencies. More specifically our study highlights importance of regional transport for the BC radiative forcing and shows how the enhancement of BC radiative effects caused by aging during regional transport could have especially significant implications for sites in river valleys. The relationships between BC and atmospheric scales of motion should be evaluated for other environments besides river valley cities because quantitative information on the relative importance of locally emitted versus regionally transported materials will be useful for developing pollution controls and for predicting future changes in climate.

删除了: It

删除了: that the DRE efficiency of BC was

删除了: ed

删除了: which

删除了: lead to greater consequences in receptor regions and the potential enhanced climatic effect of regionally transported BC is worthy of attention in terms of regional climate stability.

Data availability. The data are available from the authors upon request.

Supplement. The supplement related to this article is available online.

Author contributions. QW and JC designed the study. BZ and SL conducted the field measurements. YQ and JT conducted data analysis. SL and TZ performed the chemical analysis of filters. HL draft the article and QW revised it. JC and YH commented on the paper.

Competing interests. The authors declare that they have no conflict of interest.

Acknowledgments. This research has been supported by the National Natural Science Foundation of China (42192512), the Key Research and Development Program of Shaanxi Province (2018-ZDXM3-01), the Key Project of CAS (ZDRW-ZS-2017-6), and the Youth Innovation Promotion Association of the Chinese Academy of Sciences (2019402).

删除了: This research has been supported by the Key Research and Development Program of Shaanxi Province (2018-ZDXM3-01), the Strategic Priority Research Program of Chinese Academy of Sciences (XDB40000000), Key Project of CAS (ZDRW-ZS-2017-6), and the Youth Innovation Promotion Association of the Chinese Academy of Sciences (2019402).

Reference

Amato, F., Alastuey, A., Karanasiou, A., Lucarelli, F., Nava, S., Calzolai, G., Severi, M., Becagli, S., Gianelle, V. L., Colombi, C., Alves, C., Custódio, D., Nunes, T., Cerqueira, M., Pio, C., Eleftheriadis, K., Diapouli, E., Reche, C., Minguillón, M. C., Manousakas, M.-I., Maggos, T., Vratolis, S., Harrison, R. M., and Querol, X.: AIRUSE-LIFE+: a harmonized PM speciation and source apportionment in five southern European cities, Atmos. Chem. Phys., 16, 3289–3309, https://doi.org/10.5194/acp-16-3289-2016, 2016.

Artaxo, P., Fernandas, E. T., Martins, J. V., Yamasoe, M. A., Maenhaut, W., Longo, K. M., Castanho, A., and Hobbs, P. V.: Large-scale aerosol source apportionment in Amazonia, J. Geophys. Res.-Atmos., 103, 31837–31847, https://doi.org/10.1029/98jd02346, 1998.

Allwine, K. J., and Whiteman, C. D.: Single-station integral measures of atmospheric stagnation, recirculation and ventilation. Atmos. Environ., 28: 713–721, https://doi.org/10.1016/1352-2310(94)90048-5, 1994.

Bei, N., Li, G., Huang, R., Cao, J., Meng, N., Feng, T., Liu, S., Zhang, T., Zhang, Q., and Molina, L.: Typical synoptic situations and their impacts on the wintertime air pollution in the Guanzhong basin, China, Atmos. Chem. Phys., 16, 7373–7387, http://dx.doi.org/10.5194/acp-16-7373-2016, 2016.

Bond, T. C., Doherty, S. J., Fahey, D. W., Forster, P. M., Berntsen, T., DeAngelo, B. J., Flanner, M. G., Ghan, S., Karcher, B., Koch, D., Kinne, S., Kondo, Y., Quinn, P. K., Sarofim, M. C., Schultz, M. G., Schulz, M., Venkataraman, C., Zhang, H., Zhang, S., Bellouin, N., Guttikunda, S. K., Hopke, P. K., Jacobson, M. Z., Kaiser, J. W., Klimont, Z., Lohmann, U., Schwarz, J. P., Shindell, D., Storelvmo, T., Warren, S. G., and Zender, C. S.: Bounding the role of black carbon in the climate system: A scientific assessment, J. Geophys. Res.-Atmos., 118, 5380–5552, https://doi.org/10.1002/jgrd.50171, 2013.

Brown, S. G., Eberly, S., Paatero, P., and Norris, G. A.: Methods for estimating uncertainty in PMF solutions: Examples with ambient air and water quality data and guidance on reporting PMF results, Sci. Total Environ., 518–519, 626–635, https://doi.org/10.1016/j.scitotenv.2015.01.022, 2015.

Brulfert, G., Chemel, C., Chaxel, E., Chollet, J., Jouve, B., and Villard, H.: Assessment of 2010 air quality in two Alpine valleys from modelling: Weather type and emission scenarios, Atmos. Environ., 40, 7893–7907, https://doi.org/10.1016/j.atmosenv.2006.07.021, 2006.

Cao, J. J., Zhu, C. S., Tie, X. X., Geng, F. H., Xu, H. M., Ho, S. S. H., Wang, G. H., Han, Y. M., and Ho, K. F.: Characteristics and sources of carbonaceous aerosols from Shanghai, China, Atmos. Chem. Phys., 13, 803-817, https://doi.org/10.5194/acp-13-803-2013, 2013.

Cai, S., Ma, Q., Wang, S., Zhao, B., Brauer, M., Cohen, A., Martin, R., Zhang, Q., Li, Q., Wang, Y., Hao, J., Frostad, J., Forouzanfar, M., and Burnett, R.: Impact of air pollution control policies on future PM$_{2.5}$ concentrations and their source contributions in China, J. Environ. Manage., 227, 124–133, https://doi.org/10.1016/j.jenvman.2018.08.052, 2018.

Cappa, C. D., Onasch, T. B., Massoli, P., Worsnop, D. R., Bates, T. S., Cross, E. S., Davidovits, P., Hakala, J., Hayden, K. L., Jobson, B. T., Kolesar, K. R., Lack, D. A., Lerner, B. M., Li, S.-M., Mellon, D., Nuaaman, I., Olfert, J. S., Petäjä, T., Quinn, P. K., Song, C., Subramanian, R., Williams, E. J., and Zaveri, R. A.: Radiative absorption enhancements due to the mixing state of atmospheric black carbon, Science., 337, 1078–1081, https://doi.org/10.1126/science.1223447, 2012.

Carvalho, A.C., Carvalho, A., Gelpi, I., Barreiro, M., Borrego, C., Miranda, A., and Perez-Munuzuri, V.: Influence of topography and land use on pollutants dispersion in the Atlantic coast of Iberian Peninsula, Atmos. Environ., 40,3969–3982, https://doi.org/10.1016/j.atmosenv.2006.02.014, 2006.

Cho, C., Schwarz, J., Perriing, A., Lamb, K., Kondo, Y., Park, J., Park, D., Shim, K., Park, J., Park, R., Lee, M., Song, C., Kim, S.: Light-absorption enhancement of black carbon in the Asian outflow inferred from airborne SP2 and in-situ measurements during KORUS- AQ, Sci. Total Environ., 773, 145531, https://doi.org/10.1016/j.scitotenv.2021.145531, 2021.

Chang, F., Chang, L., Kang, C., Wang, Y., Huang, A.: Explore spatio-temporal PM$_{2.5}$ features in northern Taiwan using machine learning techniques, Sci. Total Environ., 736, 139656, https://doi.org/10.1016/j.scitotenv.2020.139656, 2020.

Cheng, Y., He, K., Zheng, M., Duan, F., Ma, Y., Tan, J., Yang, F., Liu, J., Zhang, X., Weber, R., Bergin, M. and Russell, A.: Mass absorption efficiency of elemental carbon and water-soluble organic carbon in Beijing, China, Atmos. Chem. Phys., 11, 11497–11510, https://doi:10.5194/acp-11-11497-2011, 2011.

Chen, X., Wang, Z., Yu, F., Pan, X., Li, J., Ge, B., Wang, Z., Hu, M., Yang, W., Chen, H.: Estimation of atmospheric aging time of black carbon particles in the polluted atmosphere over central-eastern China using microphysical process analysis in regional chemical transport model, Atmos. Environ., 163,44-56, https://doi.org/10.1016/j.atmosenv.2017.05.016, 2017

Drinovec, L., Močnik, G., Zotter, P., Prévôt, A. S. H., Ruckstuhl, C., Coz, E., Rupakheti, M., Sciare, J., Müller, T., Wiedensohler, A., and Hansen, A. D. A.: The "dual-spot" Aethalometer: an improved measurement of aerosol black carbon with real-time loading compensation, Atmos. Meas. Tech., 8, 1965-1979, https://doi.org/10.5194/amt-8-1965-2015, 2015.

Draxler, R., and Hess, G.: An overview of the HYSPLIT_4 modelling system for trajectories, Aust. Meteorol. Mag., 47, 1998.

Dutton, J., The ceaseless wind an introduction to the theory of atmospheric motion, McGraw-Hill, Inc., U.S.A., 1976

Geivanidis, S., Pistikopoulos, P., and Samaras, Z.: Effect on exhaust emissions by the use of methylcyclopentadienyl manganese tricarbonyl (MMT) fuel additive and other lead replacement gasolines. Sci. Total Environ., *305*, 129-141, https://doi.org/10.1016/S0048-9697(02)00476-X, 2003.

Glojek, K., Moˇcnik, G., Alas, H., Cuesta-Mosquera, A., Drinovec, L., Gregoriˇc, A., Ogrin, M., Ježek, I., Müller, T., Rigler, M., Remškar, M., Pinxteren, D., Herrmann, H., Ristorini, M., Merkel, M., Markelj, M., Wiedensohler, A.: The impact of temperature inversions on black carbon and particle mass concentrations in a mountainous area, Atmos. Chem. Phys., 22, 5577–5601, https://doi.org/10.5194/acp-22-5577-2022, 2022.

Green, M., Chow, J., and Watson, G.: Effects of snow cover and atmospheric stability on winter PM$_{2.5}$ concentrations in western U.S. valleys, J. Appl. Meteorol. Clim., 54, https://doi.org/doi: 10.1175/JAMC-D-14-0191.1, 2016.

Han, H., Liu, J., Shu, L., Wang, T., and Yuan, H.: Local and synoptic meteorological influences on daily variability in summertime surface ozone in eastern China, Atmos. Chem. Phys., 20, 203–222, https://doi.org/10.5194/acp-20-203-2020, 2020.

Helin, A., Niemi, J. V., Virkkula, A., Pirjola, L., Teinilä, K., Backman, J., Aurela, M., Saarikoski, S., Rönkkö, T., Asmi, E., and Timonen, H.: Characteristics and source apportionment of black carbon in the Helsinki metropolitan area, Finland, Atmos. Environ., 190, 87-98, https://doi.org/10.1016/j.atmosenv.2018.07.022, 2018.

设置了格式：下标

删除了: Absorption

删除了: Enhancements

删除了: Due

删除了: Mixing

删除了: S

删除了: A

删除了: B

删除了: C

设置了格式：下标

删除了: C

删除了: W

删除了: I

删除了: T

删除了: T

删除了: A

删除了: M

删除了: S

删除了: C

删除了: A

删除了: S

删除了: W

删除了: C

删除了: W

设置了格式：下标

删除了: V

删除了: Journal of Applied Meteorology and Climatology

He, C., Liou, K.-N., Takano, Y., Zhang, R., Levy Zamora, M., Yang, P., Li, Q., and Leung, L. R.: Variation of the radiative properties during black carbon aging: theoretical and experimental intercomparison, Atmos. Chem. Phys., 15, 11967–11980, https://doi.org/10.5194/acp-15-11967-2015, 2015.

Hewitson, B. C. and Crane, R. G.: Consensus between GCM climate change projections with empirical downscaling: precipitation downscaling over South Africa, Int. J. Climatol., 26, 1315–1337, https://doi.org/10.1002/joc.1314, 2006.

Hsu, C.-Y., Chiang, H.-C., Lin, S.-L., Chen, M.-J., Lin, T.-Y., and Chen, Y.-C.: Elemental characterization and source apportionment of PM 10 and PM 2.5 in the western coastal area of central Taiwan, Sci. Total Environ., 541, 1139-1150, https://doi.org/10.1016/j.scitotenv.2015.09.122, 2016.

Huang, Y., Zhang, L., Li, T., Chen, Y., and Yang, F.: Seasonal variation of carbonaceous species of PM$_{2.5}$ in a small city in Sichuan Basin, China, Atmosphere., 11, 1286, https://doi.org/10.3390/atmos11121286, 2020.

Jacobson, M. Z.: Control of fossil-fuel particulate black carbon and organic matter, possibly the most effective method of slowing global warming, J. Geophys. Res., 107, 4410, https://doi.org/10.1029/2001JD001376, 2002.

Jiang, N. B., Scorgie, Y., Hart, M., Riley, M. L., Crawford, J., Beggs, P. J., Edwards, G. C., Chang, L. S., Salter, D., and Virgilio, G. D.: Visualising the relationships between synoptic circulation type and air quality in Sydney, a subtropical coastal-basin environment, Int. J. Climatol., 37, 1211–1228, https://doi.org/10.1002/joc.4770, 2017.

Kant, Y., Shaik,D., S., Mitra, D., Chandola, H., Babu, S. S., and Chauhan, P., Black carbon aerosol quantification over north-west himalayas: seasonal heterogeneity, source apportionment and radiative forcing, Environ. Pollut., 10.1016/j.envpol.2019.113446, 2019.

Kangas, J., and Kohonen, T.: Developments and applications of the self-organizing map and related algorithms, Math. Comput. Simulat., 41, 3-12, https://doi.org/10.1016/0378-4754(96)88223-1, 1996.

Kahnert, M., and Kanngiesser, F.: Review: modelling optical properties of atmospheric black carbon aerosols. J. Quant. Spectrosc., RA, 244, 106849, https://doi.org/10.1016/j.jqsrt.2020.106849, 2020.

Kalthoff, N., Horlacher, V., Corsmeier, U., Volz-Thomas, A., Kolahgar, B., Geiß, H., Möllmann-Coers, M., and Knaps, A.: Influence of valley winds on transport and dispersion of airborne pollutants in the Freiburg-Schauinsland area, J. Geophys. Res.-Atmos., 105, 1585–1597, https://doi.org/10.1029/1999jd900999, 2000.

Kirchstetter, T. W., Novakov, T., and Hobbs, P. V.: Evidence that the spectral dependence of light absorption by aerosols is affected by organic carbon, J. Geophys. Res.-Atmos., 109, D21208, https://doi.org/10.1029/2004jd004999, 2004.

Kohonen, T.: The self-organizing map, Proc. IEEE, 78, 1464–1480, https://doi.org/10.1109/5.58325, 1990.

Kohonen, T., and Simula, O., Visa, A., Kangas, J.: Engineering Applications of the Self-Organizing Map, P. IEEE, 84(10), 1358-1384, https://doi.org/10.1109/5.537105,1996.

Liao, Z., Xie, J., Fang, X., Wang, Y., Zhang, Y., Xu, X., and Fan, S.: Modulation of synoptic circulation to dry season PM$_{2.5}$ pollution over the Pearl River Delta region: An investigation based on self-organizing maps. Atmos. Environ., 230, 117482, https://doi.org/10.1016/j.atmosenv.2020.117482, 2020.

Liu, S., Gautam, A., Yang, X., Tao, J., Wang, X., Zhao, W: Analysis of improvement effect of PM$_{2.5}$ and gaseous pollutants in Beijing based on self-organizing map network, Sustain. Cities Soc., 70, 102827, https://doi.org/10.1016/j.scs.2021.102827, 2021.

Lewis, C. W., Norris, G. A., Conner, T. L., and Henry, R. C.: Source apportionment of Phoenix PM$_{2.5}$ aerosol with the Unmix receptor model, J. Air Waste Manage., 53, 325–338, https://doi.org/10.1080/10473289.2003.10466155, 2003.

Levy, I., Dayan, U., and Mahrer, Y.: Differing atmospheric scales of motion and their impact on air pollutants, Int. J. Climatol., 30, 612–619, https://doi.org/10.1002/joc.1905, 2010.

Lin, Y., Tsai, C., Wu, T., Zhang, R., Chi, K., Huang, Y., Lin, S., and Hsu, S.: Characteristics of trace metals in traffic-derived particles in Hsuehshan Tunnel, Taiwan: size distribution, potential source, and fingerprinting metal ratio, Atmos. Chem. Phys., 15, 4117–4130, https://doi.org/10.5194/acp-15-4117-2015, 2015.

IPCC: Climate Change 2021: The physical science basis. contribution of working group i to the sixth assessment report of the intergovernmental panel on climate change [Masson-Delmotte, V., P. Zhai, A. Pirani, S.L. Connors, C. Péan, S. Berger,

删除了: V
删除了: C
删除了: S
删除了: S
删除了: C
删除了: S
删除了: Environmental Pollution
设置了格式: 下标
设置了格式: 下标
删除了: Physical

N. Caud, Y. Chen, L. Goldfarb, M.I. Gomis, M. (eds)], https://reliefweb.int/report/world/climate-change-2021-physical-science-basis, 2021

Manousakas, M., Papaefthymiou, H., Diapouli E., Migliori, A., Karydas, A.G., Bogdanovic-Radovic, I., Eleftheriadis, K.: Assessment of $PM_{2.5}$ sources and their corresponding level of uncertainty in a coastal urban area using EPA PMF 5.0 enhanced diagnostics, Sci. Total Environ., 574, 155–164, https://doi.org/10.1016/j.scitotenv.2016.09.047, 2017.

Manö, S., and Andreae, M.O.: Emission of methyl bromide from biomass burning. Science., 263, 1255–1257, https://doi.org/10.1126/science.263.5151.1255, 1994.

Norris, G., Duvall, R., Brown, S. and Bai, S.: EPA Positive Matrix Factorization (PMF) 5.0 fundamentals and User Guide Prepared for the US Environmental Protection Agency Office of 30 Research and Development, Washington, DC, by the National Exposure Research Laboratory, Research Triangle Park; Sonoma Technology, Inc., Petaluma., https://www.epa.gov/air-research/epa-positive-matrix-factorization-50-fundamentals-and-user-guide, 2014.

Ochoa-Hueso, R., Munzi, S., Alonso, R., Arróniz-Crespo, M., Avila, A., Bermejo, V., Bobbink, R., Branquinho, C., Concostrina-Zubiri, L., Cruz, C., Cruz de Carvalho, R., De Marco, A., Dias, T., Elustondo, D., Elvira, S., Estébanez, B., Fusaro, L., Gerosa, G., Izquieta-Rojano ,S., Lo Cascio, M., Marzuoli, R., Matos, P., Mereu, S., Merino, J., Morillas, L., Nunes, A., Paoletti, E., Paoli, L., Pinho, P., Rogers, I.B., Santos, A., Sicard, P., Stevens, C. J., and Theobald, M. R.: Ecological impacts of atmospheric pollution and interactions with climate change in terrestrial ecosystems of the Mediterranean Basin: Current research and future directions, Environ. Pollut., 227, 194–206, 2017.

Oke, T., Boundary layer climates, 2nd edition, Taylor & Francis e-Library, 2002.

Panicker, A. S., Pandithurai, G., Safai, P. D., Dipu, S., and Lee, D.-I.: On the contribution of black carbon to the composite aerosol radiative forcing over an urban environment, Atmos. Environ., 44, 3066-3070, 10.1016/j.atmosenv.2010.04.047, 2010.

Pathak, B., Kalita, G., Bhuyan, K., Bhuyan, P. and Moorthy, K.: Aerosol temporal characteristics and its impact on shortwave radiative forcing at a location in the northeast of India, J. Geophys. Res.-Atmos., 115, D19204, https://doi:10.1029/2009JD013462, 2010.

Peng, J., Hu, M., Guo, S., Du, Z., Zheng, J., Shang, D., Levy, M., and Zeng, L.: Markedly enhanced absorption and direct radiative forcing of black carbon under polluted urban environments, P. Natl. Acad. Sci. USA, 113, 4266–4271, https://doi.org/10.1073/pnas.1602310113, 2016.

Pearce, J. L., Waller, L. A., Chang, H. H., Klein, M., Mulholland, J. A., Sarnat, J. A., Sarnat, S. E., Strickland, M. J., and Tolbert, P. E.: Using self-organizing maps to develop ambient air quality classifications: a time series example, Environ. Health-Glob., 13, https://doi.org/10.1186/1476-069X-13-56, 2014.

Ramachandran A., Rustum, R., and Adeloye, A.: Anaerobic digestion process modeling using Kohonen self-organising maps, Heliyon, 5,e01511, https://doi.org/10.1016/j.heliyon.2019.e01511, 2019.

Rajesh, T. A., and Ramachandran, S.: Black carbon aerosols over urban and high altitude remote regions: characteristics and radiative implications, Atmos. Environ., 194, 110-122, https://doi.org/10.1016/j.atmosenv.2018.09.023, 2018.

Reusch, D.B., Alley, R.B., and Hewitson, B.C.: Relative performance of Self-Organizing Maps and principal component analysis in pattern extraction from synthetic climatological data. Polar Geogr., 29(3): 188–212. http://dx.doi.org/10.1080/789610199, 2005.

Ricchiazzi, P., Yang, S., Gautier, C., and Sowle, D.: SBDART: A research and teaching software tool for plane-parallel radiative transfer in the Earth’s atmosphere, B. Am. Meteorol. Soc., 79, 2101–2114, https://doi.org/10.1175/1520-0477(1998)0792.0.CO;2, 1998.

Sandradewi, J., Prévôt, A. S. H., Weingartner, E., Schmidhauser, R., Gysel, M., and Baltensperger, U.: A study of wood burning and traffic aerosols in an Alpine valley using a multi-wavelength Aethalometer, Atmos. Environ., 42, 101-112, https://doi.org/10.1016/j.atmosenv.2007.09.034, 2008.

Seinfeld, J., and Pandis, S., 2006. Atmospheric chemistry and physics: from air pollution to climate change, 2nd ed., Published by John Wiley & Sons, Inc., Hoboken, New Jersey, United States of America,

设置了格式：下标

删除了: Layer

删除了: Climates

删除了: Characteristics

Schroter, D., Cramer, W., Leemans, R., Prentice, C., Araujo, M., Arnell, N., Bondeau, A., Bugmann, H., Carter, T., Gracia, C., de la Vega-Leinert, A., Erhard, M., Ewert, F., Glendining, M., House, J., Kankaanpaa, S., Klein, R., Lavorel, S., Lindner, M., Metzger, M., Meyer, J., Mitchell, T., Reginster, I., Rounsevell, M., Sabate, S., Sitch, S., Smith, B., Smith, J., Smith, P., Sykes, ´ M., Thonicke, K., Thuiller, W., Tuck, G., Zaehle, S., and Zierl, B.: Ecosystem service supply and vulnerability to Global Change in Europe, Science., 310, 1333–1337, https://doi.org/10.1126/science.1115233, 2005.

Shen, Z., Liu, J., Horowitz, W., Henze, D., Levy, H., Mauzerall, D., Lin, J., and Tao, S.: Analysis of transpacific transport of black carbon during HIPPO-3: implications for black carbon aging, Atmos. Chem. Phys., 14, 6315–6327, https://doi.org/10.5194/acp-14-6315-2014, 2014.

Shiraiwa, M., Kondo, Y., Moteki, N., Takegawa, N., Miyazaki, Y., and Blake, D. R.: Evolution of mixing state of black carbon in polluted air from Tokyo, Geophys. Res. Letters., 34, L16803, https://doi.org/10.1029/2007GL029819, 2007.

Shindell, D., Kuylenstierna, J. C. I., Vignati, E., van Dingenen, R., Amann, M., Klimont, Z., Anenberg, S. C., Muller, N., JanssensMaenhout, G., Raes, F., Schwartz, J., Faluvegi, G., Pozzoli, L., Kupiainen, K., Hoglund-Isaksson, L., Emberson, L., Streets, D., Ramanathan, V., Hicks, K., Oanh, N. T. K., Milly, G., Williams, M., Demkine, V., and Fowler, D.: Simultaneously mitigating near-term climate change and improving human health and food security, Science, 335, 183–189, https://doi.org/10.1126/science.1210026, 2012.

Sirois, A. and Bottenheim, J. W.: Use of backward trajectories to interpret the 5-year record of PAN and O_3 ambient air concentrations at Kejimkujik National Park, Nova Scotia, J. Geophys. Res., 100, 2867–2881, https://doi.org/10.1029/94JD02951, 1995.

设置了格式：下标

Song, Y., Zhang, Y., Xie, S., Zeng, L., Zheng, M., Salmon, L. G., Shao, M., and Slanina, S.: Source apportionment of $PM_{2.5}$ in Beijing by positive matrix factorization, Atmos. Environ., 40, 1526-1537, https://doi.org/10.1016/j.atmosenv.2005.10.039, 2006.

设置了格式：下标

Sun, J., Zhi, G., Hitzenberger, R., Chen, Y., Tian, C., Zhang, Y., Feng, Y., Cheng, M., Zhang, Y., Cai, J., Chen, F., Qiu, Y., Jiang, Z., Li, J., Zhang, G., and Mo, Y.: Emission factors and light absorption properties of brown carbon from household coal combustion in China, Atmos. Chem. Phys., 17, 4769–4780, https://doi.org/10.5194/acp-17-4769-2017, 2017.

Stauffer, R. M., Thompson, A. M., and Young, G. S.: Tropospheric ozonesonde profiles at long-term US monitoring sites: 1. A climatology based on self-organizing maps, J. Geophys. Res.-Atmos, 121, 1320–1339, https://doi.org/10.1002/2015JD023641, 2016.

Tan, J., Zhang, L. Zhou, X., Duan, J. Li, Y., Hu, J., and He, K.: Chemical characteristics and source apportionment of $PM_{2.5}$ in Lanzhou, China, Sci. Total Environ., 601, 1743-1752, https://doi.org/10.1016/j.scitotenv.2017.06.050, 2017.

设置了格式：下标

Tao, J., Zhang L., Zhang, R., Wu, Y., Zhang, Z., Zhang, X., Tang. Y., Cao, J., and Zhang, Y.: Uncertainty assessment of source attribution of PM2.5 and its water-soluble organic carbon content using different biomass burning tracers in positive matrix factorization analysis — a case study in Beijing, China, Sci. Total Environ., 543, 326–335, https://doi.org/10.1016/j.scitotenv.2015.11.057, 2016.

Tao, J., Zhang, L. M., Cao, J. J., Zhong, L. J., Chen, D. S., Yang, Y. H., Chen, D. H., Chen, L. G., Zhang, Z. S., Wu, Y. F., Xia, Y. J., Ye, S. Q., and Zhang, R. J.: Source apportionment of $PM_{2.5}$ at urban and suburban areas of the Pearl River Delta region, south China – with emphasis on ship emissions, Sci. Total Environ., 574, 1559–1570, https://doi.org/10.1016/j.scitotenv.2016.08.175, 2017.

设置了格式：下标

Thorpe, A., and Harrison, R. M.: Sources and properties of non-exhaust particulate matter from road traffic: A review, Sci. Total Environ., *400*, 270-282, https://doi.org/10.1016/j.scitotenv.2008.06.007, 2008.

Urban, R. C., Lima-Souza, M., Caetano-Silva, L., Queiroz, M. E. C., Nogueira, R. F. P., Allen, A. G., Cardoso, A. A., Held, G., and Campos, M. L. A. M.: Use of levoglucosan, potassium, and water-soluble organic carbon to characterize the origins of biomass-burning aerosols, Atmos. Environ., 61, 562-569, https://doi.org/10.1016/j.atmosenv.2012.07.082, 2012.

Washenfelder, R., Attwood, A., Brock, C., Guo, H., Xu, L., Weber, R., Ng, N., Allen, H., Ayres, B., Baumann, K., Cohen, R., Draper, D., Duffey, K., Edgerton, E., Fry, J., Hu, W., Jimenez, J., Palm, B., Romer, P., Stone, E., Wooldridge, P., and Brown, S.: Biomass burning dominates brown carbon absorption in the rural southeastern United States, Geophys. Res. Lett., 42, 653–664, https://doi.org/10.1002/2014GL062444, 2015

Wang, Q., Huang, R., Zhao, Z., Cao, J., Ni, H., Tie, X., Zhao, S., Su, X., Han, Y., Shen, Z., Wang, Y., Zhang, N., Zhou, Y., and Corbin, J.: Physicochemical characteristics of black carbon aerosol and its radiative impact in a polluted urban area of China, J. Geophys. Res. Atmos., 121, https://doi.org/doi:10.1002/2016JD024748, 2016.

Wang, Q., Han, Y., Ye, J., Liu, S., Pongpiachan, S., Zhang, N., Han, Y., Tian, J., Wu, C., Long, X., Zhang, Q., Zhang, W., Zhao, Z., and Cao, J.: High contribution of secondary brown carbon to aerosol light absorption in the southeastern margin of Tibetan Plateau, Geophys. Res. Lett., 46, 4962–4970, https://doi.org/10.1029/2019GL082731, 2019.

Wang, Q., Liu, H., Wang, P., Dai, W., Zhang T., Zhao, Y., Tian, J., Zhang, W., Han, Y., and Cao, J.: Optical source apportionment and radiative effect of light-absorbing carbonaceous aerosols in a tropical marine monsoon climate zone: the importance of ship emissions, Atmos. Chem. Phys., 20, 15537–15549, https://doi.org/10.5194/acp-20-15537-2020, 2020.

Wang, W., Chen, N., and Ma, X., Characteristic analysis on mountain-valley wind in deep valley, Adv. Mater. Vols 610-613, pp 817-824, https://doi:10.4028/www.scientific.net/AMR.610-613.817, 2013.

Wei, N., Wang, N., Huang, X., Liu, P., and Chen, L.: The effects of terrain and atmospheric dynamics on cold season heavy haze in the Guanzhong Basin of China, Atmos. Pollut. Res., 11, 1805-1819, https://doi.org/10.1016/j.apr.2020.07.007, 2020.

Wehrens, R., and Kruisselbrink, J.: Supervised and unsupervised self-organising maps, Package 'kohonen', 2019, https://cran.r-project.org/.

Wu, J., Kong, S., Wu, F., Cheng, Y., Zheng, S., Qin, S., Liu, X., Yan, Q., Zheng, H., Zheng, M., Yan, Y., Liu, D., Ding, S., Zhao, D., Shen, G., Zhao, T., and Qi, S.: The moving of high emission for biomass burning in China: view from multiyear emission estimation and human-driven forces, Environ. Int., 142, 105812, https://doi.org/10.1016/j.envint.2020.105812, 2020.

Wu, C. and Yu, J. Z.: Determination of primary combustion source organic carbon-to-elemental carbon (OC / EC) ratio using ambient OC and EC measurements: secondary OC-EC correlation minimization method, Atmos. Chem. Phys., 16, 5453–5465, https://doi.org/10.5194/acp-16-5453-2016, 2016.

Xiao, S., Wang, Q., Cao, J., Huang, R., Chen, W., Han, Y., Xu, H., Xu, H., Liu, S., Zhou, Y., Wang, P., Zhang, J., Zhan, C.: Long-term trends in visibility and impacts of aerosol composition on visibility impairment in Baoji, China, Atmos. Res., 149, 88–95, http://dx.doi.org/10.1016/j.atmosres.2014.06.006, 2014.

Xu, H. M., Cao, J. J., Ho, K. F., Ding, H., Han, Y. M., Wang, G. H., Chow, J. C., Watson, J. G., Khol, S. D., Qiang, J., and Li, W. T.: Lead concentrations in fine particulate matter after the phasing out of leaded gasoline in Xi'an, China, Atmos. Environ., 46, 217– 224, https://doi.org/10.1016/j.atmosenv.2011.09.078, 2012.

Xu, H., Ren, Y., Zhang, W., Meng,W., Yun, X., Yu, X., Li, J., Zhang, Y., Shen, G., Ma, J., Li, B., Cheng, H., Wang, X., Wan, Y., and Tao, S.: Updated global black carbon emissions from 1960 to 2017: improvements, trends, and drivers, Environ. Sci. Technol., 55, 7869-7879, https://doi.org/10.1021/acs.est.1c03117, 2021.

Xu, H., Cao, J., Chow, J., Huang, R., Shen, Z., Chen, L.W., Ho, K., Watson, J.: Inter-annual variability of wintertime PM$_{2.5}$ chemical composition in Xi'an, China: evidences of changing source emissions, Sci. Total Environ., 545, 546–555, http://dx.doi.org/10.1016/j.scitotenv.2015.12.070, 2016.

Yan, C., Zheng, M., Sullivan, A., Bosch, C., Desyaterik., Andersson, A., Li, X., Guo, X., Zhou, T., Gustafsson, O., Collett Jr., J.: Chemical characteristics and light-absorbing property of water soluble organic carbon in Beijing: biomass burning contributions, Atmos. Environ., 121, 4-12, http://dx.doi.org/10.1016/j.atmosenv.2015.05.005, 2015.

Yang, M., Howell, S. G., Zhuang, J., and Huebert, B. J.: Attribution of aerosol light absorption to black carbon, brown carbon, and dust in China – interpretations of atmospheric measurements during EAST-AIRE, Atmos. Chem. Phys., 9, 2035–2050, https://doi.org/10.5194/acp-9-2035-2009, 2009.

Yao, X., Chan, C. K., Fang, M., Cadle, S., Chan, T., Mulawa, P., He, K., and Ye, B.: The water-soluble ionic composition of PM2.5 in Shanghai and Beijing, China, Atmos. Environ., 36, 4223–4234, https://doi.org/10.1016/S1352-2310(02)00342-4, 2002.

Zhao, S., Tian, H., Luo, L., Liu, H., Wu, B., Liu, S., Bai, X., Liu, W., Liu, X., Wu, Y., Lin, S., Guo, Z., Lv, Y., and Xue, Y.: Temporal variation characteristics and source apportionment of metal elements in PM$_{2.5}$ in urban Beijing during 2018–2019, Environ. Pollut., 268, 115856, https://doi.org/10.1016/j.envpol.2020.115856, 2021.

删除了: Wang, Q., Cao, J., Han, Y., Tian, J., Zhu, C., Zhang, Y., Zhang, N., Shen, Z., Ni, H., Zhao, S., and Wu, J.: Sources and physicochemical characteristics of black carbon aerosol from the southeastern Tibetan Plateau: internal mixing enhances light absorption, Atmos. Chem. Phys., 18, 4639-4656, https://doi.org/10.5194/acp-18-4639-2018, 2018.

删除了: ,

删除了: Advanced Materials Research

删除了: View

设置了格式: 下标

删除了: B

设置了格式: 下标

Zhao, S., Tie, X., Cao, J., and Zhang, Q.: Impacts of mountains on black carbon aerosol under different synoptic meteorology conditions in the Guanzhong region, China, Atmos. Res., 164–165, 286–296, https://doi.org/10.1016/j.atmosres.2015.05.016, 2015

Zhao, S. P., Yu, Y., Yin, D., Yu, Z., Dong, L. X., Mao, Z., He, J. J., Yang, J., Li, P., and Qin, D. H.: Concentrations, optical and radiative properties of carbonaceous aerosols over urban Lanzhou, a typical valley city: results from in-situ observations and numerical model, Atmos. Environ., 213, 470–484, https://doi.org/10.1016/j.atmosenv.2019.06.046, 2019.

Zhang, Z., Gao, J., Engling, G., Tao, J., Chai, F., Zhang, L., Zhang, R., Sang, X., Chan, C., Lin, Z., and Cao, J.: Characteristics and applications of size-segregated biomass burning tracers in China's Pearl River Delta region, Atmos. Environ., 102, 290–301. https://doi.org/10.1016/j.atmosenv.2014.12.009, 2015.

Zhang, J. P., Zhu, T., Zhang, Q. H., Li, C. C., Shu, H. L., Ying, Y., Dai, Z. P., Wang, X., Liu, X. Y., Liang, A. M., Shen, H. X., and Yi, B. Q.: The impact of circulation patterns on regional transport pathways and air quality over Beijing and its surroundings, Atmos. Chem. Phys., 12, 5031–5053, https://doi.org/10.5194/acp-12-5031-2012, 2012.

Zhang, Y., Li, M., Cheng, Y., Geng, G., Hong, C., Li, H., Li, X., Tong, D., Wu, N., Zhang, X., Zheng, B., Zheng, Y., Bo, Y., Su, H., and Zhang, Q.: Modeling the aging process of black carbon during atmospheric transport using a new approach: a case study in Beijing, Atmos. Chem. Phys., 19, 9663–9680, https://doi.org/10.5194/acp-19-9663-2019, 2019.

Zhou, B., Wang, Q., Zhou, Q., Zhang, Z., Wang, G., Fang, N., Li, M., Cao, J.: Seasonal characteristics of black carbon aerosol and its potential source regions in Baoji, China, Aerosol Air. Qual. Res., 18, 397–406, https://doi.org/10.4209/aaqr.2017.02.0070, 2018.

Zotter, P., Herich, H., Gysel, M., El-Haddad, I., Zhang, Y., Močnik, G., Hüglin, C., Baltensperger, U., Szidat, S., and Prévôt, A. S. H.: Evaluation of the absorption Ångström exponents for traffic and wood burning in the Aethalometer-based source apportionment using radiocarbon measurements of ambient aerosol, Atmos. Chem. Phys., 17, 4229–4249, https://doi.org/10.5194/acp-17-4229-2017, 2017

删除了: Results

Table 1. The mass concentration of eBC from fossil fuel combustion (eBC_{fossil}) and eBC from biomass burning ($eBC_{biomass}$) associated with different clusters under four featured atmospheric motions

Motion category	Local scale dominance (LD) (40%)				Local scale strong and regional scale weak (LSRW) (17%)			
	L_{bj} = 70.9 km, S_{bj} = 107.8 km, R_{bj} = 0.35, R_{std} = 0.25				L_{bj} = 106.9 km, S_{bj} = 164.8 km, R_{bj}=0.33, R_{std} = 0.23			
	Cluster 1	Cluster 2	Cluster 3	Total average	Cluster 1	Cluster 2	Cluster 3	Total average
Trajectory percentage (%)	45	52	3	100	56	33	11	100
eBC_{fossil} ($\mu g\ m^{-3}$)	2.82[a] ± 1.59[b]	3.2 ± 1.73	3.64 ± 0.67	3.08 ± 2.07	2.42 ± 1.00	3.43 ± 1.17	2.89 ± 1.00	2.79 ± 1.73
$eBC_{biomass}$ ($\mu g\ m^{-3}$)	1.34 ± 1.07	1.72 ± 1.29	0.67 ± 0.87	1.52 ± 1.19	1.0 ± 0.85	1.17 ± 0.84	1.00 ± 0.64	1.06 ± 0.83

L_{bj}—resultant transport distance, S_{bj}—actual wind run distance at 100 m, R_{bj} —recirculation factor at 100 m, R_{std}—standard deviation for recirculation factor. a and b: Mean ± Standard deviation.

Table 1 (continued)

Motion category	Local scale weak and regional scale strong (LWRS) (14%)				Regional scale dominance (RD) (29%)			
	L_{bj} =159 km, S_{bj} = 183.4 km, R_{bj}=0.13, R_{std} = 0.20				L_{bj} =235.6 km, S_{bj} = 246.4 km, R_{bj}= 0.05, R_{std} = 0.18			
	Cluster 1	Cluster 2	Cluster 3	Total average	Cluster 1	Cluster 2	Cluster 3	Total average
Trajectory percentage (%)	42	22	36	100	41	20	39	100
eBC_{fossil} ($\mu g\ m^{-3}$)	1.32[a] ± 0.67[b]	2.02 ± 0.73	3.16 ± 1.19	2.15 ± 1.62	1.00 ± 0.64	1.02 ± 0.88	2.75 ± 1.26	1.69 ± 1.36
$eBC_{biomass}$ ($\mu g\ m^{-3}$)	0.67 ± 0.49	0.73 ± 0.47	1.19 ± 0.60	0.86 ± 0.58	0.64 ± 0.63	0.87 ± 0.69	1.26 ± 0.68	0.93 ± 0.72

L_{bj}—resultant transport distance, S_{bj}—actual wind run distance at 100 m, R_{bj} —recirculation factor at 100 m, R_{std}—standard deviation for recirculation factor. a and b: Mean ± Standard deviation.

删除了: Table 1. The mass concentration of eBC from fossil fuel combustion (eBC_{fossil}) and eBC from biomass burning ($eBC_{biomass}$) associated with different clusters under four featured atmospheric motions

...

Table 2. Direct radiative forcing efficiencies for equivalent black carbon (eBC) from fossil fuel combustion (eBC$_{\text{fossil}}$) and the eBC from biomass burning (eBC$_{\text{biomass}}$) under four atmospheric motion categories

Atmospheric motion category	DRE$_{\text{eBCfossil, ATM}}$ efficiency ((W m^{-2})/(μg m^{-3}))	DRE$_{\text{eBCbiomass, ATM}}$ efficiency ((W m^{-2})/(μg m^{-3}))
Local scale dominance (LD)	10.2[a] ± 4.2[b]	10.3 ± 4.4
Local scale strong and regional scale weak (LSRW)	10.6 ±5.7	10.2 ± 5.8
Local scale weak and regional scale strong (LWRS)	13.5 ± 6.7	14.7 ± 8.1
Regional scale dominance (RD)	15.6 ± 8.9	15.5 ± 8.4

a and b: Mean ± Standard deviation

删除了: T

删除了: he DRE$_{\text{eBC, ATM}}$ efficiencies of the eBC from fossil fuel combustion (eBC$_{\text{fossil}}$) and the eBC from biomass burning (eBC$_{\text{biomass}}$) under the four featured atmospheric motions

删除了: [a]

删除了: [a]

格式化表格

设置了格式: 上标

设置了格式: 上标

删除了: LD

删除了: LSRW

删除了: LWRS

删除了: RD

删除了: a: Mean ± Std

Figure captions:

Figure 1. Four factors identified by source apportionment. Concentration (μg m^{-3}) of the chemical species and primary absorption (p_{abs}) (λ) at six wavelengths (λ = 370, 470, 520, 590, 660, or 880nm) (M m^{-1}) for each source are shown in grey. The blue square represents the contribution of each chemical species to the four different factors.

Figure 2. (a) Diel variations of the eBC from fossil fuel combustion (eBC$_{fossil}$) and (b) the eBC from biomass burning (eBC$_{biomass}$), (c) wind speed (m s^{-1}) and (d) planetary boundary layer height (m). The black bars of each hourly-averaged point show the standard deviation.

Figure 3. (a) The 75th – 100th percentile mass concentrations of the eBC from fossil fuel combustion (eBC$_{fossil}$) and (b) the eBC from biomass burning (eBC$_{biomass}$) under local scale dominance (LD, red circle), local scale strong and regional scale weak (LSRW, green circle), local scale weak regional scale strong (LWRS, purple circle) and regional scale dominance (RD, blue circle). S_{bj} is actual wind run distance at 100m height, R_{bj} is the recirculation factor, the grey area indicates good ventilation ($S_{bj} \geq$ 250km, $R_{bj} \leq 0.2$), the yellow area indicates air stagnation (S_{bj} 130km).

Figure 4. Mass concentrations of the eBC from fossil fuel combustion (eBC$_{fossil}$) and the eBC from biomass burning (eBC$_{biomass}$) during daytime (a, c) and nighttime (b, d) under local scale dominance (LD); local scale strong and regional scale weak (LSRW); local scale weak regional strong (LWRS); and regional scale dominance (RD).

删除了: b_{abs}

删除了: in

删除了: are colored by

删除了: in

删除了: The

删除了: d

删除了: ,

删除了: the

删除了: the

删除了: ,

删除了: t

删除了: is

设置了格式: 字体: 10 磅

删除了: (a) The 75th – 100th percentile mass concentrations of the eBC from fossil fuel combustion (eBC$_{fossil}$) and (b) the eBC from biomass burning (eBC$_{biomass}$) under local dominance (LD), local strong and regional weak (LSRW), local weak regional strong (LWRS) and regional dominance (RD). S_{bj} is actual wind run distance at 100m height, R_{bj} is the recirculation factor.

Figure 5. Direct radiative effect (DRE) of the eBC from fossil fuel combustion (eBC$_{fossil}$) shaded in grey and the eBC from biomass burning (eBC$_{biomass}$) shaded in grey yellow (a) in the top atmosphere (TOA), surface (SUF), and the atmosphere atmospheric column (ATM) and (b) the DRE$_{eBC,ATM}$ of two types of eBC under local dominance (LD) shaded in light grey labeled as LD, local strong and regional weak (LSRW) shaded in light blue labeled as LSRW, local weak regional strong (LWRS) shaded in light grey labeled with LWRS and regional dominance (RD) shaded in light blue labeled as RD (c) DRE efficiencies of eBC$_{biomass}$ (shaded in yellow) and eBC$_{fossil}$ (shaded by grey) in TOA, SUF and ATM (d) DRE efficiencies of eBC$_{biomass}$ and eBC$_{fossil}$ at ATM under LD (shaded in light grey labeled as LD), LSRW (shaded in light blue labeled as LSRW), LWRS (shaded in light grey labeled as LWRS) and RD (shaded in light blue labeled with RD).

删除了: (a) The Mmass concentrations of the eBC from (a) fossil fuel combustion (eBC$_{fossil}$) and (b) the eBC from biomass burning (eBC$_{biomass}$) during daytime and (c,d) nighttime under local dominance (LD); local strong and regional weak (LSRW); local weak regional strong (LWRS); and regional dominance (RD).

删除了: by

删除了: by

删除了: in-between

删除了: by

删除了: l

删除了: with

删除了: by

删除了: l

删除了: with

删除了: by

删除了: l

删除了: by

删除了: l

删除了: with

删除了: by grey

删除了: by

删除了: l

删除了: with

删除了: by

删除了: l

删除了: with

删除了: by

删除了: l

删除了: with

删除了: by

删除了: l

删除了: Direct radiative effect (DRE) of the eBC from fossil fuel combustion (eBC$_{fossil}$) and the eBC from biomass burning (eBC$_{biomass}$) (a) in the top atmosphere (TOA), surface (SUF), and in-between the atmosphere (ATM) and (b) the DRE$_{eBC,ATM}$ of two types of eBC under local dominance (LD), local strong and regional weak (LSRW), local weak regional strong (LWRS) and regional dominance (RD)

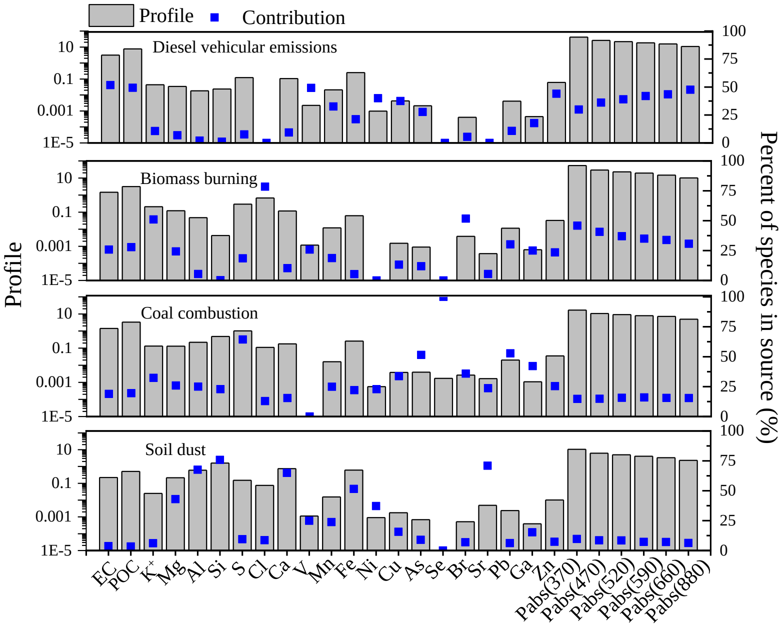

Figure 1. Four factors identified by source apportionment. Concentration (μg m^{-3}) of the chemical species and primary absorption coefficients (p_{abs}) (λ) at six wavelengths (λ = 370, 470, 520, 590, 660, or 880nm) (M m^{-1}) for each source are shown in grey. The blue square represents the contribution of each chemical species to the four different factors.

删除了: Four factors identified by source apportionment. Concentration (μg m^{-3}) of the chemical species and b_{abs} p_{abs} (λ) at six wavelengths (λ = 370, 470, 520, 590, 660, or 880nm) (M m^{-1}) in each source are colored by grey. The blue square represents the contribution of each chemical species in the four different factors.

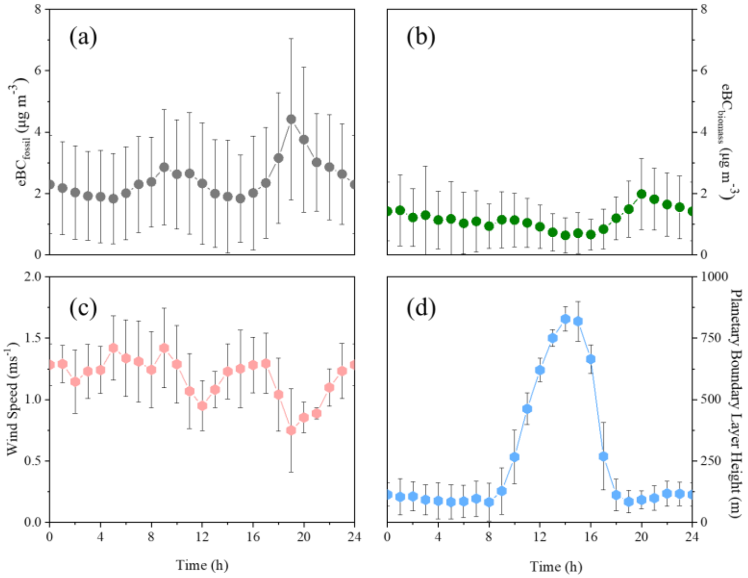

Figure 2. (a) (a) Diel variations of the eBC from fossil fuel combustion (eBC$_{fossil}$) and (b) the eBC from biomass burning (eBC$_{biomass}$), (c) wind speed (m s^{-1}) and (d) planetary boundary layer height (m). The black bars of each hourly-averaged point show the standard deviation.

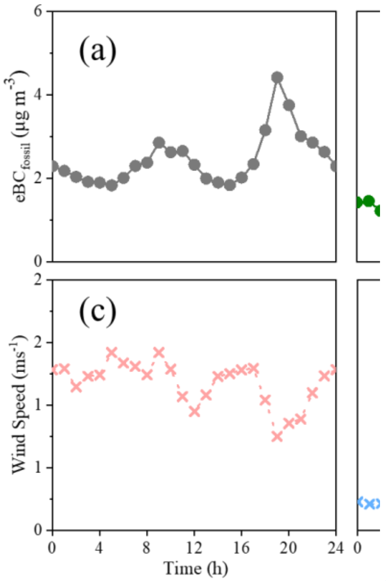

删除了:

带格式的: 段落间距段前: 6 磅, 段后: 0 磅

删除了: The diurnal diel variations of the eBC from fossil fuel combustion (eBC$_{fossil}$), (b) the eBC from biomass burning (eBC$_{biomass}$), (c) the wind speed (m s^{-1}) and (d) the planetary boundary layer height (m).
, the black bar of each hourly-averaged point is the standard deviation

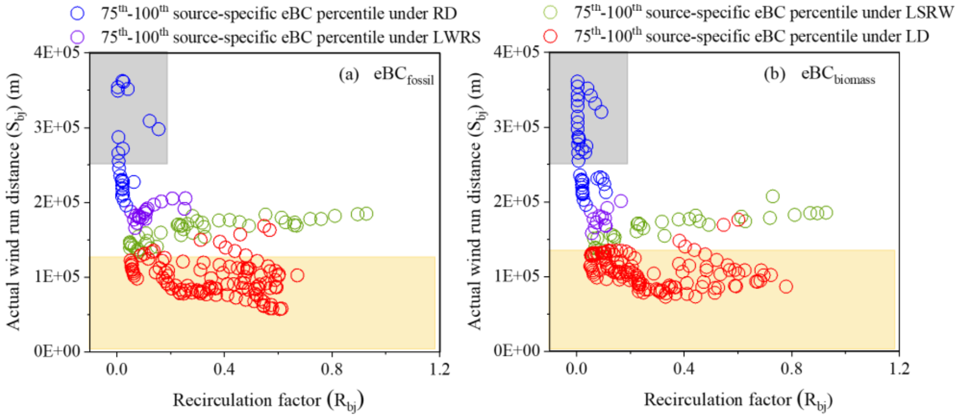

Figure 3. (a) The 75th – 100th percentile mass concentrations of the eBC from fossil fuel combustion (eBC$_{fossil}$) and (b) the eBC from biomass burning (eBC$_{biomass}$) under local scale dominance (LD, red circle), local scale strong and regional scale weak (LSRW, green circle), local scale weak regional scale strong (LWRS, purple circle) and regional scale dominance (RD, blue circle). S_{bj} is actual wind run distance at 100m height, R_{bj} is the recirculation factor, the grey area indicates good ventilation ($S_{bj} \geq$ 250km, $R_{bj} \leq$ 0.2), the yellow area indicates air stagnation ($S_{bj} \leq$130km).

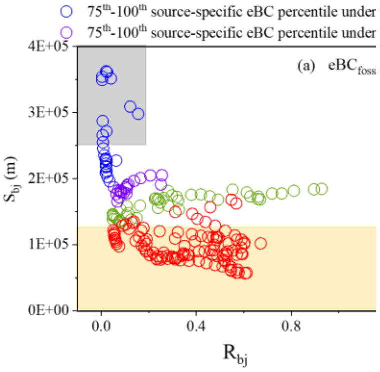

删除了:

带格式的: 段落间距段前：6 磅，段后：0 磅

删除了: (a) The 75th – 100th percentile mass concentrations of the eBC from fossil fuel combustion (eBC$_{fossil}$) and (b) the eBC from biomass burning (eBC$_{biomass}$) under local dominance (LD, red circle), local strong and regional weak (LSRW, green circle), local weak regional strong (LWRS, purple circle) and regional dominance (RD, blue circle). S_{bj} is actual wind run distance at 100m height, R_{bj} is the recirculation factor, the gray areas indicates good ventilation ($S_{bj} \geq$ 250km, $R_{bj} \leq$ 0.2), the yellow area indicates air stagnation (S_{bj} 130km)

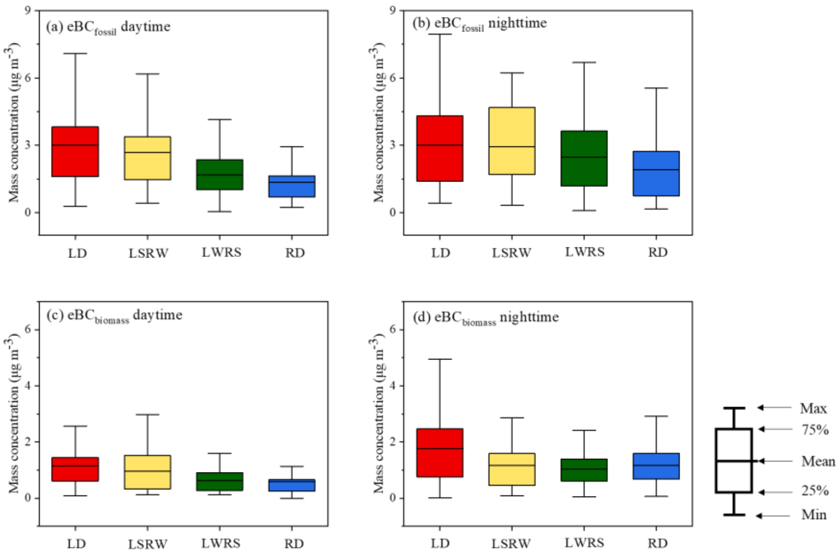

Figure 4. Mass concentrations of the eBC from fossil fuel combustion (eBC$_{fossil}$) and the eBC from biomass burning (eBC$_{biomass}$) during daytime (a, c) and nighttime (b, d) under local scale dominance (LD); local scale strong and regional scale weak (LSRW); local scale weak regional strong (LWRS); and regional scale dominance (RD).

删除了: The mass concentrations of the eBC from fossil fuel combustion (eBC$_{fossil}$) and (b) the eBC from biomass burning (eBC$_{biomass}$) during daytime and (c,d) nighttime under local dominance (LD); local strong and regional weak (LSRW); local weak regional strong (LWRS); and regional dominance (RD).…

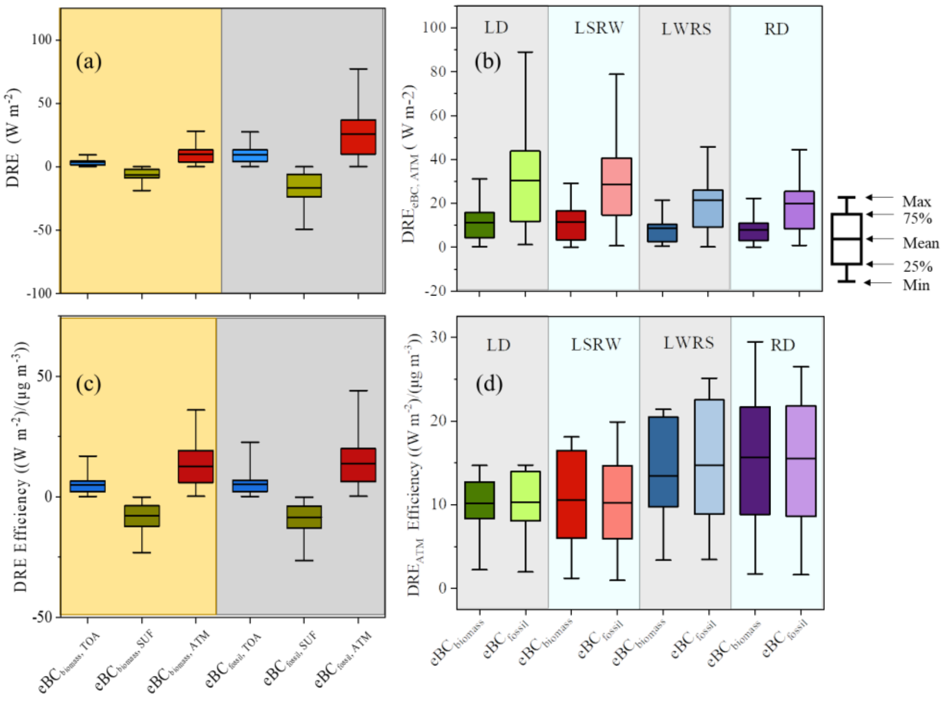

Figure 5. Direct radiative effect (DRE) of the eBC from fossil fuel combustion (eBC$_{fossil}$) shaded in grey and the eBC from biomass burning (eBC$_{biomass}$) shaded in yellow (a) in the top atmosphere (TOA), surface (SUF), and the atmosphere atmospheric column (ATM) and (b) the DRE$_{eBC,ATM}$ of two types of eBC under local dominance (LD) shaded in light grey labeled as LD, local strong and regional weak (LSRW) shaded in light blue labeled as LSRW, local weak regional strong (LWRS) shaded in light grey labeled with LWRS and regional dominance (RD) shaded in light blue labelled as RD (c) DRE efficiencies of eBC$_{biomass}$ (shaded in yellow) and eBC$_{fossil}$ (shaded by grey) in TOA, SUF and ATM (d) DRE efficiencies of eBC$_{biomass}$ and eBC$_{fossil}$ at ATM under LD (shaded in light grey labeled as LD), LSRW (shaded in light blue labeled as LSRW), LWRS (shaded in light grey labeled as LWRS) and RD (shaded in light blue labeled with RD).

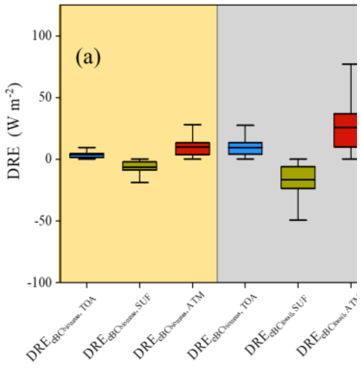

删除了:

设置了格式: 非突出显示

设置了格式: 非突出显示

删除了: Direct radiative effect (DRE) of the eBC from fossil fuel combustion (eBC$_{fossil}$) shaded by grey and the eBC from biomass burning (eBC$_{biomass}$) shaded by grey yellow (a) in the top atmosphere (TOA), surface (SUF), and in-between the atmosphere (ATM) and (b) the DRE$_{eBC,ATM}$ of two types of eBC under local dominance (LD) shaded by light grey labelled with LD, local strong and regional weak (LSRW) shaded by light blue labelled with LSRW, local weak regional strong (LWRS) shaded by light grey labelled with LWRS and regional dominance (RD) shaded by light blue labelled with RD. (c) DRE efficiencies of eBC$_{biomass}$ (shaded by grey yellow) and eBC$_{fossil}$ (shaded by grey) in TOA, SUF and ATM (d) DRE efficiencies of eBC$_{biomass}$ and eBC$_{fossil}$ at ATM under LD (shaded by light grey labelled with LD), LSRW (shaded by light blue labelled with LSRW), LWRS (shaded by light grey labelled with LWRS) and RD (shaded by light blue labelled with RD).

删除了:

Comment on acp-2022-26 titled "Review of "The impact of atmospheric motion on source-specific black carbon and the induced direct radiative effect over a river-valley region" by Liu et al.

Anonymous Referee #2

General comment

The site location should be described in more detail, and also earlier on. Some more comments on this issue are below.

Response: We have taken the suggestion to heart and have added more details about the location description. The revised site description now reads:

"Baoji is a typical river-valley city, located at the furthest west of the Guanzhong Plain, at an altitude from 450 to 800 m a.s.l. (Figure S1), Baoji has a complex topography and often suffering from severe pollution in winter. It is surrounded by mountains to the south, west and north, with the Weihe River as the central axis extending eastward. The shape can be viewed as a funnel, with large opening to east. The Qinling peaks and the flat Weihe Plain are the main landforms of Baoji. The main peak of the Qinling Mountains is 3,767 m a.s.l. and it is the highest mountain in the eastern part of mainland China. This terrain causes divergent flow at local scales, which can impact pollution levels (Wei et al., 2020). Baoji also is an important railway intersection in China, connecting six railways to the north-west and southwest China. Pollutant levels can be high and pollutants are not easy to be dispersed in the city due to its special topographic conditions, dense population (total population of 0.341 million, with 63.5% population living in the downtown aera and population density of 6003 people per km^2 in 2019 (http://tjj.shaanxi.gov.cn/upload/2021/zk/indexch.htm and https://data.chinabaogao.com/hgshj/2021/042053X932021.html), and impacts from major highway and railway networks.

The sampling site was on the rooftop of a building at Baoji University of Arts and Sciences (34°21′16.8″N, 107°12′59.6″E, 569 m a.s.l.) surrounded by commercial and residential buildings, highways, and a river, there were no major industrial emission sources nearby. The main sources of BC in Baoji were the domestic fuel (coal and biomass) burning as well as the motor vehicle emissions (Zhou et al., 2018; Xiao et al., 2014). Open fire also can be sources for BC, but there were limited fire found scattered around the site (Figure S2). The meteorological conditions at Baoji for the four seasons are listed in Table S1, and the wind roses for the different seasons are shown in Figure S3(data are from the Meteorological Institute of Shaanxi Province)."

Table R1 The seasonal meteorological data of Baoji

Season	Temperature (℃)	Relative humidity (%)	Precipitation in last hour (mm)
Winter	2.7	60.6	0.025
Spring	11.5	54.9	0.042
Summer	23.7	67.1	0.139
Autumn	20.2	67.0	0.074

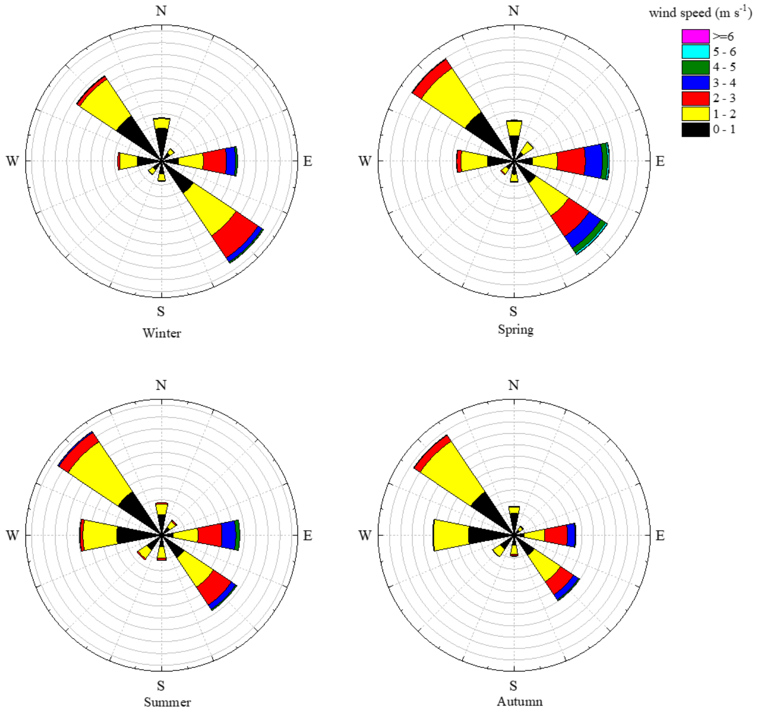

Figure R1 Seasonal wind roses for Baoji.

The English grammar and style could be quite significantly improved. A few examples of some issues are provided in the specific comments below, but many more instances are present in the paper. Maybe some editorial work by a native-speaking scientist could help improve the language and therefore clarity.

Response: Thanks for pointing out those grammatical mistakes in the specific comments and as suggested we had the paper polished by a native English speaker.

The origin of the biomass burning BC is not well described or discussed. Is this agricultural biomass burning, wildfires, or residential biomass burning? Something else?

Response: The field sampling happened in winter (from 16th November 2018 to 21st December 2018), in Baoji wildfires were comparatively sparser, we screenshotted the fire map (data from MODIS/Aqura, MODIS/Terra and VIIRS 375m/Suomi NPP) from NASA, as shown in Figure R2. Although China has banned agriculture biomass burning due to the air pollution, a lack of strict supervision leads to a few illegal burning in rural areas. Biomass (e.g. straw and crop) is one of the common solid fuel for residential heating and home cooking in winter which causes severe air pollution (Wu et al., 2019). Thus, we believe the biomass burning BC could be from all the three sources but residential biomass burning may take the major responsibility. We have added the potential emission sources of BC at study site in the section 2.1 Research site, see the response above.

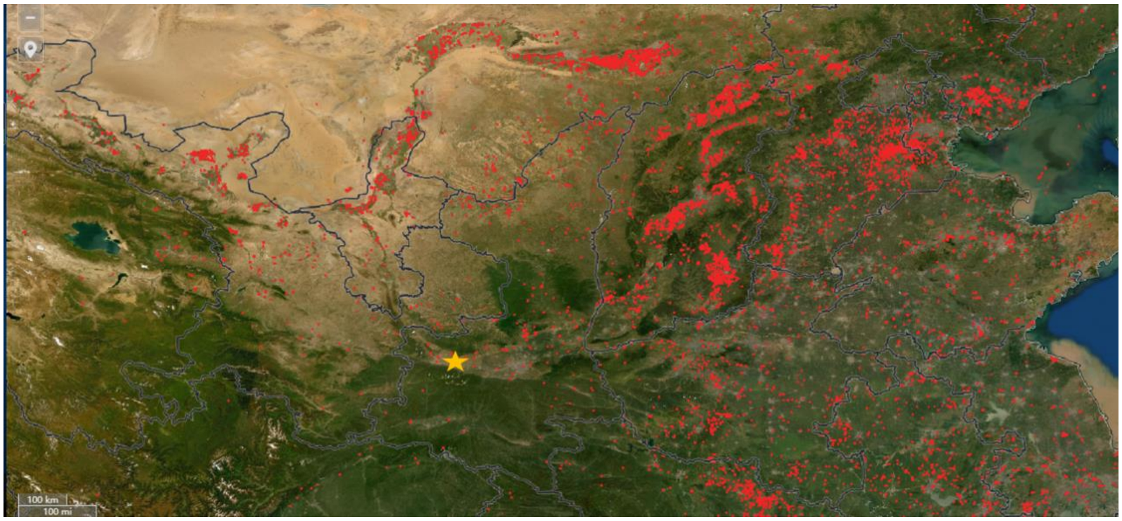

Figure R2. Map of fire occurrences. The yellow star represents the study site, the red dots represent the fire. The image from © NASA (National Aeronautics and Space Administration) (https://firms.modaps.eosdis.nasa.gov/map).

Reference:

Wu S., Zheng, X., You, C., and Wei, C.: Household energy consumption in rural China: Historical development, present pattern and policy implication, Journal of Cleaner Production, 211, 981-991, https://doi.org/10.1016/j.jclepro.2018.11.265, 2019.

The literature citations are a bit scarce and somewhat biased. A broader representation of the work published in the literature and relevant to the authors' work outside of their own work, would help.

Response: We reviewed more studies and replaced some of the research citation from our work. In addition, we added the comparison of studies on BC pollution and the total DRE of BC in other river valley sites. The revised part is shown was following:

"The mean values of eBC$_{\text{fossil}}$ and eBC$_{\text{biomass}}$ were 2.46 μg m^{-3} and 1.17 μg m^{-3}, respectively. The averaged total eBC mass concentration (± standard deviation) was 3.63±2.73μg m^{-3}, and the eBC ranged from varying from 0.39 to 12.73 μg m^{-3} during the study period, The averaged mass concentration was comparable to that in Lanzhou, another river valley city in China, that was sampled in the same season (5.1 ± 2.1, Zhao et al.,2019). The lowest value is comparable to other river valley regions such as in Retje in India (Glojek et al., 2022) or in Urumqi River Valley in China (Zhang et al., 2020), however even the highest concentration was much lower than that in other urban regions (Table S5)."

"The DRE$_{\text{eBC, TOA}}$ and DRE$_{\text{eBC, SUF}}$ of eBC were 13 W m^{-2} and -22.9 W m^{-2}, which were lower than that reported in Lanzhou (21.8 W m^{-2} and -47.5 W m^{-2} for DRE$_{\text{eBC, TOA}}$ and DRE$_{\text{eBC, SUF}}$) – which is another a river valley city in China (Zhao et al., 2019). This could be due to fact that the eBC mass concentration in Baoji was lower than in Lanzhou (Table S5). As for the DRE$_{\text{eBC, TOA}}$ and DRE$_{\text{eBC, SUF}}$ per an unit mass of BC, the results of the two studies were comparable."

Table R2 Mean (range) BC mass concentration in river valley sites worldwide.

Reference	BC concentration ($\mu g\ m^{-3}$)	Season	Topographic conditions	Altitude	Station type	Year
This study	3.63±2.73 (0.39~12.73)	November~December (winter)	river valley	450 to 800 m a.s.l.	urban	2018
Glojek et al., (2020)	0.9~40	December~January (winter)	river valley	715 m a.s.l.	rural	2017-2018
Zhao et al. (2015)	25±11	January (winter)	river valley	410 m a.s.l.	urban	2013
Barman and Gokhale (2019)	20.58~22.44	Winter	river valley		urban	2016-2017
Zhang et al., 2020	0.102~1.525	Winter	river valley	2130 m a.s.l.	rural	2016-2017
Chakrabarty et al., (2012)	9~41	January~February (winter)	river valley		urban	2011
Zhao et al. (2019)	5.1 ± 2.1	December~January (winter)	river valley		urban	2018
Tiwari et al., 2016	8.19 ±1.39	December-February (winter)	river valley	55 m a.s.l.	urban	2013-2014

Reference:

Barman, N., and Gokhale, S., Urban black carbon - source apportionment, emissions and long-range transport over the Brahmaputra River Valley, Science of the Total Environment, 693, 133577, https://doi.org/10.1016/j.scitotenv.2019.07.383, 2019

Chakrabarty, R., Garro, M., Wilcox, E., and Moosmuller, H., Strong radiative heating due to wintertime black carbon aerosols in the Brahmaputra River Valley, Geophysical Research Letters, 39, L09804, https://doi.org/10.1029/2012GL051148, 2012.

Glojek, K., Moˇcnik, G., Alas, H., et al., The impact of temperature inversions on black carbon and particle mass concentrations in a mountainous area, Atmos. Chem. Phys., 22, 5577–5601, https://doi.org/10.5194/acp-22-5577-2022, 2022.

Zhang, X., Li, Z., Ming, J., and Wang, F., One-Year Measurements of Equivalent Black Carbon, Optical Properties, and Sources in the Urumqi River Valley, Tien Shan, China, Atmosphere, 11, 478, https://doi.org/10.3390/atmos11050478, 2020.

Zhao, S., Yu, Y., Yin, D., et al., Concentrations, optical and radiative properties of carbonaceous aerosols over urban Lanzhou, a typical valley city: Results from in-situ observations and numerical model, Atmospheric Environment, 213, 470–484, https://doi.org/10.1016/j.atmosenv.2019.06.046, 2019.

Zhao, S., Tie, X., Cao, J & Zhang, Q. (2015), Impacts of mountains on black carbon aerosol under different synoptic meteorology conditions in the Guanzhong region, China. Atmospheric Research, 164-165, 286-296. http://dx.doi.org/10.1016/j.atmosres.2015.05.016

Tiwari, S., Kumar, R., Tunved, P., Singh, S., and Panicker, A., Significant cooling effect on the surface due to soot particles over Brahmaputra River Valley region, India: An impact on regional climate, 2016, Science of the Total Environment, 562, 504–516, http://dx.doi.org/10.1016/j.scitotenv.2016.03.157, 2016.

Maybe is my lack of familiarity with some of these aspects, but some of the data analysis methods (e.g., SOM, but not only) are not described in sufficient detail. The authors refer to existing literature, but a brief description of the methods' workings, input, outputs, limitations, etc. would help improve the clarity and broaden the audience of the paper.

Response: We are truly grateful for reviewer's comments and suggestion. We revised the methods to provide more details particularly for the optical source apportionment and SOM. Other methods also have been revised according to the reviewer's suggestions. In addition, we have provided information regarding the cluster analysis and minimum R squared method in the supplementary materials. The changes are shown in the revised version. The revised paragraphs now read as follows:

"2.2 Sampling and laboratory measurements

eBC and the absorption coefficients (b_{abs}) at 370, 470, 520, 590, 660, 880, and 950 nm wavelength were measured using an AE33 aethalometer (Magee Scientific, Berkeley, CA, USA) equipped with a $PM_{2.5}$ cut-off inlet (SCC 1.829, BGI Inc. USA) that had a time resolution of 1 min. A Nafion® dryer (MD-700-24S-3; Perma Pure, Inc., Lakewood, NJ, USA) with a flow rate of 5 L min^{-1} was used to dry the $PM_{2.5}$ before the measurement. Briefly, the particles were dried by the Nafion® dryer before being measured with the AE33 aethalometer, and the deposited particles were irradiated by light-emitting diodes at seven wavelengths of light-emitting diodes (λ = 370, 470, 520, 590,660, 880, and 950 nm), and the light attenuation was detected. The non-linear loading issue for filter-based absorption measurement was accounted for in the AE33 by a technique called dual-spot compensation. The quartz filter (PN8060) matrix scattering effect was corrected by using a factor of 1.39. More details of AE33 measurement techniques can be found in Drinovec et al. (2015).

The scattering coefficient (b_{scat}) at a single (525) nm wavelength was measured with the use of a nephelometer (Aurora-1000, Ecotech, USA) that had a time resolution of 5 min. The nephelometer and aethalometer operated simultaneously and used the same $PM_{2.5}$ cyclone and Nafion® dryer. The calibration was conducted based on the user guide with a calibration gas R-134. Zero calibrations were conducted every other day by using clean air without particles. The ambient air was drawn in through a heated inlet with a flow rate of 5 L min^{-1}. The relative humidity remained lower than 60%.

$PM_{2.5}$ samples were collected for every 24 hours (h) from 10 a.m. local time to the 10 a.m. the next day from 16th November 2018 to 21st December 2018 with two sets of mini-volume samplers (Airmetrics, USA), one using quartz fiber filters (QM/A; Whatman, Middlesex, UK) and the other with Teflon® filters (Pall Corporation, USA), both with a flow rate of 5 L min^{-1}. Those samples were kept in a refrigerator at 4°C before analysis. The mass concentration of K^+ in the $PM_{2.5}$ quartz sample was extracted in a separate 15 mL vials containing 10 mL distilled deionized water (18.2 MΩ resistivity). The vials were placed in an ultrasonic water bath and shaken with a mechanical shaker for 1 h to extract the ions and determined by a Metrohm 940 Professional IC Vario (Metrohm AG., Herisau, Switzerland) with Metrosep C6-150/4.0 column (1.7 mmol/L nitric acid+1.7 mmol/L dipicolinic acid as the eluent) for cation analysis. A group of elements (i.e. Mg, Al, Si, S, Cl, Ca, V, Mn, Fe, Ni, Cu, As, Se, Br, Sr, Pb, Ga, and Zn) on the Teflon® filters was were determined by energy-dispersive x-ray fluorescence (ED-XRF) spectrometry (Epsilon 4 ED-XRF, PANalytical B.V., Netherlands). The X-rays were generated from a gadolinium anode on a side-window X-ray tube. A spectrum of the ratio of X-ray and photon energy was obtained after 24 minutes of analysis for each sample with each energy peak characteristic of a specific element, and the peak areas were proportional to the concentrations of the elements. Quality control was conducted on a daily basis with test standard sample.

Organic carbon (OC) and elemental carbon (EC) in each sample were determined with the use of a DRI Model 2001 Thermal/Optical Carbon Analyzer (Atmoslytic Inc., Calabasas, CA, USA). The thermal/optical reflectance (TOR) method and IMPROVE_A protocol were used for analysis. A punch of a quartz filter sample was heated at specific temperatures to obtain data for four OC fractions and three EC fractions. Total OC was calculated by summing all OC fractions and the pyrolyzed carbon (OP) produced. Total EC was calculated by summing all EC fractions minus the OP. Detailed methods and quality assurance/quality control processes were described in Cao et al., (2003). Primary organic carbon (POC) was estimated by using the minimum R-squared (MRS) method, which is based on using eBC as a tracer (Text S1). The method uses the minimum R^2 between OC and eBC to indicate where the ratio for which secondary OC and eBC are independent. A detailed description of the MRS method can be found in Wu et al., (2016).

Data for NO_x, wind speed, and direction at 12 ground monitoring sites were downloaded from http://sthjt.shaanxi.gov.cn/hx_html/zdjkqy/index.html. The wind data at 100 meters (m) above the ground and the planetary boundary layer height were downloaded from https://rda.ucar.edu/datasets/ds633.0. The data used for the Hybrid Single-Particle Lagrangian Integrated Trajectory (HYSPLIT) model was downloaded from Global Data Assimilation System and it had a resolution of 1°×1° (GDAS, https://www.ready.noaa.gov/gdas1.php). The data and main parameters used in trajectory model are listed in Table S2."

2.3 Optical source apportionment

The positive matrix factorization (PMF) model that was used for the optical source apportionment in this study. PMF solves chemical mass balance by decomposing the observational data into different source profiles and contribution matrices as follows:

$$X_{ij} = \sum_{k=1}^{p} g_{ik} f_{kj} + e_{ij} \qquad (1)$$

where X_{ij} denotes the input data matrix; p is the number of sources selected in the model; g_{ik} denotes the contribution of the k^{th} factor to the i^{th} input data; f_{kj} represents the k^{th} factor's profile of the j^{th} species; and e_{ij} represents the residual. Both g_{ik} and f_{kj} are non-negative. The uncertainties of each species and $b_{\text{abs}}(\lambda)$ were calculated by the equation recommended in EPA PMF5.0 user guideline(Norris et al, 2014) as follows:

$$Unc = \sqrt{(error\ fraction \times concentration(or\ ligth\ absorption\ coefficient))^2 + (0.5 \times MDL)^2} \qquad (2)$$

$$Unc = \frac{5}{6} \times MDL \qquad (3)$$

where MDL is the minimum detection limit of the method. When the concentration of a species was higher than the MDL then equation (2) was used otherwise equation (3) was used. In equation (2), for calculating the uncertainty of a chemical species, the error fraction was multiplied the concentration of the species. For calculating the uncertainty of optical data, the error fractions were multiplied by the light absorption coefficients.

Chemical species data (EC, POC, K^+, Mg, Al, Si, S, Cl, Ca, V, Mn, Fe, Ni, Cu, As, Se, Br, Sr, Pb, Ga and Zn) and the primary absorption coefficients (Pabs) data at λ=370nm,470nm,520nm,660nm, and 880nm were used for PMF analysis. The error fraction of offline measured data was the difference between multiple measurements of the same sample. The error fraction used for optical data was 10% based on Rajesh and Ramachandran (2018). PMF solves the equation (1) by minimizing the Q value, which is the sum of the normalized residuals' squares, as follows,

$$Q = \sum_{i=1}^{n} \sum_{j=0}^{n} \left[\frac{e_{ij}}{u_{ij}}\right]^2 \quad (4)$$

where u_{ij} represents the uncertainties of each X_{ij} and Q_{true}/Q_{exp} was used as the indicators for the factor number determination.

2.4 eBC source apportionment

The quantities of eBC generated from biomass burning versus fossil fuel combustion were deconvolved by an aethalometer model which uses Beer-Lambert's Law to write the absorption coefficients equations, wavelengths and absorption Ångström exponents (AAEs) for the two different BC emission sources (Sandradewi et. al., 2008). This approach is widely used for separating BC from two different sources based on optical data (Rajesh et al., 2018; Kant et al., 2019; Panicker et al., 2010). However, the traditional aethalometer model could be affected by the light absorbing substances at lower wavelengths such as dust and secondary formation particles. An improvement to the traditional aethalometer model was made, by explicitly considering the interference of the b_{abs} at a lower wavelength (370nm) caused by dust and secondary OC. Thus, the calculation of the absorption and source apportionment was based on the following equations (Wang et al., 2020):

$$\frac{b_{abs}(370)_{fossil}}{b_{abs}(880)_{fossil}} = \left(\frac{370}{880}\right)^{-AAE_{fossil}} \quad (5)$$

$$\frac{b_{abs}(370)_{biomass}}{b_{abs}(880)_{biomass}} = \left(\frac{370}{880}\right)^{-AAE_{biomass}} \quad (6)$$

$$b_{abs}(880) = b_{abs}(880)_{fossil} + b_{abs}(880)_{biomass} \quad (7)$$

$$b_{abs}(370) = b_{abs}(370)_{fossil} + b_{abs}(370)_{biomass} + b_{abs}(370)_{secondary} + b_{abs}(370)_{dust} \quad (8)$$

$$eBC_{fossil} = \frac{b_{abs}(880)_{fossil}}{MAC_{BC}(880)_{fossil}} \quad (9)$$

$$eBC_{biomass} = \frac{b_{abs}(880)_{biomass}}{MAC_{BC}(880)_{biomass}} \quad (10)$$

where AAE_{fossil} and $AAE_{biomass}$ are the AAEs for fossil fuel combustion and biomass burning. These were derived from the optical source apportionment by using PMF as discussed in section 3.1. Further, $b_{abs}(370)$ and $b_{abs}(880)$ are the total b_{abs} measured by the AE33 at the wavelengths of 370 nm and 880 nm respectively; $b_{abs}(370)_{fossil}$ and $b_{abs}(880)_{fossil}$ are the b_{abs} caused by emissions from fossil fuel combustion at those two wavelengths; $b_{abs}(370)_{biomass}$ and $b_{abs}(880)_{biomass}$ are the b_{abs} caused by emissions from biomass burning at those two wavelengths; $b_{abs}(370)_{dust}$ refers to the b_{abs} contributed by mineral dust at the wavelength of 370 nm, which was derived from the result of optical source apportionment; $b_{abs}(370)_{secondary}$ refers to the b_{abs} caused by the secondary aerosols at the wavelength of 370 nm, which was calculated by the minimum *R*-squared approach with eBC as a tracer (Text S1, Wang et al., 2019); eBC_{fossil} and $eBC_{biomass}$ are the eBCs from fossil fuel combustion and biomass burning; and $MAC_{BC}(880)_{fossil}$ and $MAC_{BC}(880)_{biomass}$ are the mass absorption cross-sections of eBC_{fossil} and the mass absorption cross-section of $eBC_{biomass}$ at the wavelength of 880 nm respectively, which were based on the PMF results for the optical source apportionments.

2.5 Indicators for the different scales of motion

The mathematical definitions of airflow condition proposed by Allwine and Whiteman (1994) were used in this study. The definitions quantify the flow features integrally at individual stations. Three variables were quantified, namely the actual wind run distance (*S*) which is the scalar displacement of the wind in 24 h (i.e.

the accumulated distance of the wind), the resultant transport distance (L) which is the vector displacement of the wind in 24 h (i.e. the straight line from the starting point to the end point), and the recirculation factor (R) is based on the ratio of L and S which indicates the frequency of the wind veering in 24 h. The influences of different scales of atmospheric motions were assessed based on the method proposed by Levy et al., (2010), and for this, we used wind data at 100 m above the sampling site and the wind data from 12 monitoring stations at ground level (~15m) to indicate the different scales of motions. The winds at the surface monitoring stations were expected to be more sensitive to local-scale turbulence and convection than the winds at 100 m. With less influence from the surface forces, the indicators at 100 m would be more sensitive to larger scales of motion. The equations used as follows:

$$L_{n\tau/bj} = T\left[\left(\sum_{j=i}^{i-\tau+1} u_i\right)^2 + \left(\sum_{j=i}^{i-\tau+1} v_i\right)^2\right]^{1/2} \qquad (11)$$

$$S_{n\tau/bj} = \sum_{j=i}^{i-\tau+1}({u_j}^2 + {v_j}^2)^{1/2} \qquad (12)$$

$$R_{n\tau/bj} = 1 - \frac{L_{i\tau}}{S_{i\tau}} \qquad (13)$$

where T is the interval of the data (i.e., 60 min), i is the i^{th} the ending time step data, τ is the integration time period of the wind run (24 h), i-τ+1 represents the data at the start time, and n is the number of monitoring stations (a total of 12 in this study). The quantities u and v are the wind vectors. Using the wind data from the 12 monitoring stations covering Baoji, the L and S values at the 12 different sites at ground level were calculated. $L_{n\tau}$ and $S_{n\tau}$ represent the resultant transport distance and the actual wind run distance at the n^{th} (n = 1 to 12) monitoring station at ground level; $R_{n\tau}$ is the recirculation factor at the n^{th} monitoring station which is calculated based on $L_{n\tau}$; and $S_{n\tau}$; L_{bj}, and S_{bj} are the resultant transport distance and the actual wind run distance at 100 m height above the ground. These represent the flow characteristics in higher atmosphere at the study site, and they were calculated by using the wind data at 100 m height. The recirculation factor (R_{bj}) was calculated for a height of 100 m.

As explained in Levy et al., (2010), if local-scale motions are strong and regional-scale motions are weak, the variations in winds at each station would not be likely to be uniform due to differences in local factors, and that would result in relatively large standard deviations (R_{std}) for $R_{n\tau}$. By contrast, if the local-scale motions are weak and the regional-scale motion is strong, the wind direction would be likely to be more uniform over a large area, and the R_{bj} and the R_{std} should be relatively smaller.

2.6 Self-organizing map

A self-organizing map (SOM) developed by Kohonen (1990) is a type of artificial neural network that is widely used for categorizing high-dimensional data into a few major features (Stauffer et al., 2016 and Pearce et al., 2014). In particular, this approach is widely used for categorizing different meteorological patterns (Liao et al., 2020; Han et al., 2020; Jiang et al., 2017). Unlike traditional dimension reduction methods (e.g., principal component analysis), SOM projects high-dimensional input data by non-linear projection into user-designed lower-dimensions, which are typically two-dimensional arrays of nodes (Hewitson and Crane, 2006). The performance of SOM in classifying climatological data has been shown to be robust (Reusch et al., 2005). Competitive learning algorithms are used to train SOM, and the architecture of SOM consists of two layers; one is called the input layer and it contains the high dimensional input data. The other layer is the output layer in which the node number is the output cluster number. The working principle of SOM is to convert high dimensional data with complex correlations into lower dimensions via geometrical relationships (Ramachandran et al., 2019). After the initial random weights are generated, the input data are compared with each weight, and the best match is defined as winning. The winning node and the neighboring nodes close to the winning node will learn from the same inputs and the associated weights are updated. After multiple iterations, the network to settles into stable zones of features and the weights.

More detailed working principles of SOM can be found Kangas and Kohonen, (1996) and Kohonen et al., (1996).

Comparison between the input data and each weight is made by applying Euclidean distances, the best match is defined by the following equation:

$$\|x - m_c\| = min\{\|x - m_i\|\} \tag{14}$$

where x is the input data, m_c is the best matched weight, m_i is the weights connected with the *i*th node.

The weights are updated by following equation:

$$m_i(t+1) = m_i(t) + h_{ci}(t)[x(t) - m_i(t)] \tag{15}$$

where the $m_i(t+1)$ is the *i*th weight at t+1 time, $m_i(t)$ is the *i*th weight at t time, the $h_{ci}(t)$ is the neighborhood kernel defined over the lattice points at t time, and *c* is the winning node location.

SOM was used to categorize the daily atmospheric motions during the study period and to explore the influences of different scales of motion on source-specific eBC. Hourly averages of three sets of data (R_{std}, L_{bj}, and S_{bj}) were input into SOM. Determining the size of the output map is crucial for SOM (Chang et al 2020 and Liu et al., 2021). To reduce the subjectivity, the K-means cluster method was used for the decision-making regarding size. The similarity of each item of the input data relative to the node was measured using Euclidean distance. The iteration number was set to 2000. For each input data item, the node closest to it would “win out”. The reference vectors of the winning node and their neighborhood nodes were updated and adjusted towards the data. The “Kohonen” package in *R* language (Wehrens and Kruisselbrink, 2019) was used to develop the SOM model in this study.

2.7 Estimations of direct radiative effects and heating rate

The Santa Barbara DISORT Atmospheric Radiative Transfer (SBDART) model was used to estimate the direct radiative effects (DRE) induced by source-specific eBC. The model has been used in many studies to calculate the DRE caused by aerosols and BC (Pathak et al., 2010; Rajesh et al., 2018; Zhao et al., 2019). SBDART calculated DRE based on several well-tested physical models. Details regarding the model were presented in Ricchiazzi et al., (1998). The important input data included aerosol parameters, including aerosol optical depth (AOD), single scattering albedo (SSA), asymmetric factor (AF) and extinction efficiency, surface albedo, and atmospheric profile.

The aerosol parameters used in this study were derived by the Optical Property of Aerosol and Cloud (OPAC) model (Hess et al., 1998) based on the number concentrations of aerosol components. As the study was conducted in an urban region, the urban aerosol profile was used in OPAC, and it included soot (eBC), water-soluble matter (WS), and water-insoluble matter (WIS). The number concentrations of soot were derived from the mass concentrations of eBC with the default ratio (5.99E-5 μg m^{-3}/ particle.cm^{-3}) in OPAC. The number concentrations of WS and WIS were adjusted until the modeled SSA and b_{abs} at 500nm in OPAC were close (±5%, see Figure S4) to those values calculated with data from the nephelometer and AE33 ($b_{ext}(520) = b_{scat}(525) + b_{abs}(520)$, SSA= $b_{scat}(525)/b_{ext}(520)$). The DRE of source-specific eBC at the top of atmosphere (TOA) and surface atmosphere (SUF) were calculated from the difference between the DREs with or without the number concentrations of the source-specific eBC under clear-sky conditions.

$$DRE_{eBC} = (F\downarrow - F\uparrow)_{with\ eBC} - (F\downarrow - F\uparrow)_{without\ eBC} \tag{16}$$

$$DRE_{eBC,ATM} = DRE_{eBC,TOA} - DRE_{eBC,SUF} \tag{17}$$

where DRE_{eBC} is the DRE of source-specific eBC, $F\downarrow$ and $F\uparrow$ are the downward and upward flux, $DRE_{eBC,ATM}$ is the DRE of the source-specific eBC for the atmospheric column, that is, the DRE at the top of the atmosphere ($DRE_{eBC,TOA}$) minus that at the surface ($DRE_{eBC,SUF}$)"

"Text S1. Minimum R - squared method

The minimum R squared method developed by Wu et al., (2016) was used to separate secondary organic carbon (SOC) from the primary organic carbon (POC). The assumption behind this method is the organic carbon (OC) from non-combustion source is negligible. As explained by Wang et al., (2019), the major non-combustion source is biogenic which is mainly exists in coarse mode. Thus, the non-combustion organic carbon is considered negligible in this study. Therefore, SOC and POC can be separated by using following equations. For each date set, the ratios of OC to eBC and SOC and the R^2 between eBC and SOC can be calculated. SOC and eBC are considered independent, so the (OC/eBC)pri should be the value obtained when the R^2 between eBC and SOC is minimum.

$$\mathrm{POC} = (\mathrm{OC}/\mathrm{EC})_{\mathrm{pri}} \times \mathrm{EC} \tag{S1}$$

$$\mathrm{SOC} = \mathrm{OC}_{\mathrm{total}} - (\mathrm{OC}/\mathrm{EC})_{\mathrm{pri}} \times \mathrm{EC} \tag{S2}$$

where EC in this study is eBC. The $(\mathrm{OC/EC})_{\mathrm{pri}}$ is the ratio in freshly emitted OC and EC from combustion sources.

The light absorption at shorter wavelengths (<660nm) is not only from primary light absorbing substances but also from the secondary organic carbon (Wang et al., 2019). The assumption for this method is that the light absorption caused by non-combustion sources is negligible. As mentioned above, most of the biogenic BrC is in coarse mode. Another common light absorbing substance is the Fe_2O_3 in the dust, but the impact of that should be limited because the absorption from Fe_2O_3 in the dust has been reported to be much smaller than that from BC (Ramachandran and Kedia, 2010). Thus, to separate the secondary light absorption ($b_{\mathrm{abs}}(\lambda)_{\mathrm{secondary}}$) from the primary light absorption ($b_{\mathrm{abs}}(\lambda)_{\mathrm{primary}}$), a BC-tracer method coupled with a minimum R-squared method was used. The equations used for the calculation are follows:

$$b_{\mathrm{abs}}(\lambda)_{\mathrm{secondary}} = b_{\mathrm{abs}}(\lambda) - \left(\frac{b_{\mathrm{abs}}(\lambda)}{\mathrm{BC}}\right)_{\mathrm{pri}} \times \mathrm{BC} \tag{S3}$$

$$b_{\mathrm{abs}}(\lambda)_{\mathrm{primary}} = b_{\mathrm{abs}}(\lambda) - b_{\mathrm{abs}}(\lambda)_{\mathrm{secondary}} \tag{S4}$$

Where $b_{\mathrm{abs}}(\lambda)$ is the light absorption at different wavelengths (λ=370nm, 470nm, 520nm, 590nm, 660nm) measured by AE33, BC is the eBC measured by AE33 at a wavelength of 880nm. The $\left(\frac{b_{\mathrm{abs}}(\lambda)}{\mathrm{BC}}\right)_{\mathrm{pri}}$ is the ratio of the primary light absorption to the BC mas concentration from combustion sources.

Text S2. Cluster analysis of air-mass trajectories

Back trajectories were calculated by using Hybrid Single-Particle Lagrangian Integrated Trajectory (HYSPLIT) model (Draxler and Hess, 1998) developed by the Air Resource Lab (ARL) of the National Oceanic and Atmospheric Administration (NOAA). The model can predict the position of air mass by using mean wind. The back-in-time positions are calculated by reversing the advection equation (Draxler and Hess, 1997). The calculation requires the mean wind, for calculating trajectories, only advection is considered (Stein et al., 2015). The basic equations for trajectory calculation in HYSPLIT are as follows:

$$P'(t+\Delta t) = P(t) + V(P,t) \times \Delta t \quad \text{(S5)}$$

$$P(t+\Delta t) = P(t) + 0.5 \times [V(P,t) + V\left(P', t+\Delta t\right)] \times \Delta t \quad \text{(S6)}$$

Where $P(t)$ is the initial position, $P'(t+\Delta t)$ is the first guess position, V is the average velocity, t is the time, Δt is the time step.

A large number of 24 h trajectories (793) that were retrieved for the study period showed diverse pathways, so in order to find out the representative pathways for those trajectories, a cluster analysis based on an angle-based distance statistics method was conducted. Compared with Euclidean distance, angle-based distance statistics method focuses on the direction of air mass instead of the speed. The angle-based distance statistics method is defined by following equations (Sirois and Bottenheim, 1995):

$$d_{12} = \frac{1}{2}\sum_{i=1}^{n} cos^{-1}(0.5 \times \frac{A_i+B_i-C_i}{\sqrt{A_iB_i}}) \quad \text{(S7)}$$

$$A_i = (X_1(i) - X_0)^2 + (Y_1(i) - Y_0)^2 \quad \text{(S8)}$$

$$B_i = (X_2(i) - X_0)^2 + (Y_2(i) - Y_0)^2 \quad \text{(S9)}$$

$$C_i = (X_2(i) - X_1(i))^2 + (Y_2(i) - Y_1(i))^2 \quad \text{(S10)}$$

Where d_{12} is the average angle between the two backward trajectories, varying between 0 and π; X_0 and Y_0 are the position of the receptor site; and X_1 (Y_1) and X_2 (Y_2) are the backward trajectories 1 and 2, respectively. In this study, three clusters were chosen as representative of the backward trajectory clusters based on the total spatial variance (TSV) value. The simulation was conducted using the GIS-based TrajStat software (Wang et al., 2009)."

Specific comments

Abstract:

"Black carbon (BC) has a strong light absorption ability and is known as the second strongest light-absorbing substance in the atmosphere after CO2" This is debatable.

Response: We have corrected the sentence into "Black carbon (BC) is one of the most important short lived climate forcers, and atmospheric motions play an important role in determining its mass concentrations of pollutants."

In the first paragraph in the introduction part, we also revise the relevant sentence into:

"Black carbon (BC) is produced by the incomplete combustion of biomass and fossil fuels. The BC aerosol has a strong light absorption capacity and can cause heating of the atmosphere. In fact, BC is widely recognized as one of the most important short-lived climate forcers (IPCC, 2021)."

What does model refer to in "aethalometer model"?

Response: The model refers to the calculation model based on Beer–Lambert's Law. The model contains a few equations relating the absorption coefficients (b_{abs}), the wavelengths, and the absorption exponents for conditions of two BC emission sources (Sandradewi et. al., 2008). In this study the two sources were fossil combustion and biomass burning. We have revised the method section 2.4 to provide a better description and reference. The revised version was provided in response above.

Reference:

Sandradewi, J., Prévôt, A. S. H., Weingartner, E., Schmidhauser, R., Gysel, M., and Baltensperger, U.: A study of wood burning and traffic aerosols in an Alpine valley using a multi-wavelength Aethalometer, Atmos. Environ., 42, 101-112, https://doi.org/10.1016/j.atmosenv.2007.09.034, 2008.

"chemical data and optical data" what kind of data?

Response: The chemical data includes EC, POC, K^+, Mg, Al, Si, S, Cl, Ca, V, Mn, Fe, Ni, Cu, As, Se, Br, Sr, Pb, Ga, and Zn. The optical data refers to primary absorption coefficient (b_{abs} (λ)) at six wavelengths (λ = 370, 470, 520, 590, 660, and 880 nm). To make this clear, we have revised the relevant sentence into

"Equivalent BC (eBC) source apportionment was based on an aethalometer model with the site-dependent absorption Ångström exponents (AAEs) and the mass absorption cross-sections (MACs) retrieved using a positive matrix factorization (PMF) model based on observed chemical components (i.e. EC, POC, K^+, Mg, Al, Si, S, Cl, Ca, V, Mn, Fe, Ni, Cu, As, Se, Br, Sr, Pb, Ga, and Zn) and primary absorption coefficients at selected wavelengths from λ = 370 to 880nm."

"The derived AAEs" over what wavelength range?

Response: The AAEs were obtained by the power fit of b_{abs} from 370nm, 470nm, 520nm, 660nm and 880nm. The fitting is shown in figure R3. We also added this figure into supplement material and revised the relevant sentence shown below:

"The derived AAEs from 370 to 880nm were 1.07 for diesel vehicular emissions, 2.13 for biomass burning, 1.74 for coal combustion, and 1.78 for mineral dust. The mean values for eBC_{fossil} and $eBC_{biomass}$ were 2.46 µg $m^{-3}$and 1.17 µg m^{-3} respectively."

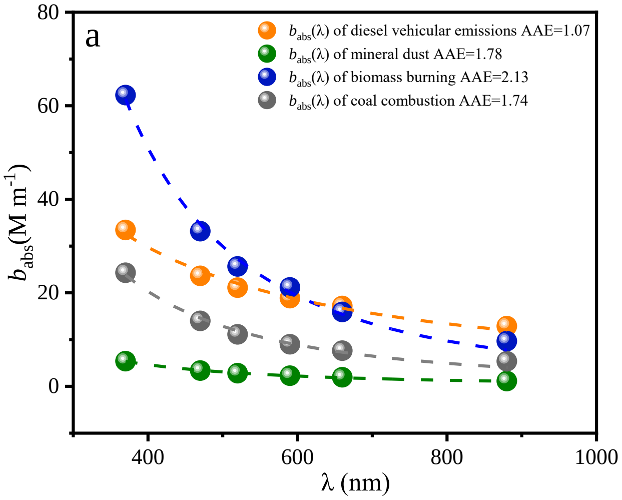

Figure R3 Light absorption ($b_{abs}(\lambda)$) for diesel vehicular emissions, biomass burning, coal combustion, and mineral dust. The dashed lines are the power law fits.

"four featured atmospheric motions categories" what the four categories are remains a mystery until later, please provide a brief description here because the abstract should be self-contained.

Response: Thanks for the suggestion, we have revised this sentence to add more information on the four categories as follows:

"Wind run distances and the vector displacements of the wind in 24 h were used to construct a self-organizing map, from which four atmospheric motions categories were identified (local-scale dominant, local-scale strong and regional-scale weak, local-scale weak and regional-scale strong and regional-scale dominant)."

"The trajectory clusters" what trajectories? How were those determined?

Response: The trajectories in this study reconstruct the path the air mass moved through in time and space. The back trajectories were calculated by using Hybrid Single-Particle Lagrangian Integrated Trajectory (HYSPLIT) model (Draxler and Hess, 1998). The model can predict the position of air mass by using the mean winds. The backwards-in-time position is calculated by reversing the advection equation (Draxler and Hess, 1997). The calculation needs the mean wind, for running trajectories, and only advection is considered (Stein et al., 2015). The basic equations for trajectory calculation in HYSPLIT are as followings:

$$P'(t+\Delta t) = P(t) + V(P,t) \times \Delta t \tag{R1}$$

$$P(t+\Delta t) = P(t) + 0.5 \times [V(P,t) + V(P',t+\Delta t)] \times \Delta t \tag{R2}$$

Where $P(t)$ is the initial position, $P'(t+\Delta t)$ is the first guess position, V is the average velocity, t is the time, Δt is the time step.

To this clear, we have revised the sentence into "Cluster analysis for the back trajectories of air mass calculated by Hybrid Single-Particle Lagrangian Integrated Trajectory model at the study site indicated that the directions of air flow can have different impacts for different scales of motion." And added the method description above into the supplementary material (Text S2) and provided a Table (Table S2) to show the input data, main parameters used in this study as follow:

Table R3 Data and parameters used in HYSPLIT model

Items	Data/parameters
Model	HYSPLIT
Meteorological data	GDAS data, 1° × 1°, 23 vertical levels, 3 hourly
Backward period	24h
Footprint level	100 m above the ground
Receptor site location	34°21′16.8″N, 107°12′59.6″E

Reference:

Stein, A., Draxler, R., Rolph, G., Stunder, B., Cohen, M., and Ngan, F.,: NOAA'S HYSPLIT Atmospheric Transport and Dispersion Modeling System, Bull. Amer. Meteor. Soc., 96, 2059-2077, https://doi.org/10.1175/BAMS-D-14-00110.1, 2015.

Draxler, R., and Hess, G.: An overview of the HYSPLIT_4 modelling system for trajectories, Aust. Meteorol. Mag., 47, 1998.

Lines 30-31: I don't understand the sentence "This study revealed the disproportional change between BC mass concentration and its DRE."

Response: We apologize for the confusing expression, and we would like to provide a further explanation and have revised the sentence to make it clear.

If the light absorbing ability is independent of the patterns of the motion (which indicates a possible path and distance the BC moved in atmosphere), the value of DRE per unit mass of BC should be the same for all cases. However, in this study, both DREs and the mass concentrations of eBC_{fossil} and $eBC_{biomass}$ changed. If we normalize DRE by dividing the mass concentration of eBC, we can see that a unit of eBC of both types associated with higher DRE under local scale weak and regional scale strong motion (LWRS) and regional scale dominance motion (RD) as shown in Table R4. If we take local scale dominance (LD) as a reference case to calculate the difference between averaged BC mass concentration (or averaged DRE) under LD and other cases (LSTW, LWRS and RD). It is apparent that the BC mass concentrations decreased more than DRE did (Table R5).

To avoid confusion, we revised the sentence into "The finding that the DRE efficiency of BC increased during the regional transport suggested significant consequences in regions downwind of pollution sources and emphasizes the importance of regionally transported BC for potential climatic effects." And "Similar to the mass concentrations, the DREs of the two types of eBC were both lower when the regional scale of motions were greater than the local ones. However, the changes in mass concentrations and DREs were not proportionate because the regional-scale of motions carried the fresh BC away from the local site but brought the aged BCs to the site from the upwind regions. As a result, the DRE efficiency of eBC was ~1.5 times higher when the regional scale of motion was stronger."

Table R4. Direct radiative forcing efficiencies for equivalent black carbon (eBC) from fossil fuel combustion (eBCfossil) and the eBC from biomass burning

Atmospheric motion category	$DRE_{eBCfossil, ATM}$ efficiency[a] $((W\ m^{-2})/(\mu g\ m^{-3}))$	$DRE_{eBCbiomass, ATM}$ efficiency[a] $((W\ m^{-2})/(\mu g\ m^{-3}))$
Local scale dominance (LD)	10.2 ± 4.2	10.3 ± 4.4
Local scale strong and regional scale weak (LSRW)	10.6 ±5.7	10.2 ± 5.8
Local scale weak and regional scale strong (LWRS)	13.5 ± 6.7	14.7 ± 8.1
Regional scale dominance (RD)	15.6 ± 8.9	15.5 ± 8.4

a: Mean ± Std

Table R5 The change of mass concentration of different eBCs and their DREs

Atmospheric motion category	Change of mass concentration of eBC_{fossil}	Change of mass concentration of $eBC_{biomass}$	Change of $DRE_{eBCfossil, ATM}$	Change of $DRE_{eBCbiomass, ATM}$
LD	-	-	-	-
LSRW	9.4%	30.3%	5.7%	-2.9%
LWRS	30.2%	43.4%	29.3%	23.1%
RS	45.1%	38.8%	34.6%	29.0%

Line 32: "It highlights…" what does "it" refer to? In general, this closing sentence reads awkward, and I would suggest rewording it.

Response: Thanks for pointing this out, we have revised the sentence as follows:

"The finding that the DRE efficiency of BC increased during the regional transport suggested significant consequences in regions downwind of pollution sources and emphasizes the importance of regionally transported BC for potential climatic effects."

Introduction:

Light absorbing or agent with positive radiative forcing? The two whings are linked but not the same.

Response: We agree with reviewer. Based on IPCC (2021) and most studies on BC (Zhao, et al., 2019; Panicker et al., 2010; Rajesh and Ramachandran, 2018, Valenzuela et al., 2017) direct radiative forcing, BC generally is considered to be a short life climate forcer which can warm the climate, however for other types of aerosols, their scattering ability is higher than its absorbing ability which more likely leads to negative forcings.

We have revised the sentence into:

"Black carbon (BC) is produced by the incomplete combustion of biomass and fossil fuels. The BC aerosol has a strong light absorption capacity and can cause heating of the atmosphere. In fact, BC is widely recognized as one of the most important short-lived climate forcers (IPCC, 2021)."

Reference:

IPCC: Climate Change 2021: The Physical Science Basis. Contribution of Working Group I to the Sixth Assessment Report of the Intergovernmental Panel on Climate Change [Masson-Delmotte, V., P. Zhai, A. Pirani, S.L. Connors, C. Péan, S. Berger, N. Caud, Y. Chen, L. Goldfarb, M.I. Gomis, M. (eds)], https://reliefweb.int/report/world/climate-change-2021-physical-science-basis, 2021

Zhao, S. P., Yu, Y., Yin, D., Yu, Z., Dong, L. X., Mao, Z., He, J. J., Yang, J., Li, P., and Qin, D. H.: Concentrations, optical and radiative properties of carbonaceous aerosols over urban Lanzhou, a typical valley city: Results from in-situ observations and numerical model, Atmos. Environ., 213, 470–484, https://doi.org/10.1016/j.atmosenv.2019.06.046, 2019.

Panicker, A. S., Pandithurai, G., Safai, P. D., Dipu, S., and Lee, D.-I.: On the contribution of black carbon to the composite aerosol radiative forcing over an urban environment, Atmos. Environ., 44, 3066-3070,

10.1016/j.atmosenv.2010.04.047, 2010.

Rajesh, T. A., and Ramachandran, S.: Black carbon aerosols over urban and high altitude remote regions: Characteristics and radiative implications, Atmos. Environ., 194, 110-122, https://doi.org/10.1016/j.atmosenv.2018.09.023, 2018.

Valenzuela, A., Arola, A., Anon, M., Quirantes, A., Alados-Arboledas, L.: Black carbon radiative forcing derived from AERONET measurements and models over an urban location in the southeastern Iberian Peninsula, Atmospheric Research, 191, 44–56, http://dx.doi.org/10.1016/j.atmosres.2017.03.007, 2017.

Line 55: remove “at” before “to”
Response: Thanks for the correction, we have revised this sentence. Now the sentence is:

“The concentrations of BC are controlled by local emissions and regional transport, but meteorological conditions also are important because they affect both transport and removal. Normally, local emissions in urban areas are predictable to some degree because those emission sources are mainly anthropogenic and the concentrations of pollutants follow the diurnal patterns driven by anthropogenic activities.”

Line 57: multiply -> multiple
Response: We apologize for the misspelling. It has been corrected in the revised version.

“By contrast, meteorological conditions and regional transport are governed by multiple scales of motion which result in distinct meteorological impacts on ambient pollutant levels (Levy et al., 2010, Dutton, 1976).”

Line 62: Why the aerosol concentration controls the local scale motion?
Response: Horizontal temperature variations can give rise to pressure differences, which can result in atmospheric motions (Oke, 1988). The aerosol concentrations and types (i.e. dominance of scattering aerosol or absorbing aerosol) can impact on the temperature, and changes in cloud microphysical properties also can impact the temperature (IPCC, 2021). Thus, difference of aerosol mass concentrations between locations could lead to atmospheric motions.

Reference:

Oke, T., Boundary Layer Climates, 2nd edition, Taylor & Francis e-Library, 2002.

IPCC: Climate Change 2021: The Physical Science Basis. Contribution of Working Group I to the Sixth Assessment Report of the Intergovernmental Panel on Climate Change [Masson-Delmotte, V., P. Zhai, A. Pirani, S.L. Connors, C. Péan, S. Berger, N. Caud, Y. Chen, L. Goldfarb, M.I. Gomis, M. (eds)], https://reliefweb.int/report/world/climate-change-2021-physical-science-basis, 2021

Line 64: diffuse -> disperse?
Response: Thanks for the comment, we have corrected this.
“Larger scale of motions are associated with a mesoscale or synoptic scale weather systems, which on the one hand can transport pollutants but on the other can disperse them (Kalthoff et al., 2000; Zhang et al., 2012).”

Line 65: “decides” seems more to belong to an intelligent entity. Maybe “determines”
Response: Thanks for explaining the difference between the two words. We have changed the “decides” into

“determines”.

“The relationships between atmospheric motions and pollutant concentrations are complex. Atmospheric motions determine where and how extensive the pollution impacts are, but of course the rates of pollutant emissions, especially local ones, are important, too (Dutton, 1976).”

Line 72: “river valley city” comes a bit out of the blue here, it might be good to provide a sentence with some background, like the general location, etc., even if that’s then discussed in detail in the method section. Is the city specifically Baoji?
Response: We agree that providing some background information would make it is more coherent, so we rewrote this part as follows:

“Topography also plays an important role in air pollution (Zhao et al., 2015). River-valley topography is complicated, and it can have a considerable influence on air pollution and synoptic patterns of flow (Green et al., 2016; Carvalho et al., 2006). The pollution levels at cities in river-valleys are not only influenced by general atmospheric dynamics but also strongly impacted by the local-scale of dynamics (Brulfert et al., 2006). Surface albedo and surface roughness are affected by the complex topography of river-valley regions, and those physical factors can affect circulation causing changes in pollutant mass concentrations (Wei et al., 2020). Mountains also significantly affect pollution, and once pollutants are generated or transported into the river-valley regions, their dispersal can be impeded by the blocking effect of the mountains. Instead of being dispersed, they can be carried by the airflows over the mountains to converge at the bottom of the valley and increase the pollutants along the river (Zhao et al., 2015). In this way, pollutants can accumulate in valleys and spread throughout the area, thereby aggravating pollution. In addition, temperature inversions commonly form in river-valleys during the winter, and that, too, can aggravate pollution problems (Glojek et al., 2022 and Bei et al., 2016).”

The river valley city we referred here is not just baoji. This topography (river-valley) has been found impact on air pollution and synoptic patterns in other countries as well (Brulfert et al., 2006, Green et al., 2016, Glojek et al., 2022).

Reference

Glojek, K., Moˇcnik, G., Alas, H., Cuesta-Mosquera, A., Drinovec, L., Gregoriˇc, A., Ogrin, M., Ježek, I., Müller, T., Rigler, M., Remškar, M., Pinxteren, D., Herrmann, H., Ristorini, M., Merkel, M., Markelj, M., Wiedensohler, A.: The impact of temperature inversions on black carbon and particle mass concentrations in a mountainous area, Atmos. Chem. Phys., 22, 5577–5601, https://doi.org/10.5194/acp-22-5577-2022, 2022.

Brulfert, G., Chemel, C., Chaxel, E., Chollet, J., Jouve, B., and Villard, H.: Assessment of 2010 air quality in two Alpine valleys from modelling: Weather type and emission scenarios, Atmos. Environ., 40, 7893–7907, https://doi.org/10.1016/j.atmosenv.2006.07.021, 2006.

Green, M., Chow, J., and Watson, G.: Effects of Snow Cover and Atmospheric Stability on Winter PM2.5 Concentrations in Western U.S. Valleys, Journal of Applied Meteorology and Climatology., 54, https://doi.org/doi: 10.1175/JAMC-D-14-0191.1, 2016.

Line 75: why the albedo makes the solar radiation uneven? Do they mean the reflected radiation? In general, I find this sentence awkward and unclear.
Response: Surface albedo is the ratio of up-welling to down-welling short wave radiative flux at the surface ($Albedo = \frac{Reflected\ radiation}{Incident\ radiation}$). Surface albedo is one of the most important parameters for determining radiative

forcing and it impacts on climatic processes. The spatial and temporal distribution of surface properties captured by albedo reflect a variety of natural and human influences on the surface that are of importance in terms of radiative balance. Surface albedos vary with the type of surface; for example the albedo for the ocean is much lower than that of land (Satheesh et al., 2006), the surface albedo of vegetated lands is also different from that of urban areas. Studies found that lower surface albedos, compared with higher ones, result in more positive radiative forcing at the top of the atmosphere (Nari et al., 2013 and reference therein).

We have rewritten that sentence from line 75 as following and hope it now reads clear and understandable.

“Surface albedo and surface roughness are affected by the complex topography of river-valley regions, and those physical factors can affect circulation causing changes in pollutant mass concentrations (Wei et al., 2020).”

The sentence starting on line 77 is also awkward and should be reworded.
Response: We have revised this sentence, now it reads like:

“Mountains also significantly affect pollution, and once pollutants are generated or transported into the river-valley regions, their dispersal can be impeded by the blocking effect of the mountains. Instead of being dispersed, they can be carried by the airflows over the mountains to converge at the bottom of the valley and increase the pollutants along the river (Zhao et al., 2015).”

Line 80: eBC appears here without having been defined as equivalent BC. It has been defined only later, but it should be defined at its first appearance.
Response: Thanks for pointing this out. We have added the definition of eBC here and deleted the one appeared later. Now it is:

“Thus, we focused our study on the impacts of different scales of motion on source-specific equivalent BCs (eBCs), and we evaluated radiative effects of eBCs over a river-valley city.”

Line 81: I believe the authors meant: “the contributions of fossil fuel combustion and biomass burning to eBC concentrations”
Response: Yes, that is what we mean. Thanks for the comment, we have revised this sentence into

“The primary objectives of this study were: (1) to quantify the contributions of fossil fuel combustion and biomass burning to eBC concentrations, (2) to investigate the impacts of different scales of motion on the source-specific eBC, and (3) to estimate the radiative effects and the radiative efficiency of the source-specific eBC under different atmospheric motion scenarios.”

Method:

Line 88: Guanzhong Plain is where the river-valley city of Baoji is located, I guess? It would be nice to say so right at the beginning.
Response: We have revised this sentence to make that point clear. The revised paragraph can be seen in a response above to the general comments.

Section 2.1: a map of the region I think would help as figure 1.
Response: We have updated the map of the region in supplementary materials. The new map looks like:

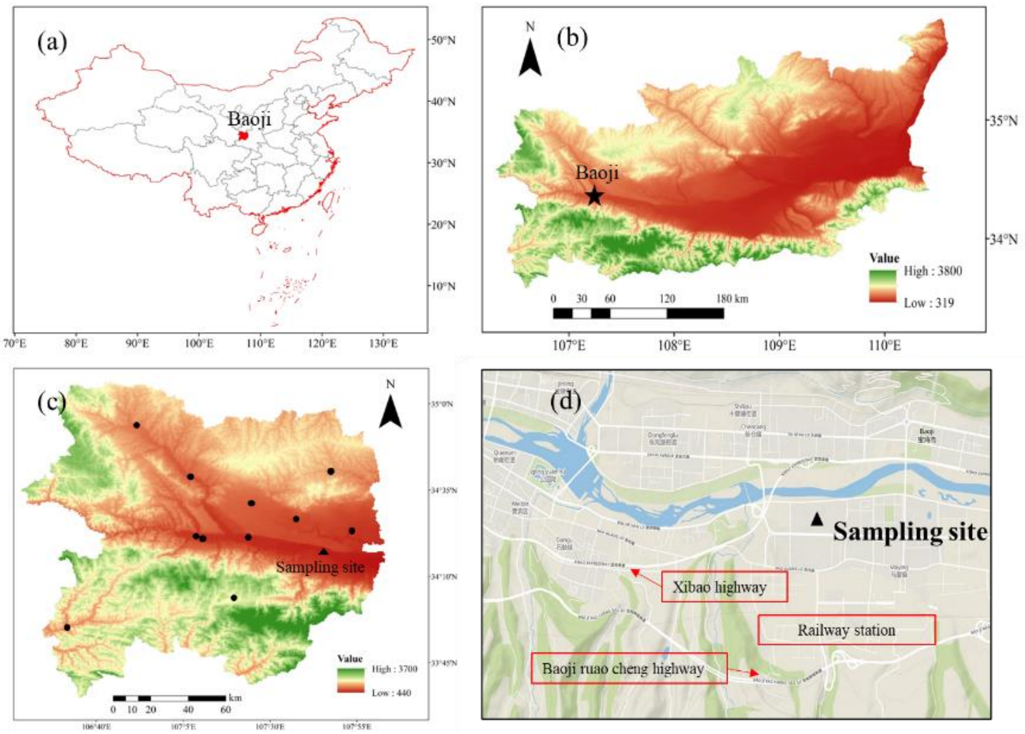

Figure R4. A map of the research site; (a) map of China—the red shape is the location of Baoji, (b) a map of the Guanzhong Plain, the black star represents the location of Baoji; (c) a map of Baoji City, the black dots and the black triangle represent 12 stations and the triangle is the location of sampling site, (d) a map of the sampling site.

Line 94: dense population, provide some numbers such as the total population, and population density.
Response: We have added the total population (0.341 million with 63.5% population living in downtown aera) and population density (6003 people per km^2 in 2019) in the site description. The revised paragraph can be seen in the response above in the general comments.

Section 2.5 is quite confusing.
Response: We have revised this section and added more detailed explanations of the equation variables and had it edited by a native speaker for clarity. Now the section 2.5 reads:

"**2.5 Indicators for the different scales of motion**

The mathematical definitions of airflow condition proposed by Allwine and Whiteman (1994) were used in this study. The definitions quantify the flow features integrally at individual stations. Three variables were quantified, namely the actual wind run distance (S) which is the scalar displacement of the wind in 24 h (i.e. the accumulated distance of the wind), the resultant transport distance (L) which is the vector displacement of the wind in 24 h (i.e. the straight line from the starting point to the end point), and the recirculation factor (R) is based on the ratio of L and S which indicates the frequency of the wind veering in 24 h. The influences of different scales of atmospheric motions were assessed based on the method proposed by Levy et al., (2010), and for this, we used wind data at 100 m above the sampling site and the wind data from 12 monitoring stations at ground level (~15m) to indicate the different scales of motions. The winds at the surface monitoring stations were expected to be more sensitive to local-scale turbulence and convection than the winds at 100 m. With less influence from the surface forces, the indicators at 100 m would be more sensitive to larger scales of motion. The equations used as follows:

$$L_{n\tau/bj} = T\left[\left(\sum_{j=i}^{i-\tau+1} u_i\right)^2 + \left(\sum_{j=i}^{i-\tau+1} v_i\right)^2\right]^{1/2} \quad (11)$$

$$S_{n\tau/bj} = \sum_{j=i}^{i-\tau+1} ({u_j}^2 + {v_j}^2)^{1/2} \quad (12)$$

$$R_{n\tau/bj} = 1 - \frac{L_{i\tau}}{S_{i\tau}} \quad (13)$$

where T is the interval of the data (i.e., 60 min), i is the i^{th} the ending time step data, τ is the integration time period of the wind run (24 h), i-τ+1 represents the data at the start time, and n is the number of monitoring stations (a total of 12 in this study). The quantities u and v are the wind vectors. Using the wind data from the 12 monitoring stations covering Baoji, the L and S values at the 12 different sites at ground level were calculated. $L_{n\tau}$ and $S_{n\tau}$ represent the resultant transport distance and the actual wind run distance at the n^{th} (n = 1 to 12) monitoring station at ground level; $R_{n\tau}$ is the recirculation factor at the n^{th} monitoring station which is calculated based on $L_{n\tau}$; and $S_{n\tau}$; L_{bj}, and S_{bj} are the resultant transport distance and the actual wind run distance at 100 m height above the ground. These represent the flow characteristics in higher atmosphere at the study site, and they were calculated by using the wind data at 100 m height. The recirculation factor (R_{bj}) was calculated for a height of 100 m.

As explained in Levy et al., (2010), if local-scale motions are strong and regional-scale motions are weak, the variations in winds at each station would not be likely to be uniform due to differences in local factors, and that would result in relatively large standard deviations (R_{std}) for $R_{n\tau}$. By contrast, if the local-scale motions are weak and the regional-scale motion is strong, the wind direction would be likely to be more uniform over a large area, and the R_{bj} and the R_{std} should be relatively smaller."

Line 175: A ratio indicates a difference? That is confusing. Also, R is defined in 13 not as the ratio of L and S but as the ratio of the difference between S and L and S itself. Or is this a different R?
Response: We apologize for the inaccurate expression. The "R" on line 175 is the R defined in equation 13. We have corrected the description of the R in line 175. Now it consistent with the equation 13:

"Three variables were quantified, namely the actual wind run distance (S) which is the scalar displacement of the wind in 24 h (i.e. the accumulated distance of the wind), the resultant transport distance (L) which is the vector displacement of the wind in 24 h (i.e. the straight line from the starting point to the end point), and the recirculation factor (R) is based on the ratio of L and S which indicates the frequency of the wind veering in 24 h."

Line 189: Again, if equation 13 is correct, then R is not the ratio of L to S but 1 – the ratio of L to S. Same for line 191 (which seems a repetition anyway).
Response: As noted above, we have corrected the expression that was on line 189 and 190, now it reads like:

"$R_{n\tau}$ is the recirculation factor at the n^{th} monitoring station which is calculated based on $L_{n\tau}$ and $S_{n\tau}$; L_{bj}, and S_{bj} are the resultant transport distance and the actual wind run distance at 100 m height above the ground. These represent the flow characteristics in higher atmosphere at the study site, and they were calculated by using the wind data at 100 m height. The recirculation factor (R_{bj}) was calculated for a height of 100 m."

Lines 192-193: this seems a bit of a circular argument (a tautology).
Response: We have rewritten this paragraph as follows:

“As explained in Levy et al., (2010), if local-scale motions are strong and regional-scale motions are weak, the variations in winds at each station would not be likely to be uniform due to differences in local factors, and that would result in relatively large standard deviations (R_{std}) for $R_{n\tau}$. By contrast, if the local-scale motions are weak and the regional-scale motions are strong, the wind direction would be likely to be more uniform over a large area, and the R_{bj} and the R_{std} should be relatively smaller.”

Line 207: provide a citation.
Response: We have provided the citation as following:

“Determining the size of the output map is crucial for SOM (Chang et al 2020 and Liu et al., 2021).”

Results and discussion:

Line 261: contain -> include
Response: Thanks for the correction, we have changed the word:

“The important input data included aerosol parameters, including aerosol optical depth (AOD), single scattering albedo (SSA), asymmetric factor (AF) and extinction efficiency, surface albedo, and atmospheric profile.”

Line 222: what is the default ratio in the model? And what model? OPAC?
Response: Yes, the model is OPAC. The default ratio used for converting mass concentration of BC to its number concentration is 5.99E-5 (μg m^{-3}/ part.cm^{-3}) in OPAC. To make this clear, we have added this information into the sentence to make it clear:

“The number concentrations of soot were derived from the mass concentrations of eBC with the default ratio (5.99E-5 μg m^{-3}/ particle.cm^{-3}) in OPAC.”

Line 230: at -> of?
Response: We corrected this.

“where DRE_{eBC} is the DRE of source-specific eBC, $F\downarrow$ and $F\uparrow$ are the downward and upward flux, $DRE_{eBC,ATM}$ is the DRE of the source-specific eBC for the atmospheric column, that is, the DRE at the top of the atmosphere ($DRE_{eBC,TOA}$) minus that at the surface ($DRE_{eBC,SUF}$).”

Lines 238-239: Provide some more background or at least some references
Response: Thanks for the suggestion. We have added some background information about the Bootstrap (BS) and Displacement (DISP) with some references. Now it reads:

“Two diagnostic methods, Bootstrap (BS) and Displacement (DISP) (Norris et al, 2014; Brown et al. 2015) were used to validate the robustness and stability of the results. The BS method was used to assess the random errors and partially assess the effects of rotational ambiguity while DISP was used to evaluate rotational ambiguity errors. The results of the BS and DISP analyses showed that there was no swap for the 4-factor solution (Table S3).”

Line283: variations… varied… rephrase.
Response: We have corrected this awkward sentence:

"The results showed that eBC_{fossil} and $eBC_{biomass}$ were only weakly correlated ($r = 0.3$, Figure S9), indicating a reasonably good separation, and furthermore, their diel variations showed different patterns (Figure 2)."

Lines 293 – 294. Remove "New para here"
Response: We deleted it.

Line 295: why did the biomass burning increase after 6 pm? Is it indoor biomass burning for cooking or heating, or is it some other biomass burning?
Response: Based on previous research (Xie et al., 2010, Zhou et al., 2018) and what we know about residential energy usage in rural areas of Baoji, biomass is commonly used as fuel for residential cooking and heating. Therefore we believe that the biomass burning increased after 6 pm due to the evening meal preparation and residential heating.

To make this clear, we have revised this:

"In contrast, the diel variation of $eBC_{biomass}$ (Figure 2b) showed greater influences from meteorological conditions during the daytime, and $eBC_{biomass}$ showed lower concentrations during the day compared with the night. After 6 p.m., increased biomass burning from cooking and residential heating let to the emission of more $eBC_{biomass}$ and the stable PBLH hindered the dispersion of $eBC_{biomass}$; these two factors caused the $eBC_{biomass}$ to reach its peak at 8 p.m."

Figure 3, caption: Explain the meaning of the gray and yellow areas even if that's explained in the text.
Response: We added an explanation to the figure caption as follows:

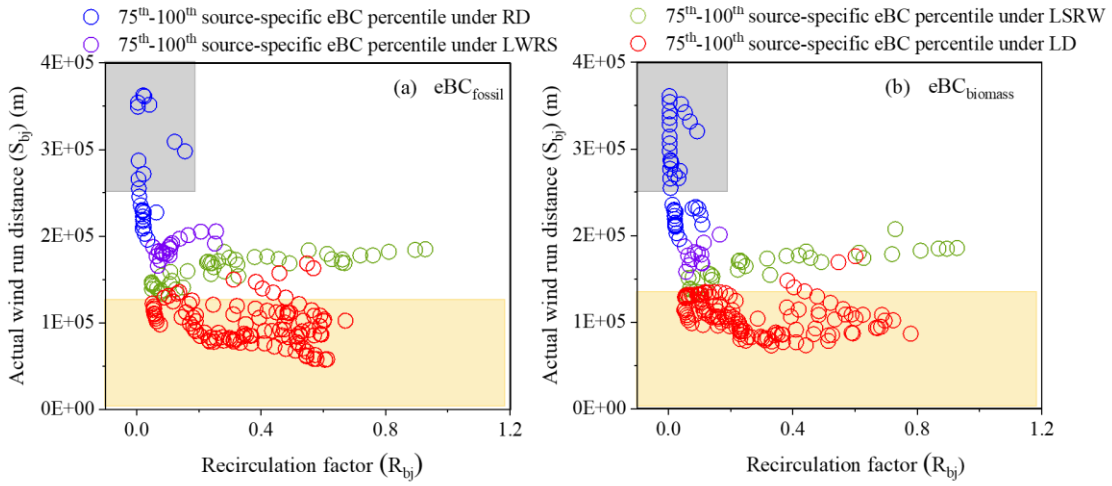

Figure R5. The 75th – 100th percentile mass concentrations of the eBC from fossil fuel combustion (eBC_{fossil}) and (b) the eBC from biomass burning ($eBC_{biomass}$) under local scale dominance (LD, red circle), local scale strong and regional scale weak (LSRW, green circle), local scale weak regional scale strong (LWRS, purple circle) and regional scale dominance (RD, blue circle). S_{bj} is actual wind run distance at 100m height, R_{bj} is the recirculation factor, the grey area indicates good ventilation ($S_{bj} \geq 250km$, $R_{bj} \leq 0.2$), the yellow area indicates air stagnation ($S_{bj} \leq 130km$).

Line 344: can one try to verify this with the backtrajectory analysis, or satellite products. etc.

Response: To verify the sources of eBC$_{\text{biomass}}$ located further than that of eBC$_{\text{fossil}}$, we used non-parametric wind regression plots (Gu et al, 2020). As shown in the Figure R6, during the night, the eBC$_{\text{biomass}}$ was higher when the wind speed was higher, while the eBC$_{\text{fossil}}$ was higher when the winds were lower. This indicates that during night, the emission sources of eBC$_{\text{biomass}}$ were located further than the sources for eBC$_{\text{fossil}}$, which explains why the mass concentrations of eBC$_{\text{biomass}}$ did not decrease with the influence of regional-scale atmospheric motion increased. We have added this figure into the supplementary materials.

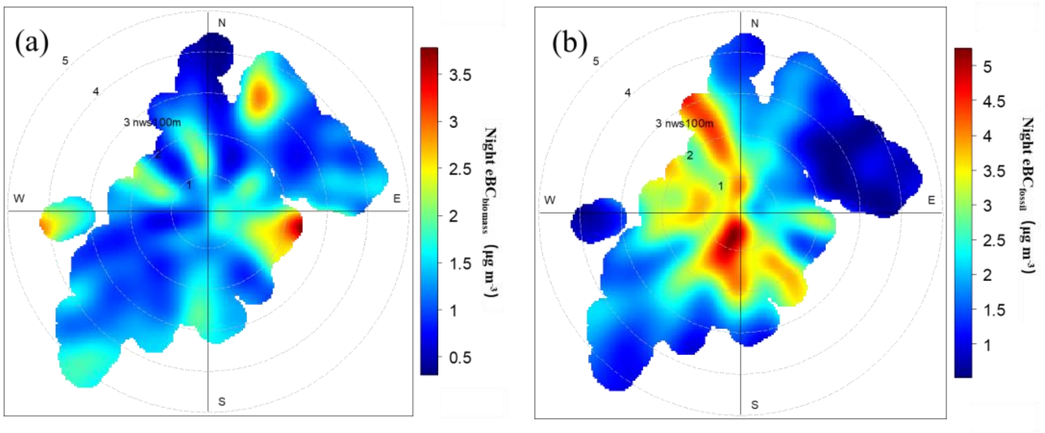

Figure R6 Non-parametric wind regression plots for eBC$_{\text{biomass}}$ (a) and eBC$_{\text{fossil}}$ (b) at night. The radial and tangential axes represent the wind direction (°) and speed (m s^{-1}), respectively, nws100m represents the night wind speed 100m above the ground level.

Reference:

Gu, Y., Huang, R., Li, Y., et al., Chemical nature and sources of fine particles in urban Beijing: Seasonality and formation mechanisms, Environmental International, 140, 155732, https://doi.org/10.1016/j.envint.2020.105732, 2020

Line 350: I would suggest briefly summarizing what the angle distance clustering method is and how it works even if that's explained in detail in the cited paper.

Response: Thanks for the suggestion, we have added the detailed method explanation in the supplementary materials (Text S1) as shown in the response above. In the revised manuscript, the sentence reads like:

"To examine the impacts caused by air masses from different directions, the hourly 24h-back trajectories were calculated at 100 m above the ground using the Hybrid Single-Particle Lagrangian Integrated Trajectory model (Draxler and Hess, 1998, Text S2). Then the trajectories were clustered by using an angle-based distance statistics method (Text S2) to show the general directional features. This method determines the direction from which the air masses reach the site and has been widely used for air mass trajectory clusters. A detailed method description can be found in Sirois and Bottenheim (1995)."

Lines 360 – 362: Rephrase this sentence, there are several awkward readability issues.

Response: We have rewritten the sentence, now it reads:

"This could be attributed to more intensive emissions in the eastern parts of Baoji because 75% of the total population of Baoji is located in this area (http://tjj.baoji.gov.cn/art/2020/10/15/art_9233_1216737.html, accessed on 25 September 2021, in Chinese)."

Line 360: remove "at" before "in"
Response: We apologize for this mistake, "at" has been removed from the sentence as shown in the response above.

Paragraph starting at line 405, specifically lines 411- 413: this is consistent with the higher MAC values.
Response: Yes, we agree. The higher DRE efficiencies can be attributed to the enhanced MAC of BC during the regional transport. So we have added the following text into the paragraph:

"Although $DRE_{eBC,\ ATM}$ declined with increased influences from the regional scale of motion, the $DRE_{eBC,\ ATM}$ efficiency ($DRE_{eBC,\ ATM}$ per mass concentration) was found to increase with greater regional-scale motion. Furthermore, the DRE efficiencies of both types of eBC under LD and LSRW were comparable, around 10 W m^{-2} (Table 2). In contrast, the efficiencies varied more when the regional-scale motions were stronger. Under LWRS, the efficiencies of eBC_{fossil} and $eBC_{biomass}$ were 13.5 ± 6.7 and 14.7 ± 8.1 (W m^{-2})/(μg m^{-3}) respectively. Under RD, the efficiencies were even higher, 15.6 ± 8.9 (W m^{-2})/(μg m^{-3}) for eBC_{fossil} and 15.5 ± 8.4 (W m^{-2})/(μg m^{-3}) for $eBC_{biomass}$, which are > 1.5 times those recorded under LD. The higher eBC efficiencies may have been caused by the increases in the BC MAC during the regional transport. Studies have confirmed that the aging processes in the atmosphere can enhance the light-absorbing ability of BC (Chen et al., 2017; Shen et al., 2014), and regional transport can provide sufficient time for BC aging (Shiraiwa, et al. 2007; Cho et al., 2021)."

Caption of figure 5: explain what the different shadings represent. Also, x-axis label number four probably should be "DREeBCfossil, TOA" not "DREeBCbiomass, TOA". It could be interesting to add another two panels with the equivalent calculations but in terms of efficiency to make more clear what is discussed in words in the paper.
Response: Thank you for pointing out this mistake. We have corrected the label and explained the shading and as suggested, we also added two figures. The figure has been replaced with following one:

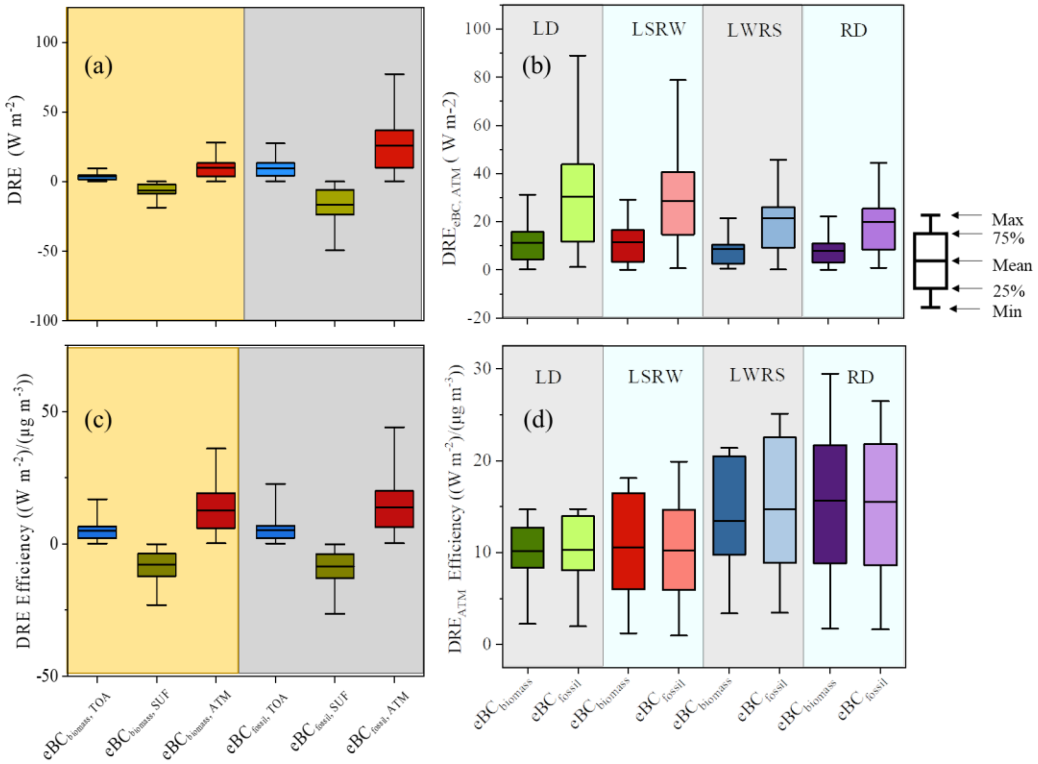

Figure R7. Direct radiative effect (DRE) of the eBC from fossil fuel combustion (eBC$_{fossil}$) shaded in grey and the eBC from biomass burning (eBC$_{biomass}$) shaded in yellow (a) in the top atmosphere (TOA), surface (SUF), and the atmosphere atmospheric column (ATM) and (b) the DRE$_{eBC,ATM}$ of two types of eBC under local scale dominance (LD) shaded in light grey labeled as LD, local scale strong and regional scale weak (LSRW) shaded in light blue labeled as LSRW, local scale weak regional scale strong (LWRS) shaded in light grey labeled with LWRS and regional scale dominance (RD) shaded in light blue labeled as RD (c) DRE efficiencies of eBC$_{biomass}$ (shaded in yellow) and eBC$_{fossil}$ (shaded by grey) in TOA, SUF and ATM (d) DRE efficiencies of eBC$_{biomass}$ and eBC$_{fossil}$ at ATM under LD (shaded in light grey labeled as LD), LSRW (shaded in light blue labeled as LSRW), LWRS (shaded in light grey labeled as LWRS) and RD (shaded in light blue labeled with RD).

Comment on acp-2022-26 titled "Review of "The impact of atmospheric motion on source-specific black carbon and the induced direct radiative effect over a river-valley region" by Liu et al.

Anonymous Referee #1

General comment

This manuscript describes how Black Carbon concentrations, measured over a little more than a month in winter 2018 together with other chemical species in $PM_{2.5}$ in a Chinese city nestled at the bottom of a valley, vary with different transport regimes and motion scales (from local to regional).

Response: We sincerely thank the reviewer for the comments and suggestions, and we have extensively revised the relevant text and modified the content. Below are point-by-point responses—the modifications to the manuscript are included.

The topic of the manuscript fits within the scope of the journal. The methodology should be described more precisely to build confidence in the results.

Response: We revised the methods to provide more details, particularly for the optical source apportionment and SOM. Other methods also have been revised according to the reviewer's suggestions. In addition, we have provided information regarding the cluster analysis and minimum R squared method in the supplementary materials. The changes are shown in the revised version. The revised paragraphs now read as follows:

"**2.2 Sampling and laboratory measurements**

eBC and the absorption coefficients (b_{abs}) at 370, 470, 520, 590, 660, 880, and 950 nm wavelength were measured using an AE33 aethalometer (Magee Scientific, Berkeley, CA, USA) equipped with a $PM_{2.5}$ cut-off inlet (SCC 1.829, BGI Inc. USA) that had a time resolution of 1 min. A Nafion® dryer (MD-700-24S-3; Perma Pure, Inc., Lakewood, NJ, USA) with a flow rate of 5 L min^{-1} was used to dry the $PM_{2.5}$ before the measurement. Briefly, the particles were dried by the Nafion® dryer before being measured with the AE33 aethalometer, and the deposited particles were irradiated by light-emitting diodes at seven wavelengths of light-emitting diodes (λ = 370, 470, 520, 590,660, 880, and 950 nm), and the light attenuation was detected. The non-linear loading issue for filter-based absorption measurement was accounted for in the AE33 by a technique called dual-spot compensation. The quartz filter (PN8060) matrix scattering effect was corrected by using a factor of 1.39. More details of AE33 measurement techniques can be found in Drinovec et al. (2015).

The scattering coefficient (b_{scat}) at a single (525) nm wavelength was measured with the use of a nephelometer (Aurora-1000, Ecotech, USA) that had a time resolution of 5 min. The nephelometer and aethalometer operated simultaneously and used the same $PM_{2.5}$ cyclone and Nafion® dryer. The calibration was conducted based on the user guide with a calibration gas R-134. Zero calibrations were conducted every other day by using clean air without particles. The ambient air was drawn in through a heated inlet with a flow rate of 5 L min^{-1}. The relative humidity remained lower than 60%.

$PM_{2.5}$ samples were collected for every 24 hours (h) from 10 a.m. local time to the 10 a.m. the next day from 16th November 2018 to 21st December 2018 with two sets of mini-volume samplers (Airmetrics, USA), one using quartz fiber filters (QM/A; Whatman, Middlesex, UK) and the other with Teflon® filters (Pall

Corporation, USA), both with a flow rate of 5 L min^{-1}. Those samples were kept in a refrigerator at 4°C before analysis. The mass concentration of K^+ in the $PM_{2.5}$ quartz sample was extracted in a separate 15 mL vials containing 10 mL distilled deionized water (18.2 MΩ resistivity). The vials were placed in an ultrasonic water bath and shaken with a mechanical shaker for 1 h to extract the ions and determined by a Metrohm 940 Professional IC Vario (Metrohm AG., Herisau, Switzerland) with Metrosep C6-150/4.0 column (1.7 mmol/L nitric acid+1.7 mmol/L dipicolinic acid as the eluent) for cation analysis. A group of elements (i.e. Mg, Al, Si, S, Cl, Ca, V, Mn, Fe, Ni, Cu, As, Se, Br, Sr, Pb, Ga, and Zn) on the Teflon® filters was were determined by energy-dispersive x-ray fluorescence (ED-XRF) spectrometry (Epsilon 4 ED-XRF, PANalytical B.V., Netherlands). The X-rays were generated from a gadolinium anode on a side-window X-ray tube. A spectrum of the ratio of X-ray and photon energy was obtained after 24 minutes of analysis for each sample with each energy peak characteristic of a specific element, and the peak areas were proportional to the concentrations of the elements. Quality control was conducted on a daily basis with test standard sample.

Organic carbon (OC) and elemental carbon (EC) in each sample were determined with the use of a DRI Model 2001 Thermal/Optical Carbon Analyzer (Atmoslytic Inc., Calabasas, CA, USA). The thermal/optical reflectance (TOR) method and IMPROVE_A protocol were used for analysis. A punch of a quartz filter sample was heated at specific temperatures to obtain data for four OC fractions and three EC fractions. Total OC was calculated by summing all OC fractions and the pyrolyzed carbon (OP) produced. Total EC was calculated by summing all EC fractions minus the OP. Detailed methods and quality assurance/quality control processes were described in Cao et al., (2003). Primary organic carbon (POC) was estimated by using the minimum R-squared (MRS) method, which is based on using eBC as a tracer (Text S1). The method uses the minimum R^2 between OC and eBC to indicate where the ratio for which secondary OC and eBC are independent. A detailed description of the MRS method can be found in Wu et al., (2016).

Data for NO_x, wind speed, and direction at 12 ground monitoring sites were downloaded from http://sthjt.shaanxi.gov.cn/hx_html/zdjkqy/index.html. The wind data at 100 meters (m) above the ground and the planetary boundary layer height were downloaded from https://rda.ucar.edu/datasets/ds633.0. The data used for the Hybrid Single-Particle Lagrangian Integrated Trajectory (HYSPLIT) model was downloaded from Global Data Assimilation System and it had a resolution of 1°×1° (GDAS, https://www.ready.noaa.gov/gdas1.php). The data and main parameters used in trajectory model are listed in Table S2."

2.3 Optical source apportionment

The positive matrix factorization (PMF) model that was used for the optical source apportionment in this study. PMF solves chemical mass balance by decomposing the observational data into different source profiles and contribution matrices as follows:

$$X_{ij} = \sum_{k=1}^{p} g_{ik} f_{kj} + e_{ij} \tag{1}$$

where X_{ij} denotes the input data matrix; p is the number of sources selected in the model; g_{ik} denotes the contribution of the k^{th} factor to the i^{th} input data; f_{kj} represents the k^{th} factor's profile of the j^{th} species; and e_{ij} represents the residual. Both g_{ik} and f_{kj} are non-negative. The uncertainties of each species and $b_{abs}(\lambda)$ were calculated by the equation recommended in EPA PMF5.0 user guideline(Norris et al, 2014) as follows:

$$Unc = \sqrt{(error\ fraction \times concentration(or\ ligth\ absorption\ coefficient))^2 + (0.5 \times MDL)^2} \tag{2}$$

$$Unc = \frac{5}{6} \times MDL \tag{3}$$

where MDL is the minimum detection limit of the method. When the concentration of a species was higher than the MDL then equation (2) was used otherwise equation (3) was used. In equation (2), for calculating the uncertainty of a chemical species, the error fraction was multiplied the concentration of the species. For calculating the uncertainty of optical data, the error fractions were multiplied by the light absorption coefficients.

Chemical species data (EC, POC, K^+, Mg, Al, Si, S, Cl, Ca, V, Mn, Fe, Ni, Cu, As, Se, Br, Sr, Pb, Ga and Zn) and the primary absorption coefficients (Pabs) data at λ=370nm,470nm,520nm,660nm, and 880nm were used for PMF analysis. The error fraction of offline measured data was the difference between multiple measurements of the same sample. The error fraction used for optical data was 10% based on Rajesh and Ramachandran (2018). PMF solves the equation (1) by minimizing the Q value, which is the sum of the normalized residuals' squares, as follows,

$$Q = \sum_{i=1}^{n} \sum_{j=0}^{n} \left[\frac{e_{ij}}{u_{ij}}\right]^2 \tag{4}$$

where u_{ij} represents the uncertainties of each X_{ij} and Q_{true}/Q_{exp} was used as the indicators for the factor number determination.

2.4 eBC source apportionment

The quantities of eBC generated from biomass burning versus fossil fuel combustion were deconvolved by an aethalometer model which uses Beer-Lambert's Law to write the absorption coefficients equations, wavelengths and absorption Ångström exponents (AAEs) for the two different BC emission sources (Sandradewi et. al., 2008). This approach is widely used for separating BC from two different sources based on optical data (Rajesh et al., 2018; Kant et al., 2019; Panicker et al., 2010). However, the traditional aethalometer model could be affected by the light absorbing substances at lower wavelengths such as dust and secondary formation particles. An improvement to the traditional aethalometer model was made, by explicitly considering the interference of the b_{abs} at a lower wavelength (370nm) caused by dust and secondary OC. Thus, the calculation of the absorption and source apportionment was based on the following equations (Wang et al., 2020):

$$\frac{b_{abs}(370)_{fossil}}{b_{abs}(880)_{fossil}} = \left(\frac{370}{880}\right)^{-AAE_{fossil}} \tag{5}$$

$$\frac{b_{abs}(370)_{biomass}}{b_{abs}(880)_{biomass}} = \left(\frac{370}{880}\right)^{-AAE_{biomass}} \tag{6}$$

$$b_{abs}(880) = b_{abs}(880)_{fossil} + b_{abs}(880)_{biomass} \tag{7}$$

$$b_{abs}(370) = b_{abs}(370)_{fossil} + b_{abs}(370)_{biomass} + b_{abs}(370)_{secondary} + b_{abs}(370)_{dust} \tag{8}$$

$$eBC_{fossil} = \frac{b_{abs}(880)_{fossil}}{MAC_{BC}(880)_{fossil}} \tag{9}$$

$$eBC_{biomass} = \frac{b_{abs}(880)_{biomass}}{MAC_{BC}(880)_{biomass}} \tag{10}$$

where AAE_{fossil} and $AAE_{biomass}$ are the AAEs for fossil fuel combustion and biomass burning. These were derived from the optical source apportionment by using PMF as discussed in section 3.1. Further, $b_{abs}(370)$ and $b_{abs}(880)$ are the total b_{abs} measured by the AE33 at the wavelengths of 370 nm and 880 nm respectively; $b_{abs}(370)_{fossil}$ and $b_{abs}(880)_{fossil}$ are the b_{abs} caused by emissions from fossil fuel combustion at those two wavelengths; $b_{abs}(370)_{biomass}$ and $b_{abs}(880)_{biomass}$ are the b_{abs} caused by emissions from biomass burning at those two wavelengths; $b_{abs}(370)_{dust}$ refers to the b_{abs} contributed by mineral dust at the wavelength of 370 nm, which was derived from the result of optical source apportionment; $b_{abs}(370)_{secondary}$ refers to the b_{abs} caused by the secondary aerosols at the wavelength of 370 nm, which was calculated by the minimum R-squared approach with eBC as a tracer (Text S1, Wang et al., 2019); eBC_{fossil} and $eBC_{biomass}$ are the eBCs from fossil fuel combustion and biomass burning; and $MAC_{BC}(880)_{fossil}$ and $MAC_{BC}(880)_{biomass}$ are the mass absorption cross-sections of eBC_{fossil} and the mass absorption cross-section of $eBC_{biomass}$ at the wavelength of 880 nm respectively, which were based on the PMF results for the optical source apportionments.

2.5 Indicators for the different scales of motion

The mathematical definitions of airflow condition proposed by Allwine and Whiteman (1994) were used in this study. The definitions quantify the flow features integrally at individual stations. Three variables were quantified, namely the actual wind run distance (S) which is the scalar displacement of the wind in 24 h (i.e. the accumulated distance of the wind), the resultant transport distance (L) which is the vector displacement of the wind in 24 h (i.e. the straight line from the starting point to the end point), and the recirculation factor (R) is based on the ratio of L and S which indicates the frequency of the wind veering in 24 h. The influences of different scales of atmospheric motions were assessed based on the method proposed by Levy et al., (2010), and for this, we used wind data at 100 m above the sampling site and the wind data from 12 monitoring stations at ground level (~15m) to indicate the different scales of motions. The winds at the surface monitoring stations were expected to be more sensitive to local-scale turbulence and convection than the winds at 100 m. With less influence from the surface forces, the indicators at 100 m would be more sensitive to larger scales of motion. The equations used as follows:

$$L_{n\tau/bj} = T\left[\left(\sum_{j=i}^{i-\tau+1} u_i\right)^2 + \left(\sum_{j=i}^{i-\tau+1} v_i\right)^2\right]^{1/2} \tag{11}$$

$$S_{n\tau/bj} = \sum_{j=i}^{i-\tau+1}\left(u_j{}^2 + v_j{}^2\right)^{1/2} \tag{12}$$

$$R_{n\tau/bj} = 1 - \frac{L_{i\tau}}{S_{i\tau}} \tag{13}$$

where T is the interval of the data (i.e., 60 min), i is the i^{th} the ending time step data, τ is the integration time period of the wind run (24 h), $i-\tau+1$ represents the data at the start time, and n is the number of monitoring stations (a total of 12 in this study). The quantities u and v are the wind vectors. Using the wind data from the 12 monitoring stations covering Baoji, the L and S values at the 12 different sites at ground level were calculated. $L_{n\tau}$ and $S_{n\tau}$ represent the resultant transport distance and the actual wind run distance at the n^{th} (n = 1 to 12) monitoring station at ground level; $R_{n\tau}$ is the recirculation factor at the n^{th} monitoring station which is calculated based on $L_{n\tau}$; and $S_{n\tau}$; L_{bj}, and S_{bj} are the resultant transport distance and the actual wind run distance at 100 m height above the ground. These represent the flow characteristics in higher atmosphere at the study site, and they were calculated by using the wind data at 100 m height. The recirculation factor (R_{bj}) was calculated for a height of 100 m.

As explained in Levy et al., (2010), if local-scale motions are strong and regional-scale motions are weak, the variations in winds at each station would not be likely to be uniform due to differences in local factors, and that would result in relatively large standard deviations (R_{std}) for $R_{n\tau}$. By contrast, if the local-scale motions are weak and the regional-scale motions are strong, the wind direction would be likely to be more uniform over a large area, and the R_{bj} and the R_{std} should be relatively smaller.

2.6 Self-organizing map

A self-organizing map (SOM) developed by Kohonen (1990) is a type of artificial neural network that is widely used for categorizing high-dimensional data into a few major features (Stauffer et al., 2016 and Pearce et al., 2014). In particular, this approach is widely used for categorizing different meteorological patterns (Liao et al., 2020; Han et al., 2020; Jiang et al., 2017). Unlike traditional dimension reduction methods (e.g., principal component analysis), SOM projects high-dimensional input data by non-linear projection into user-designed lower-dimensions, which are typically two-dimensional arrays of nodes

(Hewitson and Crane, 2006). The performance of SOM in classifying climatological data has been shown to be robust (Reusch et al., 2005). Competitive learning algorithms are used to train SOM, and the architecture of SOM consists of two layers; one is called the input layer and it contains the high dimensional input data. The other layer is the output layer in which the node number is the output cluster number. The working principle of SOM is to convert high dimensional data with complex correlations into lower dimensions via geometrical relationships (Ramachandran et al., 2019). After the initial random weights are generated, the input data are compared with each weight, and the best match is defined as winning. The winning node and the neighboring nodes close to the winning node will learn from the same inputs and the associated weights are updated. After multiple iterations, the network to settles into stable zones of features and the weights. More detailed working principles of SOM can be found Kangas and Kohonen, (1996) and Kohonen et al., (1996).

Comparison between the input data and each weight is made by applying Euclidean distances, the best match is defined by the following equation:

$$\|x - m_c\| = min\{\|x - m_i\|\} \tag{14}$$

where x is the input data, m_c is the best matched weight, m_i is the weights connected with the i^{th} node.

The weights are updated by following equation:

$$m_i(t+1) = m_i(t) + h_{ci}(t)[x(t) - m_i(t)] \tag{15}$$

where the $m_i(t+1)$ is the i^{th} weight at t+1 time, $m_i(t)$ is the i^{th} weight at t time, the $h_{ci}(t)$ is the neighborhood kernel defined over the lattice points at t time, and *c* is the winning node location.

SOM was used to categorize the daily atmospheric motions during the study period and to explore the influences of different scales of motion on source-specific eBC. Hourly averages of three sets of data (R_{std}, L_{bj}, and S_{bj}) were input into SOM. Determining the size of the output map is crucial for SOM (Chang et al 2020 and Liu et al., 2021). To reduce the subjectivity, the K-means cluster method was used for the decision-making regarding size. The similarity of each item of the input data relative to the node was measured using Euclidean distance. The iteration number was set to 2000. For each input data item, the node closest to it would “win out”. The reference vectors of the winning node and their neighborhood nodes were updated and adjusted towards the data. The “Kohonen” package in *R* language (Wehrens and Kruisselbrink, 2019) was used to develop the SOM model in this study.

2.7 Estimations of direct radiative effects and heating rate

The Santa Barbara DISORT Atmospheric Radiative Transfer (SBDART) model was used to estimate the direct radiative effects (DRE) induced by source-specific eBC. The model has been used in many studies to calculate the DRE caused by aerosols and BC (Pathak et al., 2010; Rajesh et al., 2018; Zhao et al., 2019). SBDART calculated DRE based on several well-tested physical models. Details regarding the model were presented in Ricchiazzi et al., (1998). The important input data included aerosol parameters, including aerosol optical depth (AOD), single scattering albedo (SSA), asymmetric factor (AF) and extinction efficiency, surface albedo, and atmospheric profile.

The aerosol parameters used in this study were derived by the Optical Property of Aerosol and Cloud (OPAC) model (Hess et al., 1998) based on the number concentrations of aerosol components. As the study was conducted in an urban region, the urban aerosol profile was used in OPAC, and it included soot (eBC), water-soluble matter (WS), and water-insoluble matter (WIS). The number concentrations of soot were derived from the mass concentrations of eBC with the default ratio (5.99E-5 μg m^{-3}/ particle.cm^{-3}) in OPAC.

The number concentrations of WS and WIS were adjusted until the modeled SSA and b_{abs} at 500nm in OPAC were close (±5%, see Figure S4) to those values calculated with data from the nephelometer and AE33 ($b_{\mathrm{ext}}(520) = b_{\mathrm{scat}}(525) + b_{\mathrm{abs}}(520)$, SSA= $b_{\mathrm{scat}}(525)/b_{\mathrm{ext}}(520)$). The DRE of source-specific eBC at the top of atmosphere (TOA) and surface atmosphere (SUF) were calculated from the difference between the DREs with or without the number concentrations of the source-specific eBC under clear-sky conditions.

$$DRE_{eBC} = (F\downarrow - F\uparrow)_{with\ eBC} - (F\downarrow - F\uparrow)_{without\ eBC} \tag{16}$$

$$DRE_{eBC,ATM} = DRE_{eBC,TOA} - DRE_{eBC,SUF} \tag{17}$$

where DRE_{eBC} is the DRE of source-specific eBC, $F\downarrow$ and $F\uparrow$ are the downward and upward flux, $DRE_{eBC,ATM}$ is the DRE of the source-specific eBC for the atmospheric column, that is, the DRE at the top of the atmosphere ($DRE_{eBC,TOA}$) minus that at the surface ($DRE_{eBC,SUF}$).”

“Text S1. Minimum R - squared method

The minimum R squared method developed by Wu et al., (2016) was used to separate secondary organic carbon (SOC) from the primary organic carbon (POC). The assumption behind this method is the organic carbon (OC) from non-combustion source is negligible. As explained by Wang et al., (2019), the major non-combustion source is biogenic which is mainly exists in coarse mode. Thus, the non-combustion organic carbon is considered negligible in this study. Therefore, SOC and POC can be separated by using following equations. For each date set, the ratios of OC to eBC and SOC and the R^2 between eBC and SOC can be calculated. SOC and eBC are considered independent, so the (OC/eBC)pri should be the value obtained when the R^2 between eBC and SOC is minimum.

$$\mathrm{POC} = (\mathrm{OC}/\mathrm{EC})_{\mathrm{pri}} \times \mathrm{EC} \tag{S1}$$

$$\mathrm{SOC} = \mathrm{OC}_{\mathrm{total}} - (\mathrm{OC}/\mathrm{EC})_{\mathrm{pri}} \times \mathrm{EC} \tag{S2}$$

where EC in this study is eBC. The $(\mathrm{OC/EC})_{\mathrm{pri}}$ is the ratio in freshly emitted OC and EC from combustion sources.

The light absorption at shorter wavelengths (<660nm) is not only from primary light absorbing substances but also from the secondary organic carbon (Wang et al., 2019). The assumption for this method is that the light absorption caused by non-combustion sources is negligible. As mentioned above, most of the biogenic BrC is in coarse mode. Another common light absorbing substance is the Fe_2O_3 in the dust, but the impact of that should be limited because the absorption from Fe_2O_3 in the dust has been reported to be much smaller than that from BC (Ramachandran and Kedia, 2010). Thus, to separate the secondary light absorption ($b_{\mathrm{abs}}(\lambda)_{\mathrm{secondary}}$) from the primary light absorption ($b_{\mathrm{abs}}(\lambda)_{\mathrm{primary}}$), a BC-tracer method coupled with a minimum R-squared method was used. The equations used for the calculation are follows:

$$b_{\mathrm{abs}}(\lambda)_{\mathrm{secondary}} = b_{\mathrm{abs}}(\lambda) - \left(\frac{b_{\mathrm{abs}}(\lambda)}{\mathrm{BC}}\right)_{\mathrm{pri}} \times \mathrm{BC} \tag{S3}$$

$$b_{\mathrm{abs}}(\lambda)_{\mathrm{primary}} = b_{\mathrm{abs}}(\lambda) - b_{\mathrm{abs}}(\lambda)_{\mathrm{secondary}} \tag{S4}$$

Where $b_{\mathrm{abs}}(\lambda)$ is the light absorption at different wavelengths (λ=370nm, 470nm, 520nm, 590nm, 660nm) measured by AE33, BC is the eBC measured by AE33 at a wavelength of 880nm. The $\left(\frac{b_{\mathrm{abs}}(\lambda)}{\mathrm{BC}}\right)_{\mathrm{pri}}$ is the ratio of the primary light absorption to the BC mas concentration from combustion sources.

Text S2. Cluster analysis of air-mass trajectories

Back trajectories were calculated by using Hybrid Single-Particle Lagrangian Integrated Trajectory (HYSPLIT) model (Draxler and Hess, 1998) developed by the Air Resource Lab (ARL) of the National Oceanic and Atmospheric Administration (NOAA). The model can predict the position of air mass by using mean wind. The back-in-time positions are calculated by reversing the advection equation (Draxler and Hess, 1997). The calculation requires the mean wind, for calculating trajectories, only advection is considered (Stein et al., 2015). The basic equations for trajectory calculation in HYSPLIT are as follows:

$$P'(t+\Delta t) = P(t) + V(P,t) \times \Delta t \qquad \text{(S5)}$$

$$P(t+\Delta t) = P(t) + 0.5 \times [V(P,t) + V\left(P', t+\Delta t\right)] \times \Delta t \qquad \text{(S6)}$$

Where $P(t)$ is the initial position, $P'(t+\Delta t)$ is the first guess position, V is the average velocity, t is the time, Δt is the time step.

A large number of 24 h trajectories (793) that were retrieved for the study period showed diverse pathways, so in order to find out the representative pathways for those trajectories, a cluster analysis based on an angle-based distance statistics method was conducted. Compared with Euclidean distance, angle-based distance statistics method focuses on the direction of air mass instead of the speed. The angle-based distance statistics method is defined by following equations (Sirois and Bottenheim, 1995):

$$d_{12} = \frac{1}{2}\sum_{i=1}^{n} cos^{-1}(0.5 \times \frac{A_i+B_i-C_i}{\sqrt{A_iB_i}}) \qquad \text{(S7)}$$

$$A_i = (X_1(i) - X_0)^2 + (Y_1(i) - Y_0)^2 \qquad \text{(S8)}$$

$$B_i = (X_2(i) - X_0)^2 + (Y_2(i) - Y_0)^2 \qquad \text{(S9)}$$

$$C_i = (X_2(i) - X_1(i))^2 + (Y_2(i) - Y_1(i))^2 \qquad \text{(S10)}$$

Where d_{12} is the average angle between the two backward trajectories, varying between 0 and π; X_0 and Y_0 are the position of the receptor site; and X_1 (Y_1) and X_2 (Y_2) are the backward trajectories 1 and 2, respectively. In this study, three clusters were chosen as representative of the backward trajectory clusters based on the total spatial variance (TSV) value. The simulation was conducted using the GIS-based TrajStat software (Wang et al., 2009).”

The discussion section could be strengthened by comparing this work with other studies in similar topographic conditions.

Response: We have reviewed studies on BC pollution and the total DRE of BC at other river valley sites and compared them with this study. The revised text is as follows:

“The mean values of eBC_{fossil} and $eBC_{biomass}$ were 2.46 μg m^{-3} and 1.17 μg m^{-3}, respectively. The averaged total eBC mass concentration (± standard deviation) was 3.63±2.73μg m^{-3}, and the eBC ranged from varying from 0.39 to 12.73 μg m^{-3} during the study period, The averaged mass concentration was comparable to that in Lanzhou, another river valley city in China, that was sampled in the same season (5.1 ± 2.1, Zhao et al.,2019). The lowest value is comparable to other river valley regions such as in Retje in India (Glojek et al.,

2022) or in Urumqi River Valley in China (Zhang et al., 2020), however even the highest concentration was much lower than that in other urban regions (Table S5)."

"Figure 5a shows the DREs at top of the atmosphere ($DRE_{eBC, TOA}$), surface ($DRE_{eBC, SUF}$), and the whole atmosphere ($DRE_{eBC, ATM}$) of eBC_{fossil} and $eBC_{biomass}$. The $DRE_{eBC, TOA}$ and $DRE_{eBC, SUF}$ of eBC were 13 W m^{-2} and -22.9 W m^{-2}, which were lower than that reported in Lanzhou (21.8 W m^{-2} and -47.5 W m^{-2} for $DRE_{eBC, TOA}$ and $DRE_{eBC, SUF}$) – which is another a river valley city in China (Zhao et al., 2019). This could be due to fact that the eBC mass concentration in Baoji was lower than in Lanzhou (Table S5). As for the $DRE_{eBC, TOA}$ and $DRE_{eBC, SUF}$ per an unit mass of BC, the results of the two studies were comparable."

Table R1 Mean (range) BC mass concentration in river valley sites worldwide

Reference	BC concentration (μg m^{-3})	Season	Topographic conditions	Altitude	Station type	Year
This study	3.63±2.73 (0.39~12.73)	November~December (winter)	river valley	450 to 800 m a.s.l.[a]	urban	2018
Glojek et al., (2020)	0.9~40	December~January (winter)	river valley	715 m a.s.l.	rural	2017-2018
Zhao et al. (2015)	25±11	January (winter)	river valley	410 m a.s.l.	urban	2013
Barman and Gokhale (2019)	20.58~22.44	Winter	river valley		urban	2016-2017
Zhang et al., 2020	0.102~1.525	Winter	river valley	2130 m a.s.l.	rural	2016-2017
Chakrabarty et al., (2012)	9~41	January~February (winter)	river valley		urban	2011
Zhao et al. (2019)	5.1 ± 2.1	December~January (winter)	river valley		urban	2018
Tiwari et al., 2016	8.19 ±1.39	December-February (winter)	river valley	55 m a.s.l.	urban	2013-2014

[a] asl stands for "above sea level."

References:

Barman, N., and Gokhale, S., Urban black carbon - source apportionment, emissions and long-range transport over the Brahmaputra River Valley, Science of the Total Environment, 693, 133577, https://doi.org/10.1016/j.scitotenv.2019.07.383, 2019

Chakrabarty, R., Garro, M., Wilcox, E., and Moosmuller, H., Strong radiative heating due to wintertime black carbon aerosols in the Brahmaputra River Valley, Geophysical Research Letters, 39, L09804, https://doi.org/10.1029/2012GL051148, 2012.

Glojek, K., Moˇcnik, G., Alas, H., et al., The impact of temperature inversions on black carbon and particle mass concentrations in a mountainous area, Atmos. Chem. Phys., 22, 5577–5601, https://doi.org/10.5194/acp-22-5577-2022, 2022.

Zhang, X., Li, Z., Ming, J., and Wang, F., One-year measurements of equivalent black carbon, optical properties, and sources in the Urumqi River Valley, Tien Shan, China, Atmosphere, 11, 478, https://doi.org/10.3390/atmos11050478, 2020.

Zhao, S., Yu, Y., Yin, D., et al., Concentrations, optical and radiative properties of carbonaceous aerosols over urban Lanzhou, a typical valley city: Results from in-situ observations and numerical model, Atmospheric Environment, 213, 470–484, https://doi.org/10.1016/j.atmosenv.2019.06.046, 2019.

Zhao, S., Tie, X., Cao, J & Zhang, Q. (2015), Impacts of mountains on black carbon aerosol under different synoptic meteorology conditions in the Guanzhong region, China. Atmospheric Research, 164-165, 286-296. http://dx.doi.org/10.1016/j.atmosres.2015.05.016

Tiwari, S., Kumar, R., Tunved, P., Singh, S., and Panicker, A., Significant cooling effect on the surface due to soot particles over Brahmaputra River Valley region, India: An impact on regional climate, 2016, Science of the Total Environment, 562, 504–516, http://dx.doi.org/10.1016/j.scitotenv.2016.03.157, 2016.

The writing should be improved, I have suggested a few technical corrections in a specific section at the end.

Response: As suggested, we have had this manuscript polished by a native English speaker.

Specific comments:

L30: What type of "change" between a mass concentration and a radiative effect is expected? I am not sure the word "change" conveys your meaning.

Response: By "change" we meant that the changes in BC mass concentrations for the different scales of motions were not of the same magnitude as the changes in BC DRE. More specifically, we took LD as a base case to calculate the difference between the average BC mass concentrations (or average DRE) versus other cases (LSTW, LWRS and RD). Clearly the eBC$_{\text{fossil}}$ and eBC$_{\text{biomass}}$ concentrations decreased more than the corresponding DRE did (Table R2). This indicates that the DREs per unit mass of BC were variable (Table R3).

To avoid confusion, we revised it into "Similar to the mass concentrations, the DREs of the two types of eBC were both lower when the regional scale of motions were greater than the local ones. However, the changes in mass concentrations and DREs were not proportionate because the regional-scale of motions carried the fresh BC away from the local site but brought the aged BCs to the site from the upwind regions. As a result, the DRE efficiency of eBC was ~1.5 times higher when the regional scale of motion was stronger."

Table R2 The change of mass concentration of different eBCs and their DREs

Atmospheric motion category	Change of mass concentration of eBCfossil	Change of mass concentration of eBC$_{\text{biomass}}$	Change of DRE$_{\text{eBCfossil, ATM}}$	Change of DRE$_{\text{eBCbiomass, ATM}}$
LD	-	-	-	-
LSRW	9.4%	30.3%	5.7%	-2.9%
LWRS	30.2%	43.4%	29.3%	23.1%
RD	45.1%	38.8%	34.6%	29.0%

Table R3. Direct radiative forcing efficiencies for equivalent black carbon (eBC) from fossil fuel combustion (eBC$_{\text{fossil}}$) and the eBC from biomass burning (eBC$_{\text{biomass}}$) under four atmospheric motion categories

Atmospheric motion category	$DRE_{eBCfossil, ATM}$ efficiency ((W m^{-2})/(μg m^{-3}))	$DRE_{eBCbiomass, ATM}$ efficiency ((W m^{-2})/(μg m^{-3}))
Local scale dominance (LD)	10.2[a] ± 4.2[b]	10.3 ± 4.4
Local scale strong and regional scale weak (LSRW)	10.6 ±5.7	10.2 ± 5.8
Local scale weak and regional scale strong (LWRS)	13.5 ± 6.7	14.7 ± 8.1
Regional scale dominance (RD)	15.6 ± 8.9	15.5 ± 8.4

a and b: Mean ± Standard deviation

L37-38: "the second strongest light-absorbing substance in the atmosphere after CO2". This wording is confusing since it seems an intrinsic property of BC whatever its concentration level. Besides it is clearly related to (1) its climate forcing ability and (2) human emissions only, by Bond et al. (2013) which state that "We estimate that black carbon, with a total climate forcing of +1.1 W m^{-2}, is the second most important human emission in terms of its climate forcing in the present-day atmosphere; only carbon dioxide is estimated to have a greater forcing." (abstract) or "Our best estimate of black carbon forcing ranks it as the second most important individual climate-warming agent after carbon dioxide" (in 1.2.12 Policy implications). This sentence should thus be revised accordingly.

Response: Thanks for pointing this out, we have revised this sentence:

"Black carbon (BC) is produced by the incomplete combustion of biomass and fossil fuels. The BC aerosol has a strong light absorption capacity and can cause heating of the atmosphere. In fact, BC is widely recognized as one of the most important short-lived climate forcers (IPCC, 2021)."

In the abstract, the relevant sentence has also been revised into:

"Black carbon (BC) is one of the most important short lived climate forcers, and atmospheric motions play an important role in determining its mass concentrations of pollutants."

L60: "scale (it is atmosphere phenomena) ranges". I do not understand what the mention in brackets refers to?!

Response: We have deleted this—it was a mistake.

L62: I do not understand how an atmospheric dynamic feature (the local scale of motion) is eventually controlled by the concentration levels of BC?! Besides the land roughness, it can be influenced by thermals, turbulence, etc.

Response: We agree with reviewer that thermals and other factors cause local scales of motion, but the variations in the BC mass concentrations also can induce thermal differences horizontally and vertically. The horizontal temperature variations can give rise to horizontal pressure differences, which result in atmospheric motions (Oke, 1988). BC concentration also can impact the temperature structure of the atmosphere and cloud microphysical properties, the latter of which also can impact the temperature (IPCC, 2021). In this way, differences of BC mass concentrations between different locations can lead to atmospheric motions.

Reference:

Oke, T., Boundary Layer Climates, 2nd edition, Taylor & Francis e-Library, 2002.

IPCC: Climate Change 2021: The Physical Science Basis. Contribution of Working Group I to the Sixth Assessment Report of the Intergovernmental Panel on Climate Change [Masson-Delmotte, V., P. Zhai, A. Pirani, S.L. Connors, C. Péan, S. Berger, N. Caud, Y. Chen, L. Goldfarb, M.I. Gomis, M. (eds)], https://reliefweb.int/report/world/climate-change-2021-physical-science-basis, 2021

IPCC: Climate Change 2021: The Physical Science Basis. Contribution of Working Group I to the Sixth Assessment Report of the Intergovernmental Panel on Climate Change [Masson-Delmotte, V., P. Zhai, A. Pirani, S.L. Connors, C. Péan, S. Berger, N. Caud, Y. Chen, L. Goldfarb, M.I. Gomis, M. (eds)], https://reliefweb.int/report/world/climate-change-2021-physical-science-basis, 2021

L72-79: The authors mention the specific case of atmospheric dynamics in the context of a valley site surrounded by mountains. I am surprised not to find a word about temperature inversions which are very common in winter in such environments and have a tremendous impact on trapping pollution in valleys. See for instance Glojek et al. (2022), https://doi.org/10.5194/acp-22-5577-2022.

Response: We agree with reviewer that temperature inversions in river valley region are not uncommon and can exacerbate pollution problems. Indeed, this happens often in winter in Guanzhong Plain (Bei et al., 2016). Accordingly, we have added this background information into the description of the topography of the river-valley as follows:

"Topography also plays an important role in air pollution (Zhao et al., 2015). River-valley topography is complicated, and it can have a considerable influence on air pollution and synoptic patterns of flow (Green et al., 2016; Carvalho et al., 2006). The pollution levels at cities in river-valleys are not only influenced by general atmospheric dynamics but also strongly impacted by the local-scale of dynamics (Brulfert et al., 2006). Surface albedo and surface roughness are affected by the complex topography of river-valley regions, and those physical factors can affect circulation causing changes in pollutant mass concentrations (Wei et al., 2020). Mountains also significantly affect pollution, and once pollutants are generated or transported into the river-valley regions, their dispersal can be impeded by the blocking effect of the mountains. Instead of being dispersed, they can be carried by the airflows over the mountains to converge at the bottom of the valley and increase the pollutants along the river (Zhao et al., 2015). In this way, pollutants can accumulate in valleys and spread throughout the area, thereby aggravating pollution. In addition, temperature inversions commonly form in river-valleys during the winter, and that, too, can aggravate pollution problems (Glojek et al., 2022 and Bei et al., 2016)."

Reference:

Bei, N., Li, G., Huang, R., Cao, J., Meng, N., Feng, T., Liu, S., Zhang, T., Zhang, Q., and Molina, L.: Typical synoptic situations and their impacts on the wintertime air pollution in the Guanzhong basin, China, Atmos. Chem. Phys., 16, 7373–7387, http://dx.doi.org/10.5194/acp-16-7373-2016, 2016.

Glojek, K., Moˇcnik, G., Alas, H., Cuesta-Mosquera, A., Drinovec, L., Gregoriˇc, A., Ogrin, M., Ježek, I., Müller, T., Rigler, M., Remškar, M., Pinxteren, D., Herrmann, H., Ristorini, M., Merkel, M., Markelj, M., Wiedensohler, A.: The impact of temperature inversions on black carbon and particle mass concentrations in a mountainous area, Atmos. Chem. Phys., 22, 5577–5601, https://doi.org/10.5194/acp-22-5577-2022, 2022.

L87: The description of the research site and its surroundings is too brief. No mention of any altitude (site, surrounding mountains), which is a crucial parameter. The authors should provide a more detailed map of the city and the main local expected sources of Black Carbon (highway, residential areas, industries, etc.), as well as the 12 monitoring stations mentioned later in the text. It would also be helpful to know about the local wind rose over the different seasons, as well as basic meteorological data (temperature, RH profiles; precipitation patterns).

Response: We revised the site description to include the altitude, main local sources of BC, population density and so on. The seasonal meteorological data for Baoji is listed in Table R4 and the seasonal local wind roses are provided in Figure R1. The table and figure have been included in the supplementary materials. The revised site description is now reads:

"Baoji is a typical river-valley city, located at the furthest west of the Guanzhong Plain, at an altitude from 450 to 800 m a.s.l. (Figure S1), Baoji has a complex topography and often suffering from severe pollution in winter. It is surrounded by mountains to the south, west and north, with the Weihe River as the central axis extending eastward. The shape can be viewed as a funnel, with large opening to east. The Qinling peaks and the flat Weihe Plain are the main landforms of Baoji. The main peak of the Qinling Mountains is 3,767 m a.s.l. and it is the highest mountain in the eastern part of mainland China. This terrain causes divergent flow at local scales, which can impact pollution levels (Wei et al., 2020). Baoji also is an important railway intersection in China, connecting six railways to the north-west and southwest China. Pollutant levels can be high and pollutants are not easy to be dispersed in the city due to its special topographic conditions, dense population (total population of 0.341 million, with 63.5% population living in the downtown aera and population density of 6003 people per km^2 in 2019 (http://tjj.shaanxi.gov.cn/upload/2021/zk/indexch.htm and https://data.chinabaogao.com/hgshj/2021/042053X932021.html), and impacts from major highway and railway networks.

The sampling site was on the rooftop of a building at Baoji University of Arts and Sciences (34°21′16.8″N, 107°12′59.6″E, 569 m a.s.l.) surrounded by commercial and residential buildings, highways, and a river, there were no major industrial emission sources nearby. The main sources of BC in Baoji were the domestic fuel (coal and biomass) burning as well as the motor vehicle emissions (Zhou et al., 2018; Xiao et al., 2014). Open fire also can be sources for BC, but there were limited fire found scattered around the site (Figure S2). The meteorological conditions at Baoji for the four seasons are listed in Table S1, and the wind roses for the different seasons are shown in Figure S3(data are from the Meteorological Institute of Shaanxi Province)."

Table R4. The seasonal meteorological data of Baoji

Season	Temperature (℃)	Relative humidity (%)	Precipitation in last hour (mm)
Winter	2.7	60.6	0.025
Spring	11.5	54.9	0.042
Summer	23.7	67.1	0.139
Autumn	20.2	67.0	0.074

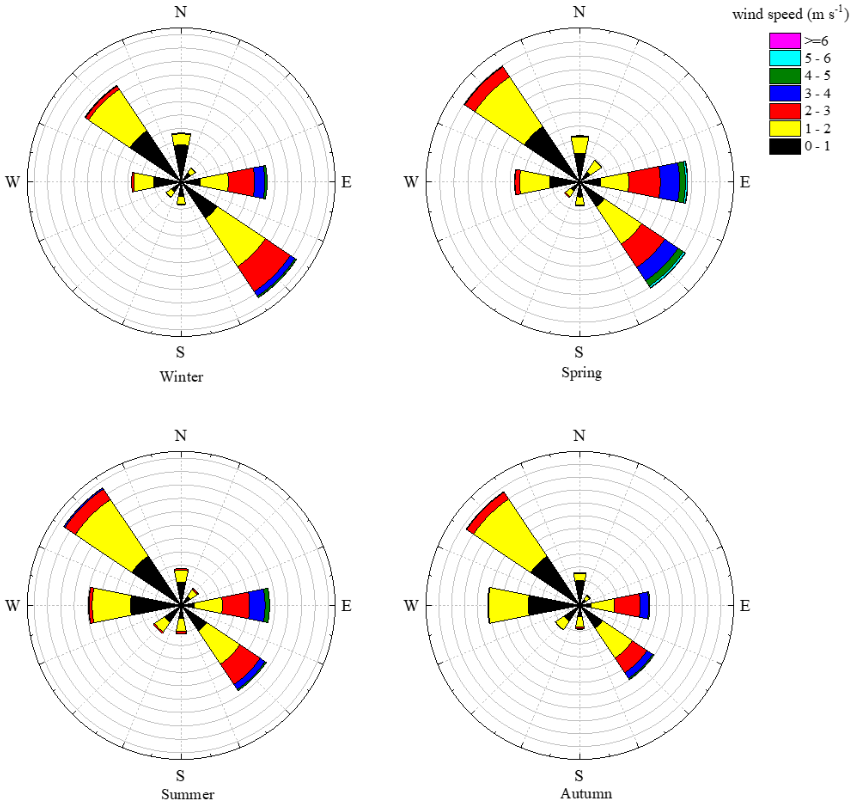

Figure R1 Seasonal wind roses for Baoji.

We also have updated the map of the region in supplementary materials. The new map looks like:

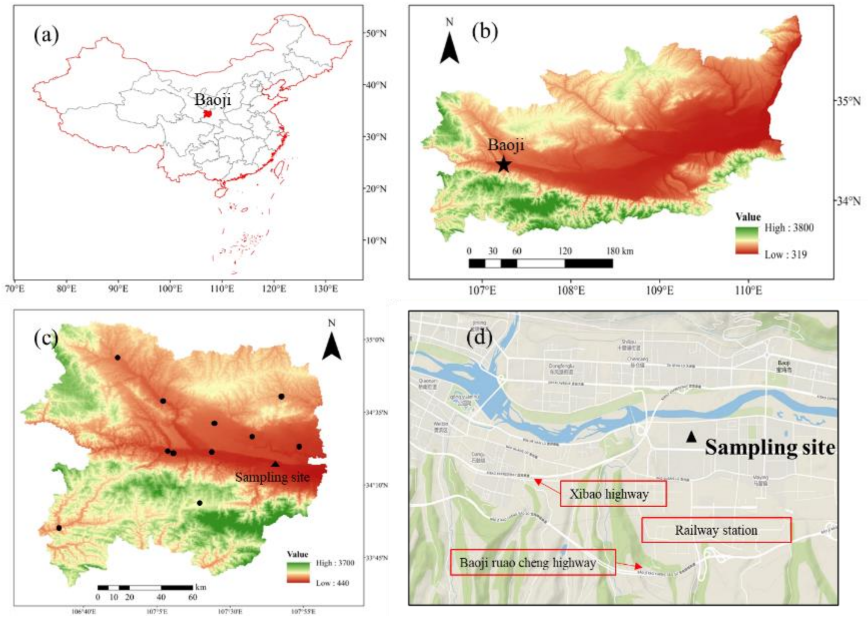

Figure R2. A map of the research site; (a) map of China—the red shape is the location of Baoji, (b) a map of the Guanzhong Plain, the black star represents the location of Baoji; (c) a map of Baoji City, the black dots and the black triangle represent 12 stations and the triangle is the location of sampling site, (d) a map of the sampling site.

L101: The time resolution of AE33 aethalometers can either be 1 min or 1 s. Do you mean you used 5-min averages of the 1-min data?

Response: The original data had 1-min time resolution. This has been corrected:

"eBC and the absorption coefficients (b_{abs}) at 370, 470, 520, 590, 660, 880, and 950 nm wavelength were measured using an AE33 aethalometer (Magee Scientific, Berkeley, CA, USA) equipped with a $PM_{2.5}$ cut-off inlet (SCC 1.829, BGI Inc. USA) that had a time resolution of 1 min."

L105-106: What type of quartz filter was used? The correction factor is dependent on the filter model.

Response: We double checked with the one of the coauthors about the tape and the C value used for this sampling. The tape is PN8060. We reset the C value to 1.39 instead of 2.14. Thanks so much for spotting this omission. We corrected this in the revised version.

"The quartz filter (PN8060) matrix scattering effect was corrected by using a factor of 1.39."

L133: What is the spatial resolution of the GDAS meteorological data?

Response: The spatial resolution of GDAS data is 1°×1°. We have added the resolution into the manuscript and provide a table with data and the main parameters used for the HYSPLIT model (Table R5).

"The data used for the Hybrid Single-Particle Lagrangian Integrated Trajectory (HYSPLIT) model was downloaded from Global Data Assimilation System and it had a resolution of 1°×1° (GDAS, https://www.ready.noaa.gov/gdas1.php). The data and main parameters used in trajectory model are listed in Table S2."

Table R5. Data and parameters used in HYSPLIT model

Items	Data/parameters
Model	HYSPLIT
Meteorological data	GDAS data, 1° × 1°, 23 vertical levels, 3 hourly
Backward period	24h
Footprint level	100 m above the ground
Receptor site location	34°21′16.8″N, 107°12′59.6″E

L162: The PMF methodology is described in section 2.3 for its classical use with mass concentrations of chemical species. Here it is used for optical source apportionment and therefore it should be explained how (concentrations are being replaced by what?) as well as the uncertainty calculation in that case.

Response: The use of the input data follows equation (R1)

$$X_{ij} = \sum_{k=1}^{p} g_{ik} f_{kj} + e_{ij} \tag{R1}$$

where X_{ij} denotes the input data matrix; p is the number of sources selected in the model; g_{ik} denotes the contribution of the k^{th} factor to the i^{th} input data; f_{kj} represents the k^{th} factor's profile of the j^{th} species; and e_{ij} represents the residual. Both g_{ik} and f_{kj} are non-negative.

As shown in the equation R1, the balance (mass balance for chemical data, total absorption balance for absorption data) isn't be violated by using a mixed input matrix X because each X_{ij} is independent from the others. PMF analysis is not degraded a priori by using joint matrices containing different dimensions/units (Forello et al., 2019 and reference therein). Putting data with different units in X means that matrix G (g_{ik}) is unitless and the corresponding column data in F (f_k) will have the same unit as the total values you into X (Paatero, 2018).

In addition, we were not interested in the total particulate mass which would satisfy the condition that the mass is equal to the sum of the mass of each chemical species. Instead, we focused only on the relationship between EC and light absorption coefficients to retrieve AAE values. We used chemical species only as tracers for different emission sources to help identify the factors. Thus, we simply use a joint matrix X[Y Z] where Y represents the part of the matrix for chemical species, Z represents the part of the matrix for light absorption coefficients.

The uncertainty of the input data was calculated by the following equation recommended in EPA PMF5.0 user guideline:

$$\text{Unc} = \sqrt{(\text{Error Fraction} \times \text{concentration})^2 + (0.5 \times \text{MDL})^2} \qquad \text{(R2)}$$

$$\text{Unc} = \frac{5}{6} \times \text{MDL} \qquad \text{(R3)}$$

where MDL is the minimum detection limit of different input data. When the concentration of species was higher than MDL then equation R2 was used otherwise equation R3 was used.

The error fraction for the offline measured data was the analytical uncertainty which in this study was taken to be the difference between replicate analyses of the same sample. The MDL was used based on the MDL of each chemical species as measured by the analytical instrumentation. For light absorption coefficients, the error fraction used was the measurement uncertainty of AE33. The uncertainty was estimated about 10% including changes in filter scattering caused due to aerosol loading, underestimation of source signals with increased filter loading, sample flow rate, filter spot area, and detector response (Rajesh and Ramachandran, 2019). Thus, we used 10% for light absorption coefficients for all wavelengths. The MDL of b_{abs} we used the value of 0.039M m^{-1} which is converted from the reported BC MDL of AE33 (0.005μg m^{-3}) in Rajesh and Ramachandran (2018).

To make the calculation clear, we have revised section 2.3, which can be seen in the response above.

Reference:

Forello, A. C., Bernardoni, V., Calzolai, G., Lucarelli, F., Massabo, D., Nava, S., Pileci, R. E., Prati, P., Valentini, S., Valli, G., and Vecchi, R.: Exploiting multi-wavelength aerosol absorption coefficients in a multi-time resolution source apportionment study to retrieve source-dependent absorption parameters, Atmos. Chem. Phys., 19, 11235-11252, 10.5194/acp-19-11235-2019, 2019.

Paatero, P.: Interactive comment on "Receptor modelling of both particle composition and size distribution from a background site in London, UK – the twostep approach" by David C. S. Beddows and Roy M. Harrison, https://doi.org/10.5194/acp-2018-784-RC2, 2018.

Rajesh, T., and Ramachanran, S., Black carbon aerosol mass concentration, absorption and single scattering albedo from single and dual spot aethalometers: Radiative implications, Journal of Aerosol Science 119, 77–90, https://doi.org/10.1016/j.jaerosci.2018.02.001, 2018.

L184: Is equation 13 correct? Both L175 and L188-189 describe R as the ratio between L and S but this does not correspond to the expression.

Response: We apologize for the inaccurate expression. The "R" on line 175 is the R defined in equation 13. We have corrected the description of the R in line 175. Now it consistent with the equation 13:

"Three variables were quantified, namely the actual wind run distance (S) which is the scalar displacement of the wind in 24 h (i.e. the accumulated distance of the wind), the resultant transport distance (L) which is the vector displacement of the wind in 24 h (i.e. the straight line from the starting point to the end point), and the recirculation factor (R) is based on the ratio of L and S which indicates the frequency of the wind veering in 24 h."

L206: What is the time resolution of the three sets of data? Are you using hourly averages?

Response: Yes, we used hourly averaged data. To make this clear, we added the time resolution into the sentence:

"Hourly averages of three sets of data (R_{std}, L_{bj}, and S_{bj}) were input into SOM. Determining the size of the output map is crucial for SOM (Chang et al 2020 and Liu et al., 2021)."

L303-318: I would suggest to include the four different average values (L(bj), S(bj), R(bj) and R(std)) for the four motion categories in Table 1 as well, and not repeat all the values in this paragraph but rather focus on the comparison and the interpretation.

Response: Thanks for the suggestion, we have revised this part in 3.2 section to make this section more concise and readable. The revised version is:

"The K-means results showed that the four-category solution was appropriate for interpretation as explained above (see also Figure S10). Thus a 2×2 map size was used for the self organizing map (SOM). The four featured atmospheric motion categories given by SOM (Figure S11) were identified as follows (feature values are in Table 1):

1. Local-scale dominance (LD): This category featured high R_{bj} and R_{std}. As described in section 2.5, high R_{std} indicates greater divergence of R at the 12 stations due to the strong influence of local-scale turbulence and convection. L_{bj} and S_{bj} were shorter than 130 km implying stagnation (Allwine and Whiteman, 1994).
2. Local-scale strong and regional-scale weak (LSRW): For this group, L_{bj} and S_{bj} were longer than those for LD, and R_{std} was slightly lower than that in LD.
3. Local-scale weak and regional-scale strong (LWRS): As the values suggest, both R_{bj} and R_{std} were lower than those in LD and LSRW, especially R_{bj}. This suggests the winds veered less frequently and the differences of R found in 12 stations were smaller than in the two situations above. This situation shows that the influence of the regional-scale motion was greater than that for the previous two categories.
4. Regional-scale dominance (RD): In this category, wind direction at the study site was nearly uniform (extremely low R_{bj}) suggesting good ventilation (Allwine and Whiteman, 1994). The differences among R found at the 12 stations were even smaller than for the LWRS group, implying a strong increased influence of regional-scale motions. Indeed, the influence of regional-scale motions far outweighed the

local ones for this category, and therefore, this group was considered to be dominated by strong regional-scale motions.”

Table R6. The mass concentration of eBC from fossil fuel combustion (eBC$_{fossil}$) and eBC from biomass burning (eBC$_{biomass}$) associated with different clusters under four featured atmospheric motions

Motion category	Local scale dominance (LD) (40%)				Local scale strong and regional scale weak (LSRW) (17%)			
	L_{bj} = 70.9 km, S_{bj} = 107.8 km, R_{bj} = 0.35, R_{std} = 0.25				L_{bj} = 106.9 km, S_{bj} = 164.8 km, R_{bj}=0.33, R_{std} = 0.23			
	Cluster 1	Cluster 2	Cluster 3	Total average	Cluster 1	Cluster 2	Cluster 3	Total average
Trajectory percentage (%)	45	52	3	100	56	33	11	100
eBC$_{fossil}$ (μg m^{-3})	2.82[a] ± 1.59[b]	3.2 ± 1.73	3.64 ± 0.67	3.08 ± 2.07	2.42 ± 1.00	3.43 ± 1.17	2.89 ± 1.00	2.79 ± 1.73
eBC$_{biomass}$(μg m-^{3})	1.34 ± 1.07	1.72 ± 1.29	0.67 ± 0.87	1.52 ± 1.19	1.0 ± 0.85	1.17 ± 0.84	1.00 ± 0.64	1.06 ± 0.83

L_{bj}—resultant transport distance, S_{bj}—actual wind run distance at 100 m, R_{bj} —recirculation factor at 100 m, R_{std}—standard deviation for recirculation factor. a and b: Mean ± Standard deviation.

Table R6 (continued)

Motion category	Local scale weak and regional scale strong (LWRS) (14%)				Regional scale dominance (RD) (29%)			
	L_{bj} =159 km, S_{bj} = 183.4 km, R_{bj}=0.13, R_{std} = 0.20				L_{bj} =235.6 km, S_{bj} = 246.4 km, R_{bj}= 0.05, R_{std} = 0.18			
	Cluster 1	Cluster 2	Cluster 3	Total average	Cluster 1	Cluster 2	Cluster 3	Total average
Trajectory percentage (%)	42	22	36	100	41	20	39	100
eBC$_{fossil}$ (μg m^{-3})	1.32[a] ± 0.67[b]	2.02 ± 0.73	3.16 ± 1.19	2.15 ± 1.62	1.00 ± 0.64	1.02 ± 0.88	2.75 ± 1.26	1.69 ± 1.36
eBC$_{biomass}$(μg m-^{3})	0.67 ± 0.49	0.73 ± 0.47	1.19 ± 0.60	0.86 ± 0.58	0.64 ± 0.63	0.87 ± 0.69	1.26 ± 0.68	0.93 ± 0.72

L_{bj}—resultant transport distance, S_{bj}—actual wind run distance at 100 m, R_{bj} —recirculation factor at 100 m, R_{std}—standard deviation for recirculation factor. a and b: Mean ± Standard deviation.

L341-344: Are emission inventories available to support the assumption that eBC from biomass burning is more regional then eBC from fossil fuel combustion? L388: A similar conclusion as above is reached here using the back trajectory cluster analysis.

Response: We thank reviewer for this suggestion. We considered using emission inventories to investigate this, however to our knowledge, the available emission inventory is Multi-resolution Emission Inventory for China (MEIC) which contains 6 emission categories (stationary combustion, industrial processes, mobile source, agriculture source, and residential source). We currently do not have access to a detailed source section (e.g. the individual biomass burning source and fossil fuel combustion source) inventory, which is what would be most helpful. Thus, it is not possible to show the source of biomass burning and fossil fuel combustion in an inventory map.

Non-parametric wind regression plots on these two variables could also be informative to assess the local vs. regional influence. See for instance: Gu et al. https://www.sciencedirect.com/science/article/pii/S0160412019342369 or Pandey et al.: https://link.springer.com/article/10.1007/s10661-022-09879-9

Response: As suggested, we have drawn the non-parametric wind regression plots for eBC$_{\mathrm{biomass}}$ and eBC$_{\mathrm{fossil}}$. As shown in Figure R3, during the night, the eBC$_{\mathrm{biomass}}$ was higher when the wind speed was faster, but in contrast, eBC$_{\mathrm{fossil}}$ was higher when the wind was slower. This indicates that during night, the emission sources of eBC$_{\mathrm{biomass}}$ were located further than the sources of eBC$_{\mathrm{fossil}}$, which explains why the mass concentrations of eBC$_{\mathrm{biomass}}$ did not decrease when the influence of regional-scale atmospheric motions was stronger. We have added this figure to the supplementary materials.

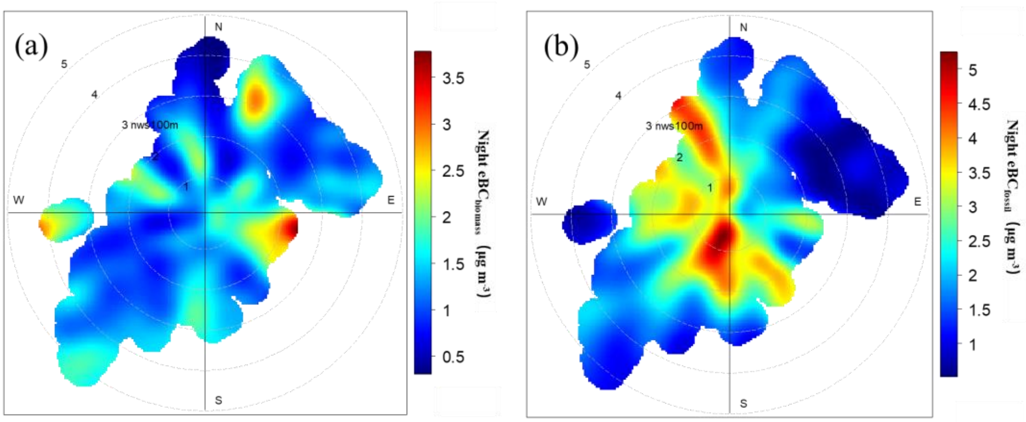

Figure R3 Non-parametric wind regression plots for eBC$_{\mathrm{biomass}}$ (a) and eBC$_{\mathrm{fossil}}$ (b) at night. The radial and tangential axes represent the wind direction (°) and speed (m s^{-1}), respectively, and nws100 m represents the night wind speed 100 m above ground level.

Supplementary Information

Figure S5: eBC(diesel) is actually EC from the PMF factor attributed to diesel vehicular emissions if I understand correctly what is written in the main text (L248). I do not think it should be considered equivalent to an eBC(diesel) which is confusing with eBC(fossil).

Response: We thank the reviewer pointing this out. It should be EC not eBC. We apologize for this mistake. The correction has been made:

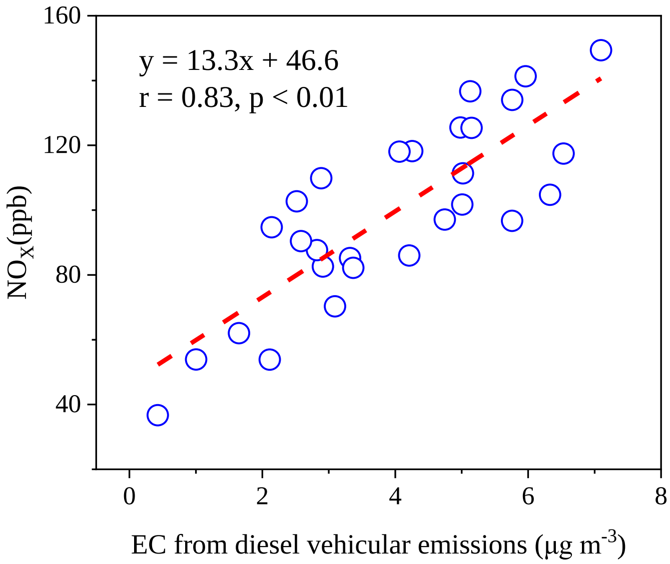

FigureR4. Linear regression of the daily averaged NO_x versus the daily averaged elemental carbon (EC) emitted from diesel vehicular emissions. The red line is the linear fit.

Figure S8: The caption is not very informative. Do L24h and S24h correspond to L(bj) and R(bj) mentioned in the main text. Being not familiar with the SOM approach, it is hard to figure out what this represents and how to interpret it.

Response: We agree with reviewer. The L24h and S24h correspond to L_{bj} and S_{bj}. We have updated the names to make them consistent with the main text. The averaged L_{bj}, S_{bj} and R_{std} of the four categories were calculated based on this SOM cluster.

To make this figure easier to interpret, we have added some explanation under the figure as follows:

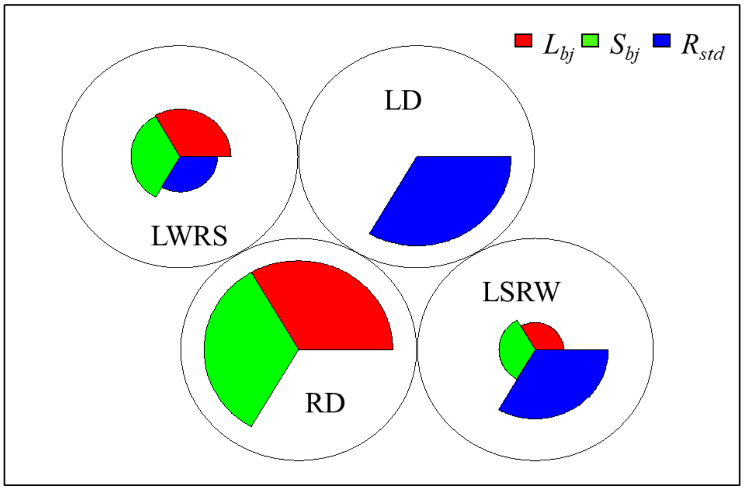

FigureR5. The result of the self-organizing map, sectorial shape represents each variable (L_{bj}, S_{bj} and R_{std}), the bigger the size the larger this variable. The four circles with the sectorial color together indicate the features of the four motion categories. The bottom left circle means high L_{bj} and S_{bj} but low R_{std}, which

indicates the feature of regional scale dominance (RD) category. The bottom right represents the high R_{std} but relatively low L_{bj} and S_{bj} indicating local-scale strong and regional scale weak (LSRW). The upper left represents local scale weak and regional-scale strong (LWRS) and the upper right represent local scale dominance (LD).

Technical corrections (list non-exhaustive):

L32: "It highlights". Do you mean "This study emphasizes the fact that"? (or something along that line)

Response: Yes, we do. We changed the wording:

"The finding that the DRE efficiency of BC increased during the regional transport suggested significant consequences in regions downwind of pollution sources and emphasizes the importance of regionally transported BC for potential climatic effects."

L54: "Local concentrations of BC are"

Response: Correction has made.

"The concentrations of BC are controlled by local emissions and regional transport, but meteorological conditions also are important because they affect both transport and removal."

L55: "predictable at to some degree". Delete "at".

Response: Correction has made.

"Normally, local emission in urban areas are predictable to some degree because those emission sources are mainly anthropogenic and the concentrations of pollutants follow the diurnal patterns driven by anthropogenic activities."

L56: "the concentration of pollutants follows"

Response: Correction has made, see the response above.

L57: "multiple" instead of "multiply"

Response: We corrected this.

"By contrast, meteorological conditions and regional transport are governed by multiple scales of motion which result in distinct meteorological impacts on ambient pollutant levels (Levy et al., 2010, Dutton, 1976)."

L76: "it can play"

Response: We have rewritten the sentence, now it reads:

"Surface albedo and surface roughness are affected by the complex topography of river-valley regions, and those physical factors can affect circulation and cause changes in pollutant mass concentrations (Wei et al., 2020)."

L78: "to converge"

Response: We have corrected this. Then sentence now reads:

"Instead of being dispersed, they can be carried by the airflows over the mountains to converge at the bottom of the valley and increase the pollutants along the river (Zhao et al., 2015)."

L80: "fascinated". Maybe too strong a word? May I suggest "keen on studying" instead. "eBCs" not defined.

Response: We changed the expression:

"Thus, we focused our study on the impacts of different scales of motion on source-specific equivalent BCs (eBCs), and we evaluated radiative effects of eBCs over a river-valley city."

L92-93: "located at the furthest west"

Response: We corrected this mistake:

"Baoji is a typical river-valley city, located at the furthest west of the Guanzhong Plain, at an altitude from 450 to 800 m a.s.l. (Figure S1), Baoji has a complex topography and often suffering from severe pollution in winter."

L93: replace "suffers" by "suffering from"

Response: Correction has made, see in the above response.

L107: "Aurora"

Response: We corrected the spelling.

L151: "deconvolved" rather than "separated"

Response: We have replace "separated" with "deconvolved".

"The quantities of eBC generated from biomass burning versus fossil fuel combustion were deconvolved by an aethalometer model which uses Beer-Lambert's Law to write the absorption coefficients equations, wavelengths and absorption Ångström exponents (AAEs) for the two different BC emission sources (Sandradewi et. al., 2008)."

L171: "different scales"

Response: Correction has been made:

"2.5 Indicators for the different scales of motion"

L230: "minus"

Response: We corrected the spelling:

"where DRE_{eBC} is the DRE of source-specific eBC, $F\downarrow$ and $F\uparrow$ are the downward and upward flux, $DRE_{eBC,ATM}$ is the DRE of the source-specific eBC for the atmospheric column, that is, the DRE at the top of the atmosphere ($DRE_{eBC,TOA}$) minus that at the surface ($DRE_{eBC,SUF}$)."

L235: "was run"

Response: We corrected this:

“For every solution, PMF was run 20 times. The Q_{true}/Q_{exp} ratios from the 2- to 7-factor solutions were examined, and the values of a 4-factor solution were found most stable compared with others because the Q_{true}/Q_{exp} values did not drop appreciably after the addition of one more factor (Figure S5).”

L236: “2-factor solution (…) 7-factor solution (…) 4-factor solution” + L237, L239

Response: We corrected this.

L279: “were calculated”

Response: Correction has been made:

“Thus, the AAE_{fossil} (1.26) and MAC $(880)_{fossil}$ (7.1 m^2 g^{-1}) were calculated was the mass-weighted averages (relative to the total EC) of AAE_{coal} (MAC $(880)_{coal}$) and AAE_{diesel} (MAC $(880)_{diesel}$) (Table S4)”

L282-283: “Their diurnal variations showed varied”. Please consider revising.

Response: We have rewritten this sentence. Now it reads:

“The results showed that eBC_{fossil} and $eBC_{biomass}$ were only weakly correlated (r = 0.3, Figure S9), indicating a reasonably good separation, and furthermore, their diel variations showed different patterns (Figure 2).”

L282, 284: “diel” instead of “diurnal”

Response: We have changed the words. The sentences now read:

“The diel variations of eBC_{fossil} (Figure 2a) showed a bimodal pattern with two peaks at 9 a.m. and 7 p.m local time. which are typical peak commuting hours, indicating that there were strong influence s from traffic emissions.” And the response above.

L293: “New para here” should be deleted.

Response: We deleted it:

“Later the PBLH decreased rapidly, resulting in conditions unfavorable for dispersion, and then eBC_{fossil} rose quickly to the second peak at 7 p.m. After passing the evening peak in traffic, the eBC_{fossil} decreased dramatically.”

L331: rather “clean” instead of “clear”.

Response: This correction has been made:

“When the regional scale of motion became stronger (i.e., LWRS and RD), the average mass concentration of eBC_{fossil} (2.15 ± 1.62 μg m^{-3} and 1.69 ± 1.36 μg m^{-3}) and $eBC_{biomass}$ (0.86 ± 1.58 μg m^{-3} and 0.93 ± 0.72 μg m^{-3}) were lower, presumably because strong winds cause the pollutants to mix with cleaner air.”

L333: “were carried”

Response: We corrected this:

"Interestingly, 19% of the total 75th to 100th percentile $eBC_{biomass}$ was found under RD, and 55% of that was when ventilation good ($S_{bj} \geq 250$km, $R_{bj} \leq 0.2$, Figure 3, shaded grey). These findings imply that the high mass concentrations of $eBC_{biomass}$ were carried by regional-scale airflow to the site."

L360-362: Consider revising this sentence: "emissions at in" (delete "at"); "(~75%) of the total population of Baoji)" can be replaced by "(that is to say 75%)"; "distributed located", pick only one.

Response: We have rewritten the sentence, now it reads:

"This could be attributed to more intensive emissions in the eastern parts of Baoji because 75% of the total population of Baoji is located in this area (http://tjj.baoji.gov.cn/art/2020/10/15/art_9233_1216737.html, accessed on 25 September 2021, in Chinese)."

L432: "outweighed the regional-scale motion"

Response: Correction has been made:

"This illustrates that the BC pollution was more severe under the influences of local-scale motion outweighed regional-scale motions."

L436: "found to be raised"

Response: We have corrected this sentence, now it reads:

"eBC_{fossil} most likely accumulated under the influence of strong local-scale motions, but $eBC_{biomass}$ also was found to be increased with the enhanced regional scale of motions when the air masses from the southwest; this indicates that there were impacts from regional transport."

L717: Figure 1 | x-axis title: "Pabs" instead of "babs"

Response: We thank review for pointing this out. We corrected this:

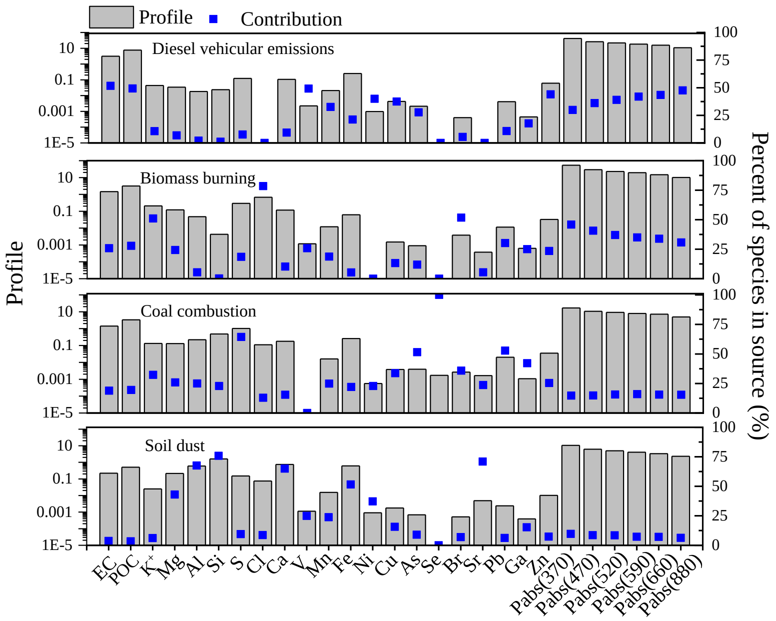

Figure R6. Four factors identified by source apportionment. Concentration (μg m^{-3}) of the chemical species and primary absorption coefficients (p_{abs}) (λ) at six wavelengths (λ = 370, 470, 520, 590, 660, or 880nm) (M m^{-1}) for each source are shown in grey. The blue square represents the contribution of each chemical species to the four different factors.

L721: "diurnal" should be replaced by "diel" (24-hour period). At the least, standard deviations could be added for each hourly-averaged point; otherwise each point could be replaced by a box and whiskers that better show the dispersion of the raw data.

Response: The standard deviations have been added for the each point of Figure 2. Now it looks like this:

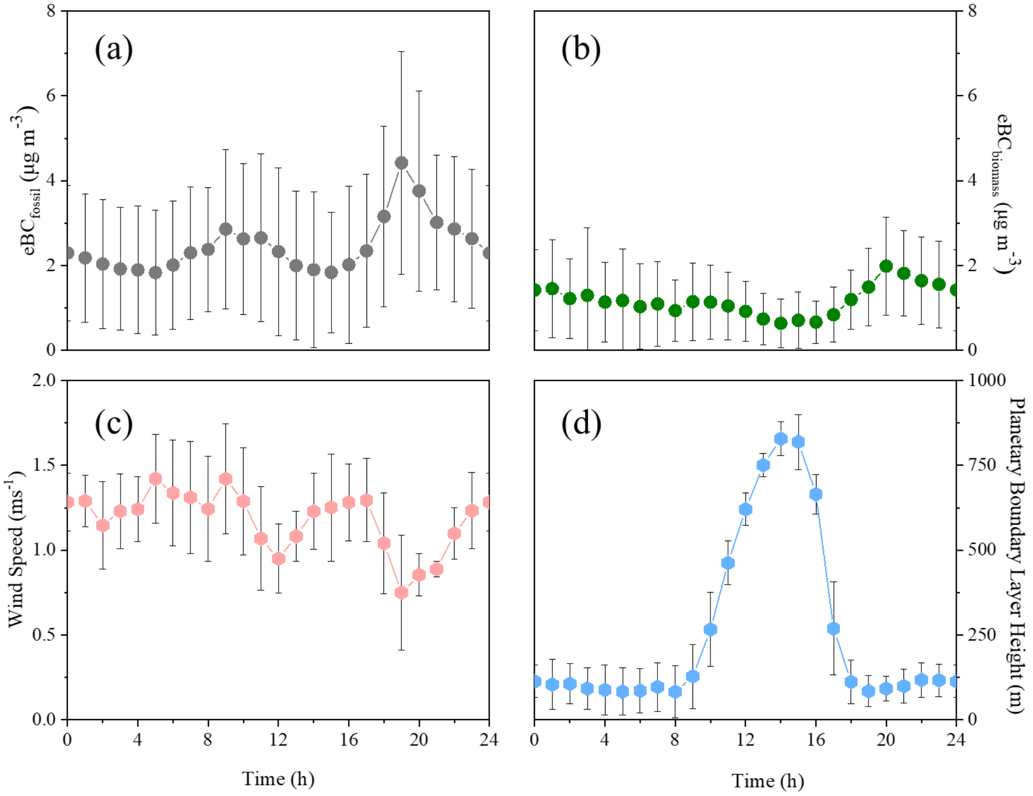

Figure R7. (a) Diel variations of the eBC from fossil fuel combustion (eBC$_{fossil}$) and (b) the eBC from biomass burning (eBC$_{biomass}$), (c) wind speed (m s^{-1}) and (d) planetary boundary layer height (m). The black bars of each hourly-averaged point show the standard deviation.

L724: Figure 3 caption should explain what the different marker colors and the shaded areas represent.

Response: We have revised the figure caption as follows:

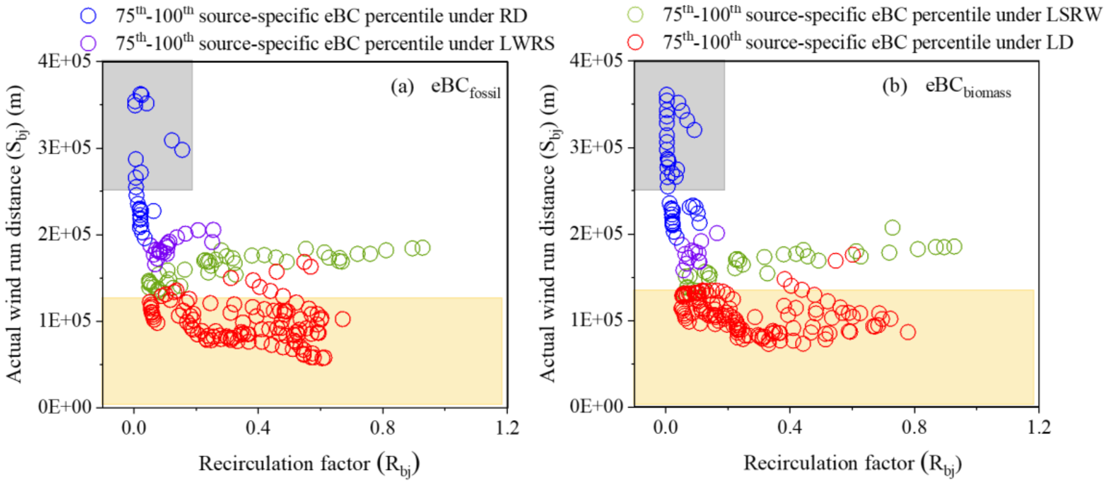

Figure R8. (a) The 75th – 100th percentile mass concentrations of the eBC from fossil fuel combustion (eBC_{fossil}) and (b) the eBC from biomass burning ($eBC_{biomass}$) under local scale dominance (LD, red circle), local scale strong and regional scale weak (LSRW, green circle), local scale weak regional scale strong (LWRS, purple circle) and regional scale dominance (RD, blue circle). S_{bj} is actual wind run distance at 100m height, R_{bj} is the recirculation factor, the grey area indicates good ventilation ($S_{bj} \geq 250km$, $R_{bj} \leq 0.2$), the yellow area indicates air stagnation ($S_{bj} \leq 130km$).

L731: Figure 5a | The 4th box and whisker plot (blue) should be labelled "fossil" and not "biomass" on the x-axis.

Response: We have re-drawn this figure and corrected the label as follows:

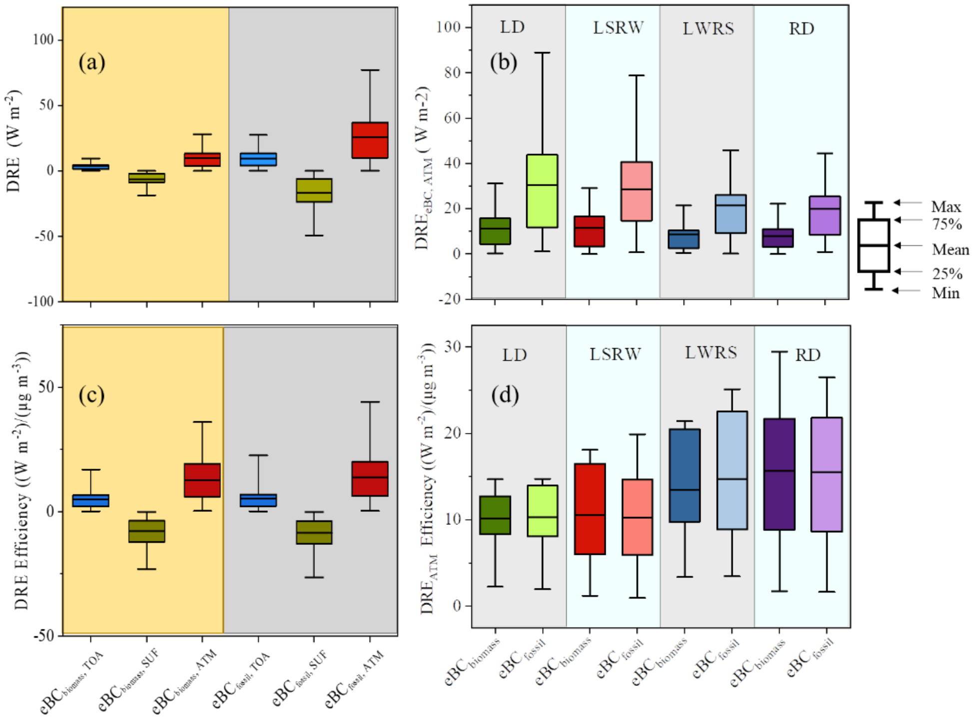

Figure R9. Direct radiative effect (DRE) of the eBC from fossil fuel combustion (eBC_{fossil}) shaded in grey and the eBC from biomass burning ($eBC_{biomass}$) shaded in yellow (a) in the top atmosphere (TOA), surface (SUF), and the atmosphere atmospheric column (ATM) and (b) the $DRE_{eBC,ATM}$ of two types of eBC under local scale dominance (LD) shaded in light grey labeled as LD, local scale strong and regional scale weak (LSRW) shaded in light blue labeled as LSRW, local scale weak regional scale strong (LWRS) shaded in light grey labeled with LWRS and regional scale dominance (RD) shaded in light blue labelled as RD (c) DRE efficiencies of $eBC_{biomass}$ (shaded in yellow) and eBC_{fossil} (shaded by grey) in TOA, SUF and ATM (d) DRE efficiencies of $eBC_{biomass}$ and eBC_{fossil} at ATM under LD (shaded in light grey labeled as LD), LSRW (shaded in light blue labeled as LSRW), LWRS (shaded in light grey labeled as LWRS) and RD (shaded in light blue labeled with RD).

Supplementary Information

Table S2 would look better if numbers were aligned with column titles.

Response: Thanks for the suggestion, we have aligned the number with column titles.

Table R7. Mass absorption cross sections (MAC) and absorption Ångström exponents (AAE) derived from the positive matrix factorization model

	Diesel vehicular missions	Coal combustion	Biomass burning	Fossil fuel combustion
MAC (m^2 g^{-1})	6.7	7.5	9.5	7.1
AAE	1.07	1.74	2.13	1.26

Figure S1: Add a scale on both maps. Topography should be indicated on the closer range map.

Response: We have updated the map of the region in the supplementary materials. It can be seen in the response above.

Figure S2 caption: "the modelled b_{abs}(500 nm) (respectively, SSA) and the observed b_{abs}(520 nm) (resp. SSA)". Right now, it reads like a ratio of the two parameters.

Response: We thank reviewer's suggestion and have rewritten the caption as follows:

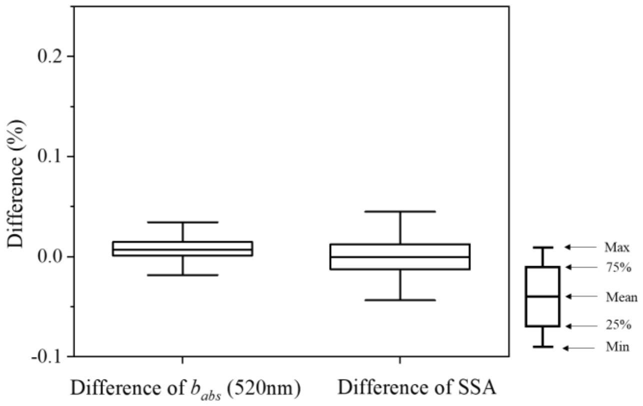

Figure R10. The difference between the modeled b_{abs}(500nm) (respectively, SSA) and the observed b_{abs}(520nm) (respectively, SSA).

Figures S4, S5 and S6: What does each point represent? (daily average, other?)

Response: The $b_{abs}(\lambda)$ in Figure S4 are daily averaged data. NO_x and EC in Figure S5 are daily averaged data. The $eBC_{biomass}$ and eBC_{fossil} are hourly averaged data. We have added this into the caption for each figure as follows:

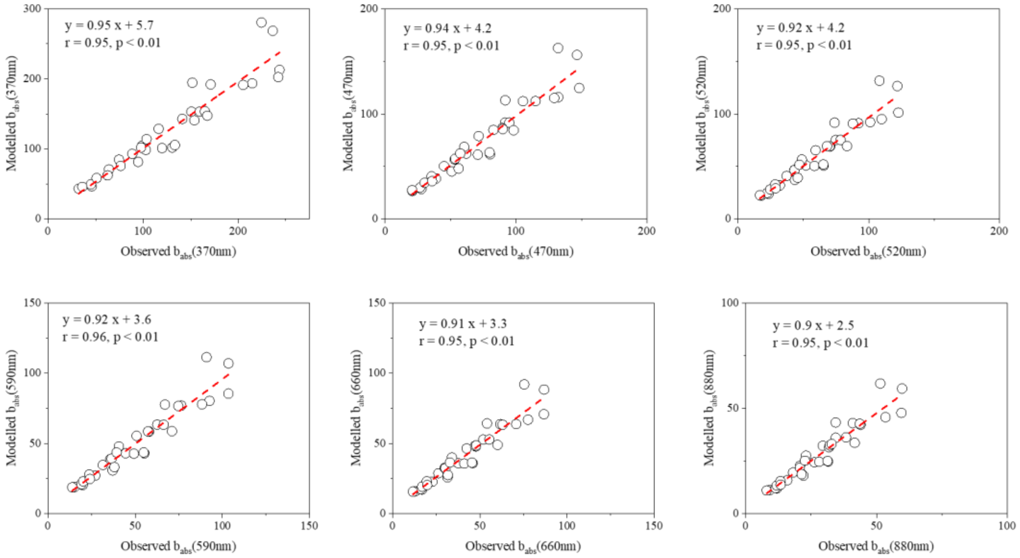

Figure R11. Relationship between the observed daily averaged $b_{abs}(\lambda)$ and positive matrix factorization modeled b_{abs} (λ). λ includes 370, 470, 520, 590, 660 and 880nm. The red line is a linear fit.

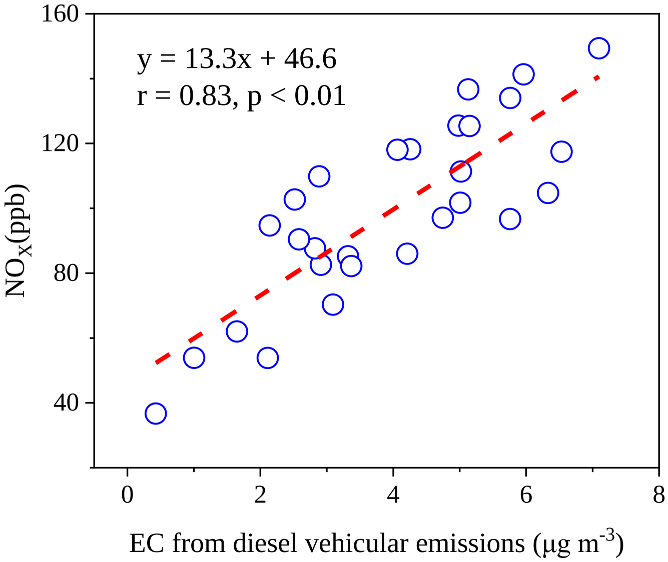

Figure R12. Linear regression of the daily averaged NO_x versus the daily averaged elemental carbon (EC) emitted from diesel vehicular emissions. The red line is the linear fit.

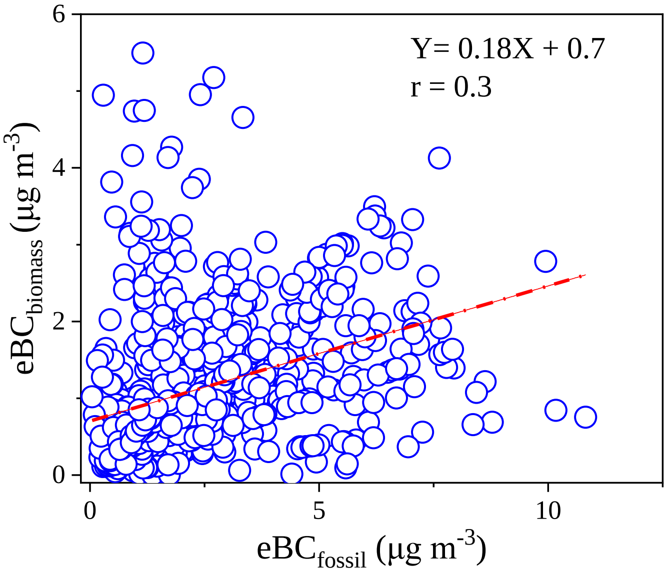

Figure R13. Relationship between hourly averaged eBC from biomass burning ($eBC_{biomass}$) and the eBC emitted from fossil fuel combustion (eBC_{fossil}). The red line is a linear fit.

Figure S9: "diurnal" should be replaced by "diel" (24-hour period). At the least, standard deviations could be added for each hourly-averaged point; otherwise each point could be replaced by a box and whisker that better shows the dispersion of the raw data.

Response: We have revised this figure with standard deviations:

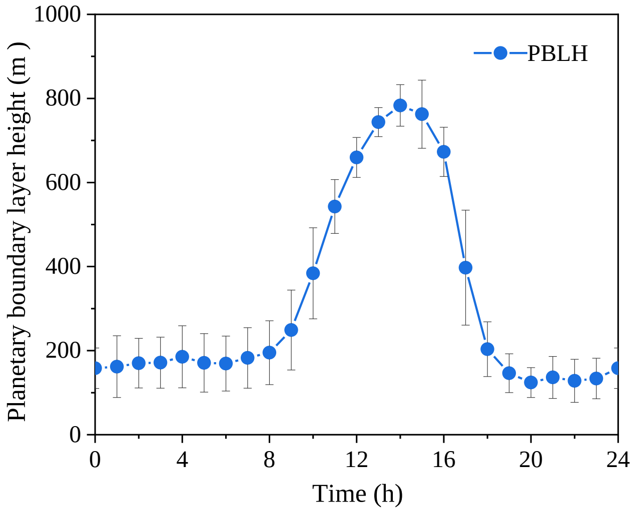

Figure R14. Diel variations of planetary boundary layer height (PBLH, m) under the dominance of regional scale of motion (RD), the blue dots represent the hourly-averaged PBLH and the black lines represent the standard deviations for each point.